DEVELOPMENT OF CLUSTER SECONDARY ION MASS SPECTROMETRY FOR SURFACE CHARACTERIZATION AT THE NANOSCALE

A Dissertation

by

FAN YANG

Submitted to the Office of Graduate and Professional Studies of
Texas A&M University
in partial fulfillment of the requirements for the degree of

DOCTOR OF PHILOSOPHY

Chair of Committee,	Emile Schweikert
Committee Members,	Lei Fang
	Timothy Phillips
	Karen Wooley
Head of Department,	Francois Gabbai

May 2016

Major Subject: Chemistry

ABSTRACT

Cluster secondary ion mass spectrometry (SIMS) operated in the event-by-event bombardment-detection mode has been applied to 1) nanodomain analysis of macromolecular brush architecture; 2) characterization of raw and modified plant surfaces; 3) adsorption identification and coverage kinetics of self-assembled monolayer on Au.

When an individual cluster projectile, in the present case Au_{400}^{4+} or C_{60}^{2+}, bombards a surface, it generates secondary ions (SIs) from a spot 10-15 nm in diameter and up to10 nm in depth, i.e. from molecules co-localized within a nanodomain (~10^3 nm^3). Their identification enables, in principle, to analyze surface composition at the nanoscale. Repeating the shot-by-shot bombardment-detection allows probing an ensemble of nanodomains stochastically. One can then extract from the records of individual impacts, subsets of data that correspond to like-domains with sufficient statistics for molecular characterization.

The first type of material investigated was diblock brush terpolymers (DBTs) films. The DBT architecture consists of a rigid backbone linking to side brush chains. A vertically aligned film of DBTs improves the resolution of electron-beam lithography etching to sub-30 nm. Thus, their evaluation and characterization must be performed at the nanoscale. The analysis of mass spectra that are obtained from each nanodomain allows determining the surface coverage by DBTs. The ratio of the surface coverage for the two groups in the DBT, the surface energy reducing moiety and the lithographic

functional moiety is a test for vertical alignment. The specimens evaluated showed that the DBT nanodomains are aligned vertically in a homogeneous arrangement.

Au_{400}^{4+} cluster SIMS and coincidence counting was also applied to determine the chemical composition and surface homogeneity of plant materials. Co-emitted and correlated SIs show that chemical components (e.g. long chain hydrocarbons, fatty acids, and their derivatives) are not always evenly distributed on the plant surface. The effect of etching with an oxygen plasma on the tomato surface was investigated with the innovative SIMS. The mass spectra results show that the epicuticular wax layer can be removed with a time-dependent oxygen plasma treatment. Further, we could measure the degree of surface coating of polymer (polyethylene glycol or polyvinylpyrrolidone) films physisorbed on the tomato surfaces to keep contents hydrated and prevent the bacterial adhesion. Our observations verified that the polyethylene glycol film could be effectively applied or removed as desired.

C_{60}^{2+} SIMS was used to analyze to study the adsorption of self-assembled monolayers (SAMs). Alkanethiol on Au was used as a model SAM. At the level of a single projectile impact, C_{60} SIMS could characterize the surface homogeneity and coverage of ultra-thin SAMs, a valuable feature for kinetic studies of SAM formation at the nanoscale.

DEDICATION

To

my beloved

mother, father, parent-in-laws,

most of all,

to Dongyuan, Russell, and Riley

ACKNOWLEDGEMENTS

I would like to take this opportunity to express my gratitude to the Schweikert research group for their help over years. Also, I would like to thank my committee members, Dr. Fang, Dr. Phillips, and Dr. Wooley for their advice. In particular, the sincerest thank my advisor, Dr. Schweikert, whose enthusiasm for science always inspires me to move forward. His advice, guidance, patience, encouragement, and extensive knowledge are decisive to finish this work. He is my role model and the best advisor in life. Special thanks also go to Dr. Verkhoturov, Dr. Eller, and Dr. Sun, whose enthusiastic and energetic attitude toward research. I appreciate their advice, passion, and emotional insightfulness to the nature of science.

I would like to appreciate my collaborators from Wooley's and Akbulut's research group at Texas A&M University and Dow Electronics. They are Dr. Cho, Dr. Trefonas, Dr. Thackeray, Dr. Zhang, and Jun, for their expertise in preparing polymer and biological samples and constructive contributions to this study. I am graceful to have a great experience to collaborate with them.

Also, I sincerely thank all staffs in the Center for Chemical Characterization and Analysis for their help and support. They are Dr. James, Mr. Micheal Raulerson, Dr. Tomlin, and Ms. Melton.

I would like to appreciate my colleagues and those I have met in College Station, especially my group members. They are Li-Jung, Francisco, Daniel, Chao-Kai, Aaron,

and Sheng, who are always helpful in many ways. They are the best co-workers in the world.

I would like to thank the grants for supporting this research: the National Science Foundation grant (CHE-1308312 & DMR-1105304), the Dow Chemical Company and the Robert A. Welch Foundation (A-0001).

Finally, the deepest gratitude to my beloved family, especially my wife Dongyuan, and my adorable son Russell for providing unconditional love, support, and encouragement to help me through the intertwined paths of graduate study.

NOMENCLATURE

16M	16-Mercaptohexadecanoic acid
2M2P	2-Methyl-2-propanethiol
6M1H	6-Mercapto-1-hexanol
C8	Octanethiol
C14	Tetradecanethiol
C18	Octadecanethiol
DBT	Diblock brush terpolymers
HBP	Homo-brushed polymers
IPNO	Institute for Nuclear Physics at Orsay
LMIS	Liquid metal ion source
MCP	Microchannel plate
PCB	Printed circuit board
PEG	Polyethylene glycol
PI	Primary ion
PVP	Polyvinylpyrrolidone
SAMPI	Surface analysis and mapping of projectile impacts
SEM	Scanning electron microscopy
SI	Secondary ion
SIMS	Secondary ion mass spectrometry
TDC	Time to digital converter

ToF	Time-of-flight

TABLE OF CONTENTS

LIST OF FIGURES

FIGURE Page

LIST OF TABLES

CHAPTER I

INTRODUCTION

In contrast to high-resolution microscopy, which can visualize nanometer scale structures and objects, molecular characterization of complex surfaces below the micrometer dimension is difficult, often impossible. A compilation of some current physical and chemical analysis techniques is provided in Table 1.1. One of the reasons for the limited "chemical vision" is the minute amount of sample available for analysis. The molecular analyzes of structures, objects, and domains of tens to a few hundred nanometers are at the core of critical problems for the study of nano-electronics and nano-photonics. It is a key to elucidating the effects of nanoparticles on health and the role of colloids and aerosols in the environment. The nanoscale characterization of complex materials requires multiple measurements by different instruments. Mass spectrometry, with its intrinsically versatile information, should be one of the methods of choice. A summary of techniques suitable for the molecular analysis of surfaces is provided in Table 1.2. There are two critical differences between the techniques listed in Table 1.1 and those based on mass spectrometry summarized in Table 1.2. The latter provide unequivocal molecular identification in complex surfaces; however, this distinct feature involves some sample consumption, while the techniques in Table 1.1 are physically nondestructive.

Table 1.1 Current surface analytical techniques and their applications

Technique	Detection Resolution	Features	Applications
Auger Electron Spectroscopy	Depth: 2–20 nm Lateral: ≥10 nm	Surface elemental composition, depth profiling, diffusion, and segregation	Metal and semiconductor thin films [1, 2]
High-Resolution Electron Energy Loss Spectroscopy	Depth: 0.5–20nm Lateral: 1–10 μm	Vibrational modes, local geometry of adsorbates, phonon dispersion	Single crystal metals [3, 4]
Infrared Adsorption Spectroscopy	Depth: 1–10 nm Lateral: 10–100 μm	Vibrational and molecular structure, functional groups	Meals, polymers, and organics [5, 6]
Total Reflection X-ray Fluorescence Spectroscopy	Depth: 3–10 nm Lateral: >1 mm	Trace elemental composition in and on top of surface	Metallic surface on semiconductor wafers [7]
X-ray Photoelectron Spectroscopy	Depth: 0.5–10 nm Lateral: >10 μm	Elemental composition, chemical bonding, and oxidation state.	Metal and semiconductor thin films [8, 9]
Atomic Force Microscopy/Scanning Probe Microscopy	Depth: 1–2 monolayers Lateral:0.1–10 nm	Surface topology map, elasticity, friction, magnetic and electrostatic forces	Nanoscale materials [8, 10, 11]
Scanning Electron Microscopy	Depth: ~1 μm Lateral: 10–1μm	Topography, elemental composition, line scan, and point analysis	Nanoscale materials [11]
Scanning Tunneling Microscopy	Depth: 1–3 monolayers Lateral: 0.1–10 nm	Map of surface electron structure, surface topography and reconstruction	Conductive materials [12, 13]
Förster (Fluorescence)Resonance Energy Transfer	Depth: 2–15 nm Lateral: ~200 nm	Macromolecular chemical composition and structural spectroscopy and imaging	Macromolecules, biomaterials, living cells [14, 15]

Table 1.1 Continued

Technique	Detection Resolution	Features	Applications
Scanning Photoelectron Microscope	Depth: 2–10 nm Lateral: 50–100 nm	Real-time scanning electron structure, mapping and imaging	Au/Si pattern thin films [16, 17]
Synchrotron Radiation Scanning Tunneling Microscopy	Depth: 1–5 nm Lateral: ~10 nm	Chemical composition, electronic and magnetic spectroscopy and high-resolution imaging	Low index single crystal metals [18]
Scanning Transmission X-ray Microscopy	Depth: 2–10 nm Lateral:10–50 nm	Use X-ray light to scan samples to obtain electron images or mappings	Metal or semiconductor oxides catalysts [19]
Tip-enhanced Raman Spectroscopy	Depth: ~2 nm Lateral: 20–50 nm	Chemical composition, functional groups, adsorbate on specific sites	Organics on SiO_x patterns [20-23]

Table 1.2 Current surface analytical mass spectrometry techniques.

Name	Principle of Operation	Advantages and Disadvantages
Cluster Secondary Ion Mass Spectrometry	Uses clusters instead of atomic ions as projectiles to improve ion yields at the surface [24, 25].	Pros: relatively high resolution (spatial resolution: ~100nm); less chemical noise as background Cons: only under vacuum conditions.
Desorption Electrospray Ionization-Mass Spectrometry	Combines electrospray and desorption ionization methods: ionization takes place by directing an electrically charged mist to the sample surface. The electrospray mist is attracted towards the surface by a bias voltage, and then the ions travel through the air into the atmospheric pressure interface to the mass spectrometer [26].	Pros: can detect both small and large molecules (peptides and proteins); an ambient ionization technique Cons: hard to identify molecules strong bond to the substrate or low solubility molecules; significant background effects.

Table 1.2 Continued

Name	Principle of Operation	Advantages and Disadvantages
Static Secondary Ion Mass Spectrometry	The high-energy impact of the primary ion results in cascades of collisions between atoms, molecules and other particles in the solid, some of which return to the surface region is resulting in the sputtering of molecules, molecular fragments, and atoms [25].	Pros: can detect molecules with strong bonds to the substrate; MS with some structural information Cons: Vacuum operation; hard to analyze proteins and large peptides.
Fast Atom Bombardment-Mass Spectrometry	Accelerated inert atoms (after neutralization) with high energy bombard the sample with matrix [25, 27].	Pros: detect insulating surface; good spatial resolution (~1 μm). Cons: operation under vacuum condition; hard to detect large molecules
Laser Ablation (Assisted) Electrospray Ionization-Mass Spectrometry	Combines laser ablation from a mid-infrared laser with a secondary electrospray ionization process	Pros: operates at ambient conditions; Cons: Poor resolution and negative ion detection (compared with MALDI and SIMS)

Table 1.2 Continued

Name	Principle of Operation	Advantages and Disadvantages
Matrix-Assisted Laser Desorption/Ionization- Mass Spectrometry	Coating or mixing a sample with compounds, i.e. matrix, that facilitate the absorption of laser photons in a particular wavelength varied with molecular ions and fragment ions that reflect some degree the chemistry of the material being analyzed [24, 28]	Pros: good sensitivity; suitable for large molecular detection with high ion yield Cons: requires a matrix treatment to samples before using [29]

A characteristic common to all molecular techniques is the capability to analyze a surface area of a few to a few hundred microns. Our approach is cluster secondary ion mass spectrometry (SIMS) with the event-by-event bombardment mode.

Overview of SIMS

SIMS is used to analyze the chemical composition of solid surfaces by sputtering the specimen with a primary ion beam and then analyzing ejected secondary ions. The mass of these secondary ions is measured to determine the elemental, isotopic, or molecular composition of the surface [30-32]. Due to the significant variation in ionization probabilities among different materials, conventional SIMS is suitable for qualitative

analysis, but it requires references to achieve the quantitative analysis. SIMS is one of the most sensitive surface analysis techniques with detection limits (for elemental and isotopic analysis) from parts per million to parts per billion [32, 33].

SIMS requires a high vacuum with pressures below 10^{-6} torr. To ensure the sufficient free path length for secondary ions and electrons, i.e. to minimize collision with residual gas on their way to the detector. A high vacuum also minimizes surface contamination during measurement [30, 32].

Several types of ions, depending on their generators (ion guns or ion sources), are used as primary ions to bombard the sample surface. The first type of ion guns usually generates gaseous ions with duo-plasmatrons or by electron ionization, e.g., noble gas ions (He^+ and Xe^+) [32, 34, 35], or oxygen ions (O^+, O^{2+}, O^{2-}) [36-39]. They are easy to operate and generates roughly focused high current ion beams. The second type of the ion source is named surface ionization source. For example, a Cs^+ ion gun belongs to this type [40-43]: Cs atoms first vaporize through a porous tungsten plug and are then ionized during evaporation. Fine focus or high current ion beam can be achieved depending on the gun design. The third type is the liquid metal ion source, which operates with metals or metallic alloys. In this type, a liquid metal covers a tungsten tip and emits ions under an intense electric field [44]. A typical liquid metal ion source is a Ga source, as well as Au, In and Bi [45-48]. The feature of some types of liquid metal ion sources, e.g. Ga or Bi liquid metal ion sources, is that it could provide a tightly focused ion beam (<50 nm) with moderate intensity and is further able to generate short pulsed ion beams [44, 49, 50]. It is therefore commonly used in the static SIMS application.

Dynamic and static SIMS

Depending on the application field, SIMS usually has a dynamic or static mode. The first one involves multilayers or film analysis with a direct current ion beam and a magnetic sector or quadrupole mass spectrometer while the latter one is a process of the surface outermost layer analysis. The static mode often uses a pulsed ion beam and a time-of-flight mass spectrometer [31, 32].

Dynamic SIMS uses a continuous ion beam (as the primary ions) to detach top layers of materials from the surface with sputtering [32]. The fragment of the sputtered material is ionized as secondary ions, and they are extracted and analyzed with a mass spectrometer. Dynamic SIMS can detect fractions in the range of parts per billion, so it is suitable to determine the trace levels of impurities and dopants on the surface [51]. Nevertheless, dynamic SIMS is impossible to obtain molecular information because the surface structure and component at the molecular level are destroyed during the sputtering process [52-54].

Different from the dynamic mode, static SIMS has a small ion sputtering rate of the surface [32]. Its dose of primary ions is often less than 10^{12} ions per cm^2, which is defined as the "static limit". Only 1% or less of the surface area is influenced or damaged during the static analysis. Therefore, it is considered as a non-destructive technique [55]. The low energy density of primary ions perturbs only the topmost layers of the surface, which enables that the static SIMS is one of the most surface sensitive techniques [56-58]. The application of the static SIMS includes elemental composition and chemical structure of a solid, e.g., metal, semiconductor or polymer. However, the resolution of the static

SIMS, especially for an imaging application, is constricted by the low secondary ion yield [59]. This challenge is the limited quantity of free molecules emitted from a small probing area. Large cluster ions are recently developed as primary ions to increase the emission of secondary ions.

Polyatomic or cluster ions in SIMS

As discussed, the application of atomic ion beams has been limited by low secondary ion yields and beam induced damage effects, especially when it is used for characterizing organic and polymeric surfaces [60-63]. The analysis of organics or polymers in the static mode with a low-density dose to retain the surface undamaged to decrease sensitivity. One possible solution is to use polyatomic (e.g. SF_5^+ [64]) or cluster ion source (e.g. C_{60}^+ [65, 66]) as the primary beam. Compared to the atomic ion beam, the cluster beam is considerable increases in secondary ion yields, in particular for the molecular ions and reductions in beam-induced damage accumulation on the surface [67, 68].

In 1960, A first observation of the ion enhancement from Ag or Cu target was discussed with a polyatomic ion bombardment (e.g. H_2^+ and H_3^+) [69, 70]. The study of the cluster as primary ions can be traced by 1989. Blain et al. reported that using keV $(CsI)_mCs^+$ (m=1-10) could gain enhanced molecular ion yields when bombarding to phenylalanine. The ion yield enhancement of organic substrates was also reported in the same year when using SF_6^- as the primary ions [71]. Various ion cluster sources have been developed and applied for surface analysis since that time [72-74]. Prominent

among there is the demonstration of C_{60} and Au_{400} as an efficient projectile. The work of Texas A&M University has resulted in the development of an instrument.

In using, a C_{60} effusion source produces C_{60}^{+} or C_{60}^{2+} cluster ions [75, 76]. The still more efficient Au_{400}^{4+} is the result of collaboration between the Institut de Physique Nucléaire d'Orsay and Texas A&M University. The Au instrument is composed of a 20 keV Au liquid ion metal source coupled to a high voltage (100 kV) "Pegase" acceleration platform to generate from Au^{+} to Au_{400}^{4+} projectiles with total impact energies of up to 120 qkeV [77, 78].

Coincidence methodology in SIMS

The single cluster projectile impact produces multiple secondary ions enabling surface analysis in the event-by-event bombardment/detection mode. In this mode, the mass spectrum of an ionized ejecta within a volume of 10^3 nm^3 is recorded from each impact as an event. In a single event, secondary ions are co-localized from the same emission site. The operation of coincidence methodology will be further discussed in Chapter II.

Our research group has first applied the coincidence concept with SIMS and applied it in several research areas [79, 80]. Early studies include measurements of the surface homogeneity of polystyrene and NaF mixtures [80], the identification of emitted secondary ions and electrons from the thin films of phenylalanine and its deuterated product [81], and the fragmentation and recombination process of primary projectiles on isotopic labeled glycine within a nano-volume domain [82, 83]. Recent studies also

showed that ion mass spectrometry could be used to test molecular mapping of lipids on native biological surfaces has been reported without surface preparation [84, 85], the limits of detecting chemical homogeneities [86-88], and co-localization of bio-related molecules in PEG-collagen micro-patterns [89-91]. A first observation of the co-emission of photons and electrons with secondary ions from fluorescent proteins demonstrates the multi-faceted correlated information generated by nanoprojectile impacts [92, 93].

Nanodomain analysis

The aim of the present study is to combine the efficiency of massive projectiles, especially C_{60} and Au_{400}, with the couple of event-by-event bombardment-detection for the analysis of nano-volumes. In this approach, a single C_{60} or Au_{400} causes desorption of matter from a surface area of 10-20 nm in diameter. The identity of the ionized ejecta is determined via time-of-flight mass spectrometry. The bombardment-detection event is repeated (e.g., at a rate of 10^3 events/s for 10^3s) enabling stochastic probing of an ensemble of nanodomains or objects. The result is an array of records from which one can extract subsets of data that correspond to like-domains/objects with sufficient statistics for molecular characterizations. Notably, this approach identifies molecules co-localized within 10-20 nm. The depth of emission is less than 10 nm. A single Au cluster projectile impact thus generates ion emission from a volume $\leq 10^3$ nm^3.

The instrumentation and methodology are discussed in detail in the following chapter. Followed by accounts of studies devoted to (i) nanodomain analysis of macromolecular

architectures, (ii) a surface co-localized analysis of modified plant surfaces, and (iii) surface adsorption and coverage kinetic study of the self-assembled monolayer.

CHAPTER II

INSTRUMENTATION AND METHODOLOGY

Au-cluster mass spectrometer

A diagram of the Au_{400}^{4+} instrument is shown in Figure 2.1 and 2.2. The Au liquid metal ion source (Au-LMIS) and high voltage platform were developed at the Institut de Physique Nucléaire d'Orsay (IPN in Orsay, France) [77, 94]. In this platform, the Au-LMIS is floated to 20 kV as the primary ion source (Figure 2.1). The Au ion beam is generated by heating a tungsten reservoir and needle assembly filled with an Au/Si eutectic. Then it is capable of producing clusters with 3-1000 atoms and beam currents as high as 200 nA depending on the projectile [95]. The Au cluster beam is mass selected using a Wien filter. A Wien filter is used in mass spectrometry to select different ions based on their velocity. This device consists of orthogonal electric and magnetic fields so that ions with the correct velocity will be unaffected while others will be deflected [96]. It is used to select the desired primary projectiles in our SIMS systems. For example, Au_{400}^{4+} ions can be mass-selected with a Wien filter. The Au_{400}^{4+} ion beam is subsequently accelerated, focused, and collimated to ~200 μm in diameter. As a result, the Au_{400}^{4+} beam with 120 qkeV total energy at the exit of the platform and the entrance to the analysis chamber. The typical beam current of the primary Au ion beam measured with a Faraday cup is of ~200 nA.

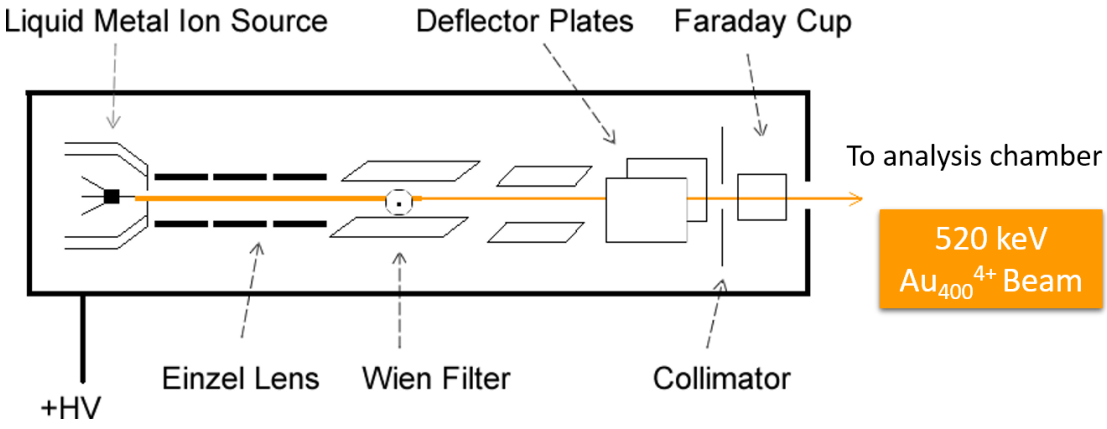

Figure 2.1 Schematic diagram of the Au liquid metal ion source chamber and the high voltage platform.

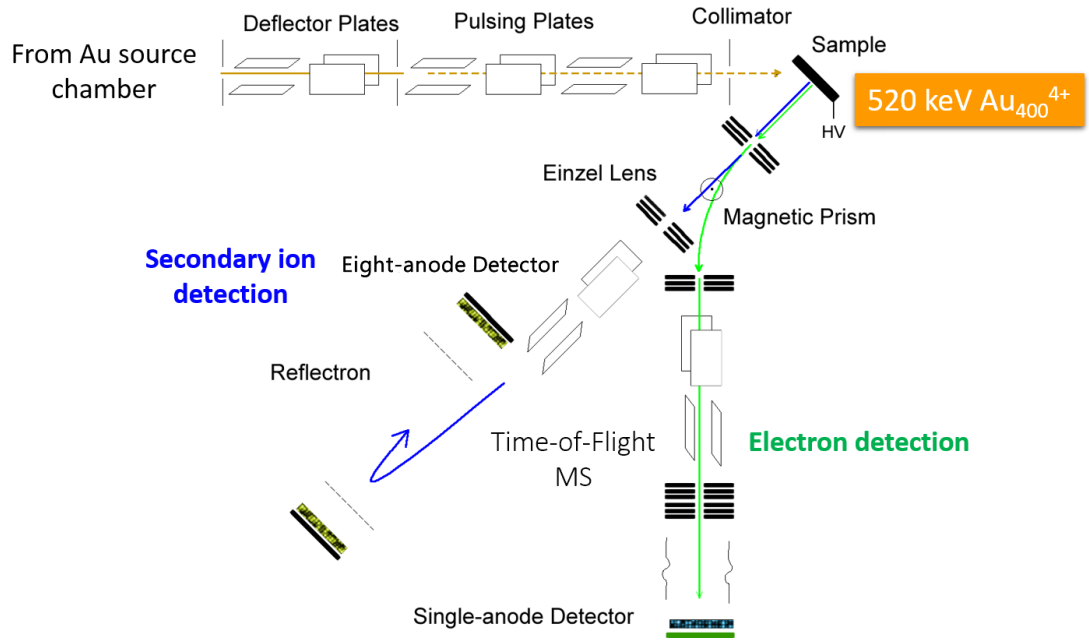

Figure 2.2 Schematic diagram of the Au SIMS analysis chamber.

The analysis chamber and the mass spectrometer as shown in Figure 2.2. In the analysis chamber, the Au ions are first deflected to pass through a collimator with a range of 200 μm to 5 mm in aperture sizes. The Au ion beam is then deflected by the deflector plates to go through another collimator (500 μm or 200 μm slit). The Au ion beam then enters a pulsing system that comprises a set of horizontal and vertical pulsing plates (from –1000 V to +1000 V) at the frequency rate of 3 kHz. The purpose of applying the pulsing system is to obtain the start signal for the acquisition of the time-of-flight measurement. More importantly, it reduces the ion beam current and converts the continuous ion beam to individual projectiles to achieve the nanodomain analysis and the event-by-event bombardment/detection later. After pulsing, massive Au projectiles are further accelerated to 130 qkeV when impacting on a negatively biased target at 10 kV. The angle of incidence of the projectile is 45° off normal, and the emission current of Au_{400}^{4+} projectiles measured on the target is few nanoamperes. The bombardment detection sequences were run at a rate of ~1000 projectiles per second to ensure single projectile impact. The secondary electrons are steered by a magnetic field and then focused onto an electron detector using a dual microchannel plate (MCP) assembly. They provide the start signal for the time-of-flight measurement [84]. Simultaneously ejected negative secondary ions (SIs) were analyzed with a custom-built reflectron time-of-flight mass spectrometer with an eight-anode MCP detector.

The MCP is a lead-doped disk-shaped glass electron multiplier with ~10 μm diameter channels arranged at 12° to normal. The outside diameter of the MCP is 50 mm with the active area of ~40 mm in diameter and a thickness of 0.46 mm. The chevron type of

MCPs is used to amplify signals from the impacts of electrons and ions [97, 98]. Figure 2.3 shows the chevron MCPs assembly with the single or eight-anode detector. The first MCP generates a gain of electrons up to ~10^3, and a total gain of ~10^6 electrons is achieved across two MCPs. The resistance between the electrodes in MCPs is on the order of 10^9 Ω. The eight-anode detector allows for the detection of up to eight isobaric ions per event. A large active area detector is developed to improve the detection efficiency of SIs. The mounting scheme also has a better mechanical stability that reduces the probability of MCP breakage over the previous generation detectors. The anode is based on previous designs that utilize printed circuit board (PCB) technology to form isolated conductive surfaces on top of an insulating substrate [99, 100]. The PCB material between the conductive anodes is removed to reduce charge accumulation from electron fluxes that are deposited on the insulating layer. Figure 2.4 shows different types of PCBs for the eight-anode detector. The anodes independently transmit the transient voltage spikes from the MCP output to signal processing electronics. In this way, the dynamic range of the pulse counting detector is determined by the number of individual anodes. An eight-anode detector is used here as a secondary ion detector coupled to a custom-designed time-to-digital converter (TDC) containing eight separate processing ports [77, 94].

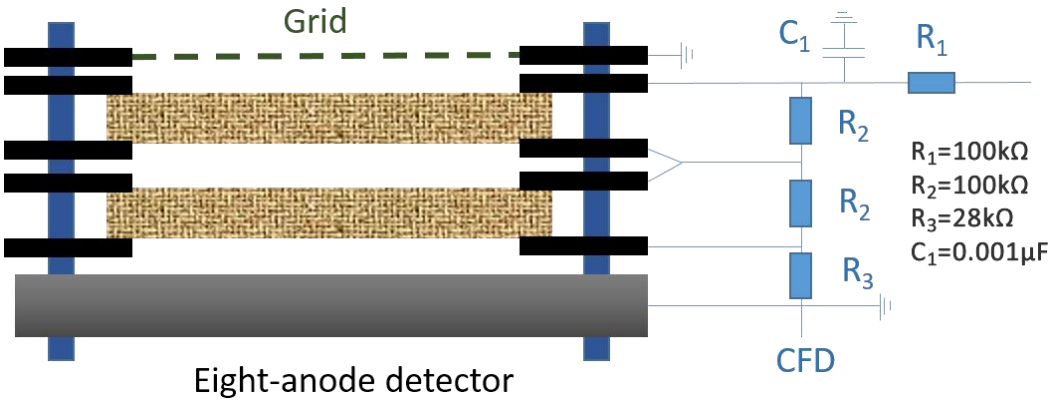

Figure 2.3 Assembly diagram of Au cluster SIMS stop detector.

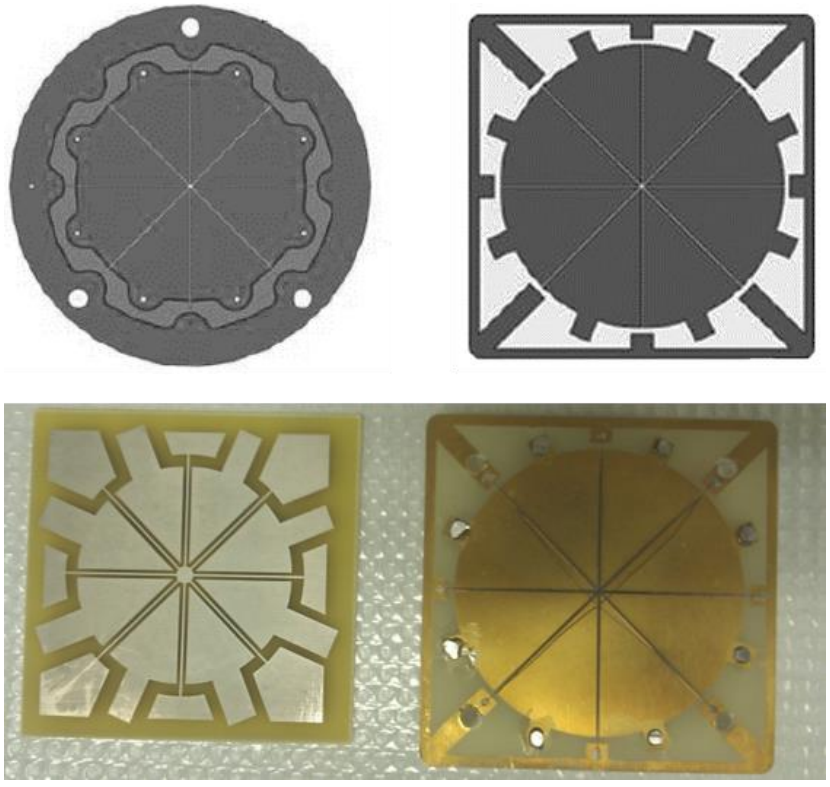

Figure 2.4 Different types of eight-anode detector PCB designs.

C_{60} mass spectrometer

As indicated earlier, the C_{60} time-of-flight SIMS instrument is a custom-built instrument. A schematic of this C_{60} SIMS is shown in Figure 2.5. The primary ion part of C_{60} is isolated from the secondary ion analysis part with a gate valve.

An electron impact ionization of C_{60} is used to produce positive C_{60} primary ions. A neutral C_{60} powder in a copper reservoir is heated up to ~450 °C to generate primary C_{60} ions. The gas phase C_{60} effuses into a cylindrical electrode and is ionized by the electron impacts from a heated tungsten wire. The charged C_{60} clusters are then extracted with a potential gradient between the C_{60} effusion source and the extraction plate. The C_{60} ions are focused and accelerated toward the ground with a pair of electrostatic lenses. Then a mixture of C_{60} ions is mass selected for specific primary ions with a Wien filter. The selected C_{60}^{2+} ions are then steered into a ~1mm in diameter aperture to deflect other ions and neutrals on the targeted sample. C_{60}^{2+} projectiles with a total energy of 50 keV toward the target after passing through a set of horizontal and vertical plates. Similar to the Au cluster SIMS system, the resulting secondary electrons are deflected by a magnetic field toward an MCP electron detector and is used as a start signal. The negative secondary ions enter into a linear time-of-flight analyzer with the same velocity and are then detected by an eight-anode detector as stop signals. The data collection and acquisition system is the same as the Au cluster SIMS system, and details will be discussed in the following section.

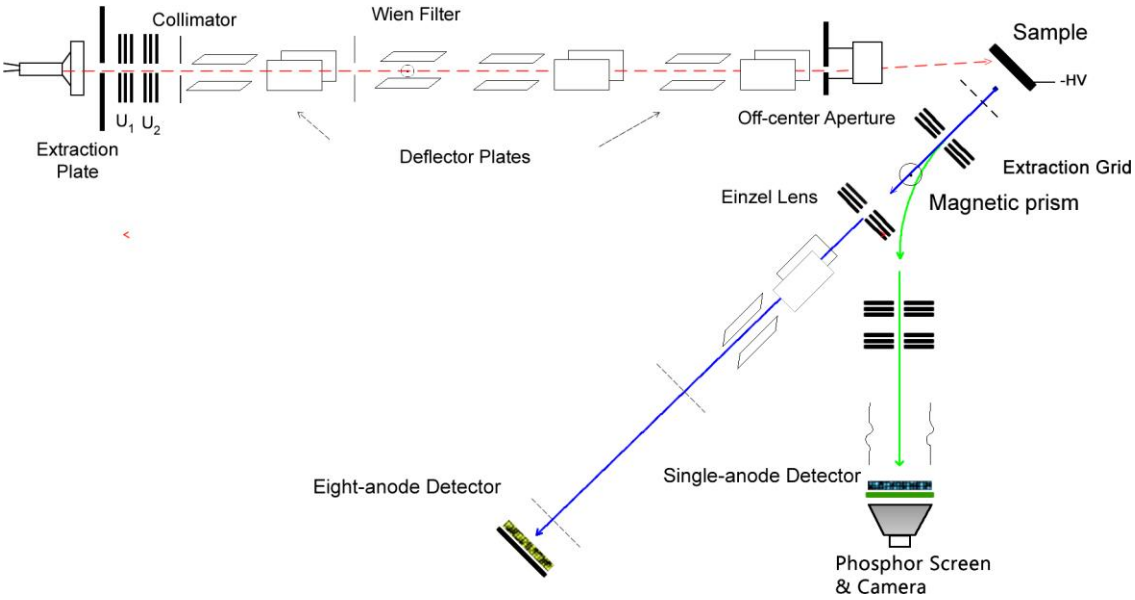

Figure 2.5 Schematic diagram of the C_{60} SIMS instrument.

Time-of-flight mass analyzer

Time-of-flight mass analyzer is a device to determine the mass-to-charge ratio of ions via a time measurement. Before the analysis, ions are accelerated by an electric field. This acceleration results in an ion having the same kinetic energy as any other ions that have the same charge. So the velocity of the ion depends on the mass-to-charge ratio [101, 102]. The time that it subsequently travels from the starter to a detector is recorded. The mass calculation is the total time of arrival to the mass-to-charge ratio:

$$t = k\sqrt{\frac{m}{q}} \qquad 2.1$$

A dual-stage reflectron time-of-flight analyzer (IPNO) [77, 94] is equipped with the Au cluster SIMS system. A general reflectron analyzer uses a constant electrostatic field

to reflect the ions toward the detector. The ions with higher energy penetrate deeper and take a slightly longer path to the detector. While, less energetic ions with the same mass-to-charge ratio penetrate a less distance to the detector. The ion mirror in a dual-stage reflectron has two regions with different electric fields, which enables the adjustment for both the first and second derivatives of time to be zero. This dual-stage is also designed to allow for the tilt about the transverse horizontal and vertical directions using vacuum positioners. This capability allows the detection surface of the MCP detectors to be aligned parallel to the sample surface, therefore maximizing improved the mass resolution in reflectron mode. More detailed setting ups are discussed elsewhere [77, 94, 103]. A linear mode of time-of-flight analyzer is equipped with the C_{60} SIMS system. This device is simpler than the dual-stage reflectron, which details are also discussed [104].

The mass resolution, R, to resolve two mass spectral peaks is defined as:

$$R = \frac{t_{tot}}{\Delta t} = \frac{m}{\Delta m} \qquad 2.2$$

Where t_{tot} is the total time of flight, and m is the mass of the given ion. The Δt and Δm are the full widths of the time or mass peak at half the maximum intensity, respectively [105]. The actual mass resolution is ~800-1,200 at *m/z* 12 using the reflectron analyzer.

Signal processing

The single-anode detector collects the electron cascade. Signals from the electron detector are processed with a quad Constant Fraction Discriminator or CFD. The output secondary ions signals are transmitted into an octal CFD as well. The CFD is used to

eliminate the ringing signal due to different arrival times and amplitudes by setting minimum input pulse amplitude on the CFD threshold. Thus, the discriminator can enhance the time resolution with a fixed trigger threshold, walk or Z/C adjust and constant width. CFD also converts the analog signal to a Nuclear Instrumentation Module (NIM) and a logic square wave pulse. A detailed discussion of the CFD has been described elsewhere [100].

The electron output signal from the CFD is collected into the start input port of the TDC, which triggers the acquisition of secondary ion signals from the octal CFD as stop signals. The TDC records the appearance time of stop signals at the start with a time resolution of 250 or 400 picoseconds per channel. Also, the TDC converts the logic pulse signal from the CFD to a digital signal. The data could be then stored on a personal computer and processed with the Surface Analysis and Mapping of Projectile Impacts (SAMPI) software [106, 107]. Figure 2.6 demonstrates the working process of the SAMPI. All emitted ions generated from a single projectile impact are saved separately in a row space of the matrix as an event. The number of the events could be up to several million. A total secondary ion mass spectrum is therefore obtained with the sum of the total events of secondary ions. There is no different between the total ion mass spectrum and the conventional mass spectrum that derived from traditional SIMS systems. Also, the SAMPI and the event-by-event bombardment-detection mode enable to create a mass spectrum co-emitted with a selected ion. This type of the secondary ion mass spectrum is different from the total secondary ion mass spectrum, which is recognized as the coincidence mass spectrum.

Event-by-event bombardment-detection mode

As discussed, the single projectile impacts in a stochastic fashion on the sample surface in both Au cluster and C_{60} SIMS systems. Each primary projectile impact on the target surface leaves a nano-volumetric crater. The molecules residing inside the crater are fragmented and ejected during each impact. The secondary ion emission volume of a single projectile impact is estimated to be ~10^3 nm^3 [91, 108]. The co-ejected/co-emitted secondary ions from each impact are resolved separately as an "event." The definition of the event is that the resulting electrons as a start signal and the detection of resulting secondary ions with a single projectile impact. The bombardment detection sequences were run at a rate of ~1000 projectiles per second. The SIMS analysis is conducted in the super-static regime, where less than 0.1% of the total surface is impacted. This regulation ensured that each time the surface was impacted by a primary projectile, an unperturbed area of the surface was sampled [93, 109]. Figure 2.6 shows the event-by-event bombardment-detection mode and coincidence mass spectrum.

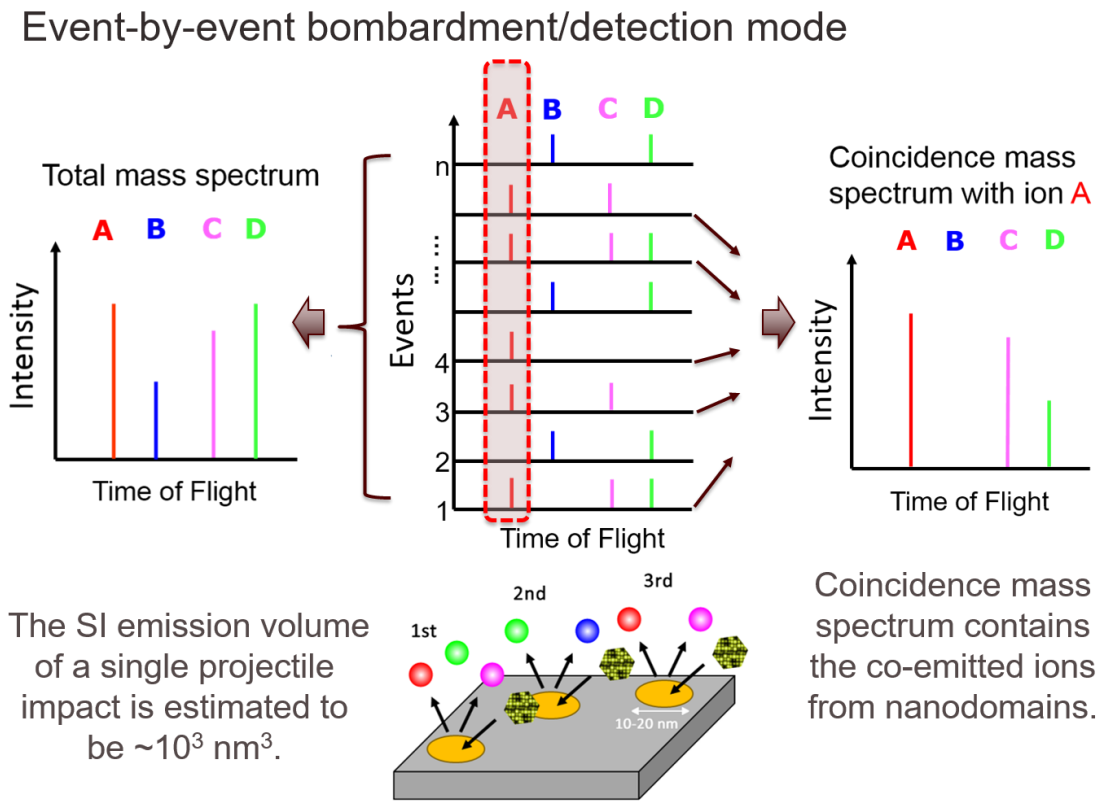

Figure 2.6 Schematic diagram of event-by-event bombardment-detection mode and coincidence mass spectrum.

Our research group introduced the coincidence counting technique combined with time-of-flight SIMS [80, 110]. The impacted region should be small enough to resolve the component or domain from one another. Moreover, each domain should generate an individual secondary ion signal to allow chemical identification. In the operation of the event-by-event bombardment-detection mode, co-localized molecules from the nanoscopic areas or nanodomains could be identified with a single projectile impact by the coincidence secondary ion mass spectrum. Coincidence mass spectrum contains the

co-emitted ions from nanodomains. Once specific ions of are identified from molecules, the measurement of coincidence emission of two specified ions allow for a variety of applications in the analysis of thin film surface coverage and homogeneity.

Surface coverage and homogeneity analysis

To estimate the surface coverage of assigned species, we use a method based on coincidence counting [109]. As noted earlier, the individual events are recorded that allows extracting the coincidence mass spectra, i.e., the co-emitted ions with a selected ion of interest [93, 111]. For a secondary ion from a mass spectrum, i.e., ion A, the yield of ion A, Y_A, is defined as:

$$Y_A = \sum_{x_A} \frac{x_A N_{(x_A)}}{N_0} = \sum_{x_A} x_A P_{(x_A)} = \frac{N_A}{N_0} \quad 2.3$$

where x_A is the number of detected ions A in an event, $N_{(x_A)}$ is total number of events when ions A was detected, N_0 is the total number of impacts, $P_{(xA)}$ is the probability distribution of detected ions A per single impact, N_A is the overall number of ion A from SAMPI. Once another secondary ion, i.e., ion B, is involved, the concept of correlation coefficient is introduced to determine the extent of the correlation in secondary ion co-emissions. The correlation among co-emitted secondary ions can be quantified with a coefficient, Q, which is defined as follows:

$$Q_{A,B} = \frac{\sum_{x_A} \sum_{x_B} x_A x_B P_{(x_A x_B)}}{\sum_{x_A} x_A P_{(x_A)} \sum_{x_B} x_B P_{(x_B)}} \quad 2.4$$

where x_B is the number of secondary ions detected for B. $P_{(xAxB)}$ is the probability distribution of the number of ions A and B that are detected simultaneously. $P_{(xB)}$ is the probability distribution of detected ion B.

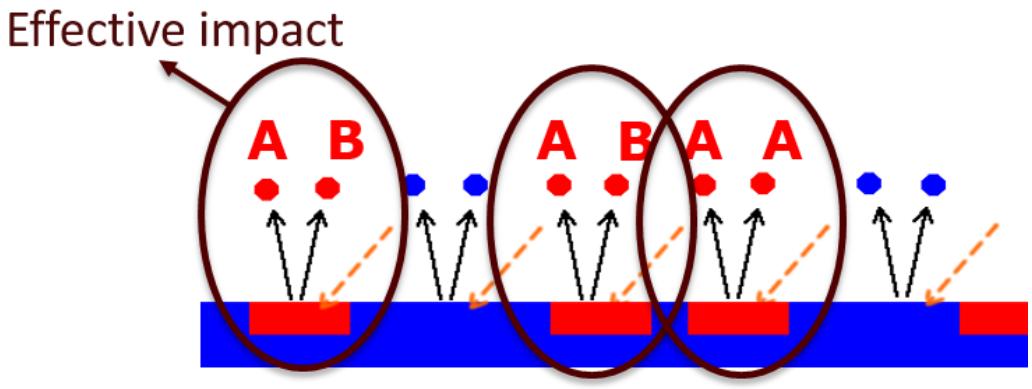

Figure 2.7 Schematic illustration of the effective impact.

When two types of ions, A and B, are emitted independently from the same compound or functional group, that is to say, the emission of ion A is independent of the coincidence ion B, they should have a correlation coefficient ($Q_{A,B}$) of unity. $Q_{A,B}$ can be expressed as follows:

$$Q_{A,B} = \frac{Y_{A,B}}{Y_A^{eff} \times Y_B^{eff}} = 1 \qquad 2.5$$

where $Y_{A,B}$ is the coincidence yield of simultaneously detected ions A and B; and Y_A^{eff} and Y_B^{eff} are the effective yields of detected ions A and B, respectively. The coincidence yield $Y_{A,B}$ is defined as follows:

$$Y_{A,B} = \frac{N_{A,B}}{N_e} \quad 2.6$$

where $N_{A,B}$ is the number of co-emitted ions A and B in their coincidence mass spectrum, and N_e is the effective number of impacts on a particular specimen (Figure 2.7). Similarly, Y_A^{eff} and Y_B^{eff} are defined as follows:

$$Y_A^{eff} = \frac{N_A}{N_e} \quad 2.7$$

$$Y_B^{eff} = \frac{N_B}{N_e} \quad 2.8$$

where N_A and N_B are numbers of ions A and B, respectively. Using Equations (2.6)-(2.8), the number of effective impacts, N_e, is expressed as follows:

$$N_e = \frac{N_A \times N_B}{N_{A,B}} \quad 2.9$$

The effective number of impacts is independent of ionization probabilities and detection efficiencies of ions A and B. For an object with the much larger area than the emission volume, their surface coverage can be calculated using the coincidental process [88, 93, 111]. Therefore, the surface coverage of specimens (K) is given by

$$K = \frac{N_e}{N_0} \times 100\% \quad 2.10$$

As discussed, Equation (2.4) can be used to investigate the correlation in secondary ion co-emissions, as well as the homogeneity of the surface. Assume ions X and Y are from different species or functional groups on the surface. The correlation coefficients correlated to the homogeneity of chemicals are summarized as follows: If X and Y are independently emitted from single impacts, then, $Q_{x,y}=1$, i.e., the emission of X and Y is uncorrelated; When $Q_{x,y}>1$, the emission of ions X and Y is correlated. On the contrary, when the emission of ions X and Y is anti-correlated, ($Q_{x,y}<1$), the emission of ion X

suppresses that of Y or vice versa. For a homogenous thin film surface, the Q value of secondary ions from different functional groups is equal to unity. The limitation of using the correlation coefficient, however, is that the secondary ion emission of ions X and Y is in the same condition under different surface ensembles. To overcome this limitation, we introduce another analytical method to discuss the surface homogeneity. For ion X, we define the total ion yield of ion x is:

$$Y_T = \frac{N_x}{N_0} \tag{2.11}$$

Similarly, the coincidental yield of ion X with ion Y, Y_C, is defined as:

$$Y_C = \frac{N_{X,Y}}{N_B} \tag{2.12}$$

where $N_{x,y}$ is the number of co-emitted ions X and Y, and N_B is the number of ion B. The ratio of Y_C to Y_T can be used to describes the co-localized/co-emitted condition of selected ions. When Y_C/Y_T is larger than 1, it means selected ions (ions X and Y) are co-located and co-emitted from the surface. Once Y_C/Y_T equals to unity, selected ions have no relation with one another.

CHAPTER III

NANODOMAIN ANALYSIS OF MACROMOLECULAR BRUSH ARCHITECTURE*

Introduction

The rapid growth in macromolecular materials for advanced photoresist applications provides continuing characterization challenges. Physical and chemical analysis become difficult at a surface or interfacial realm of less than 50 nm, where spatial variability has a substantial influence on the behavior of the entire system [112-115]. SIMS, as a non-destructive surface analysis technique, was first used for characterizing polymers over 30 years. Its unique capabilities, which includes molecular specificity, high surface sensitivity, and sub-micron resolution, could provide both compositional and structural information of the polymeric surface [115]. In the last decade, the instrumental research and development of SIMS opened new perspectives for the nanoscopic studies [116]. We focus here on Au cluster-SIMS in the event-by-event bombardment/detection mode, i.e., it operates as a nanoprobe and is thus well suited for the nanodomain characterization of polymers.

---

* Parts of this chapter were reprinted with permission from *Surface and Interface Analysis*, Volume 47, pages 1051-1055, Fan Yang, Sangho Cho, Guorong Sun, Stanislav V Verkhoturov, James W Thackeray, Peter Trefonas, Karen L Wooley, Emile A Schweikert "Nanodomain analysis with cluster-SIMS: application to the characterization of macromolecular brush architecture." Copyright [2015] John Wiley & Sons, Ltd.

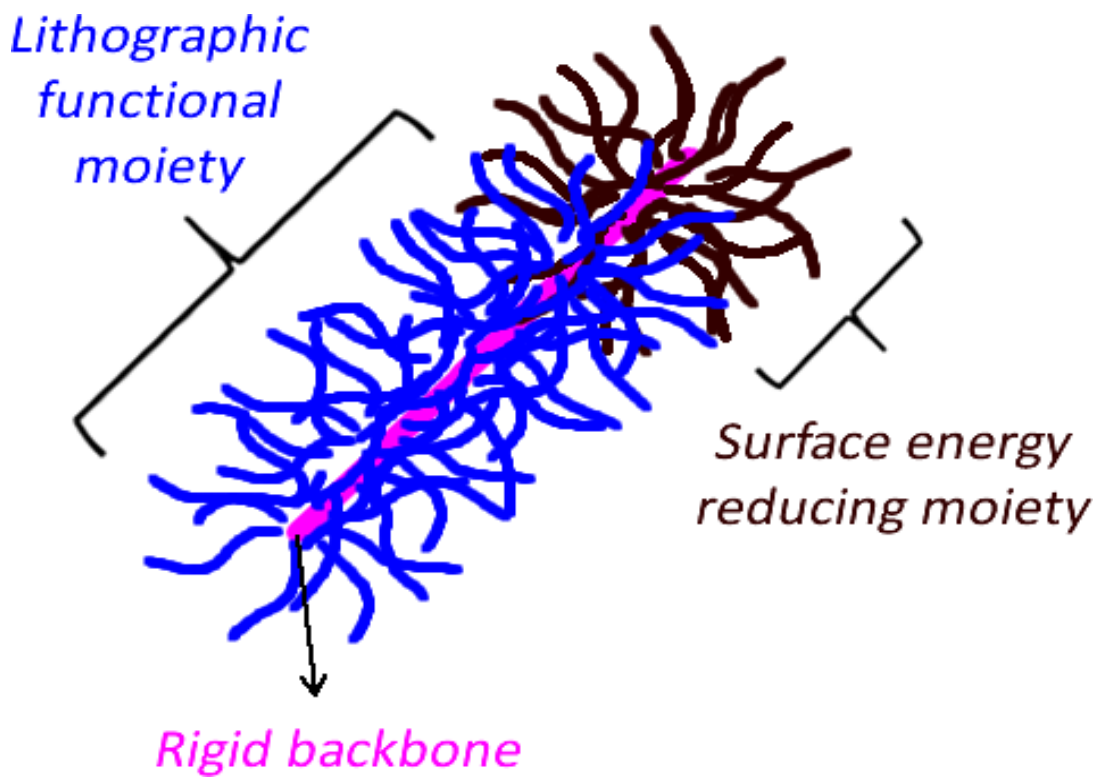

Figure 3.1 The structure of a single diblock brush terpolymers.

The materials investigated here are direct self-assembled diblock brush terpolymers (DBTs), which allows for high-resolution lithography. The DBT architecture consists of a rigid backbone linking to side brush chains. The placement of brush chains of different compositions, along with the relative concentric and lengthwise dimensions, aligns and controls the various functional moieties. Figure 3.1 illustrates a design of a DBT polymer unit. It is formed by sequentially adding the first type of homo-brushed monomers with the same set of functional groups for substrate alignment, followed by adding another homo-brushed monomers to supply the needed lithographic crosslinking and development control properties. An entire DBT unit is a brush-like cylinder. It contains

moieties of surface energy reduction blocks and functional lithographic segments, which are linked to a rigid backbone. We hypothesized that it would be possible to assemble these into a vertically aligned arrangement of these DBTs without the need to guide large-scale supramolecular assembly as is required in conventional linear block copolymers for direct self-assembly.

The ordered DBT films often achieved by the process of the direct self-assembly. It offers a route to increased order in the thin film and create patterns that are useful for the lithography (e.g. oriented cylindrical or lamellar domains). A vertically aligned film of DBTs improves the resolution of electron-beam lithography etching to sub-30 nm. Thus, their evaluation and characterization must be performed at the nanoscale.

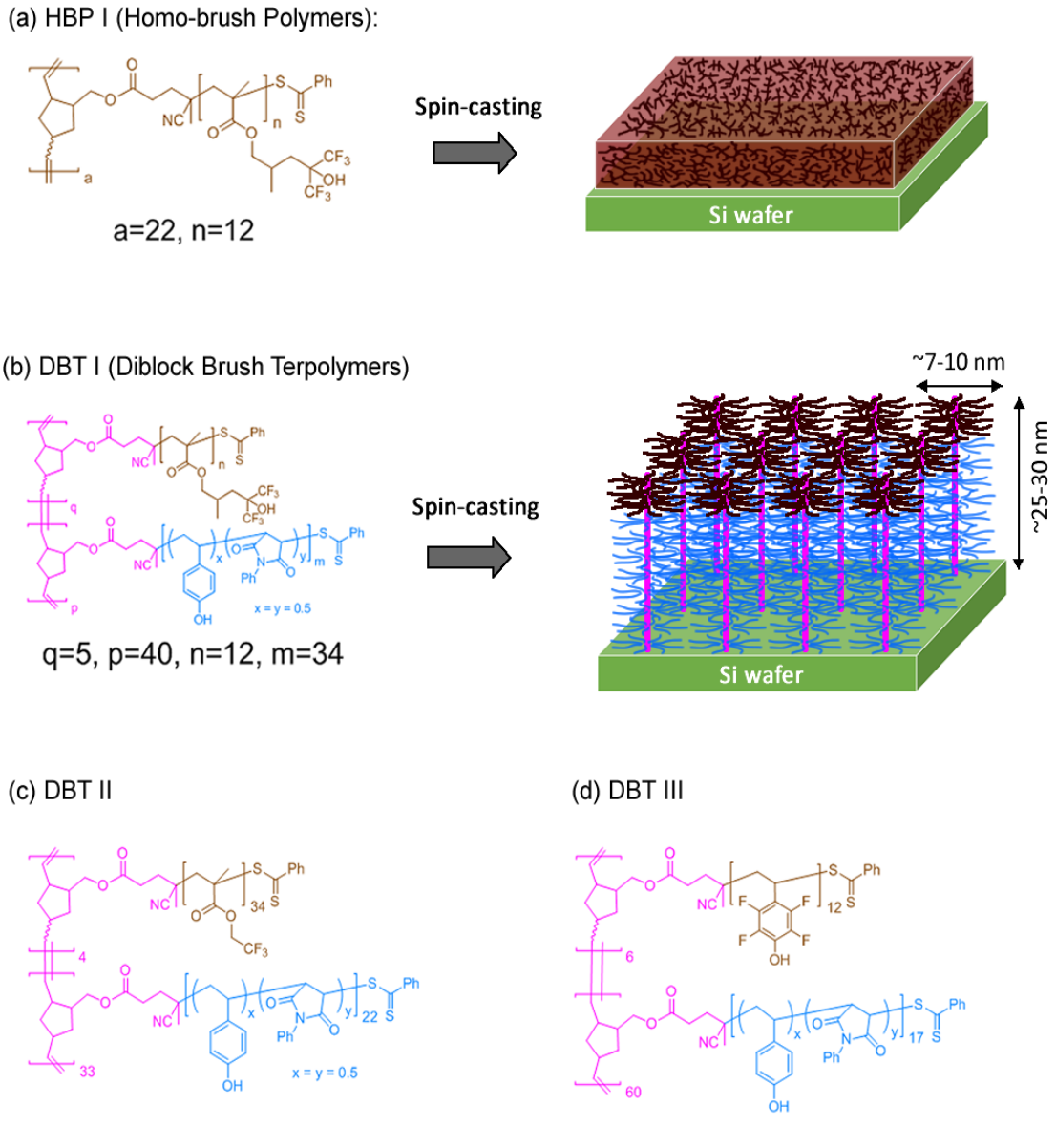

Figure 3.2 Chemical structures and estimated the dimension of (a) HBP I, (b) DBT I, (c) DBT II and (d) DBT III.

Experimental section

Preparation of homo-brushed polymer and diblock brush terpolymers thin films

The synthesis details of homo-brushed polymers (HBPs) and DBTs have been discussed elsewhere [117, 118]. The chemical structures of them are presented in Figure 3.2. The homo-brushed polymer NB-poly(1,1,1-trifluoro-2-(trifluoromethyl)-2-hydroxy-4-methyl-5-pentyl methacrylate) was synthesized as a reference for comparison with the surface component and structure of the DBT I. DBT I composed of dense poly(2,2,2-trifluoroethyl methacrylate) block segments and poly(p-hydroxystyrene-co-N-phenylmaleimide) block segments were tethered along with a rigid polynorbornene backbone. Fluorocarbon segments functioned as vertical alignment promoters, and the phenol-related segments performed to provide attractive interactions with the substrate and served as reactive sites for other reactions. The design and structure of DBT II and III are similar to DBT I, but they own different fluorocarbon functional groups. The fluorocarbons are poly(1,1,1-trifluoro-2-(trifluoromethyl)-2-hydroxy-4-methyl-5-pentyl methacrylate) for DBT II and poly(tetrafluoro para-hydroxy styrene) for DBT III.

HBP or DBT thin films were deposited by spin-casting with their 1.0 wt. % solutions in cyclohexane onto cleaned silicon wafers. The silicon wafer was cut into approximately 1×1 cm^2 pieces for the SIMS analysis. The thickness of the DBT film, as measured through atomic force microscopy, was used as a monolayer.

Cluster-SIMS and the event-by-event detection

The DBT and HBP films were examined with 520 keV Au_{400}^{4+} ToF-SIMS instruments operated in the event by event bombardment-detection mode. The detailed discussion is in Chapter II. The bombardment detection sequences were run at a rate of ~1000 projectiles per second. Total mass spectra were obtained by an accumulation of several million events. As noted already, the SIs originating from individual impacts were recorded separately [80]. The data acquired in this event-by-event mode were processed with custom developed software (SAMPI) [100]. Co-emission mass spectra including an SI of interest were extracted from the records of the individual impacts [81, 119]. This procedure identifies molecules co-located within 10-20 nm in a non-mapping mode.

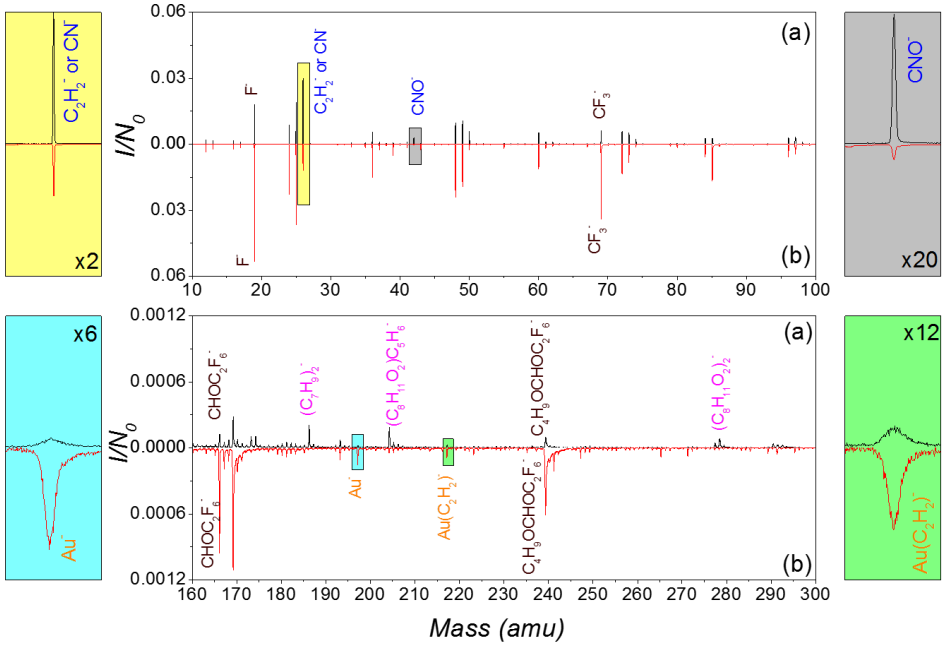

Figure 3.3 Comparison of negative ion mass spectra of (a) DBT I and (b) HBP I.

Results and discussion

SI emissions of DBT and HBP thin films

The HBP I are deposited as random films with a total thickness of at least 20 nm, i.e. above the range of the Au_{400}^{4+} projectiles in Figure 3.2a. The DBT monolayer forms an idealized morphology in a closed packed order, and DBT cylinders align vertically on the surface. As shown in Figure 3.2b, the diameter and length of each DBT I cylinder are estimated about 7 to 10 nm and 25 to 30 nm, respectively. We note that the graft on the brush could be interdigitated or in a more coiled conformation. Figure 3.3 shows the negative secondary ion mass spectra for DBT I and HBP I, each obtained by summing SIs from ~4 million impacts. The ion peaks from fluorocarbons at *m/z* 19 (F^-), 69 (CF_3^-), 167 ($C_2F_6CHO^-$), and 239 ($C_2F_6OC_5H_9O^-$) are present in both mass spectra. They originate from the fluoroalkyl groups on the side chains bound to the top-layer DBT I films and from the entire HBP I films. Ion peaks at *m/z* 121 (*ph*CS^- or $C_{10}H^-$) and 153 (*ph*CSS^-) correspond to alkanethiol groups at the end of each segmental graft. The DBT films further show series of SI emissions of carbon-based clusters, C_n^- and C_nH^-, ($1 \leq n \leq 16$). For odd numbers of *n*, ion clusters of C_n^- predominate over the C_nH^- that holds for clusters with even numbers of *n* [86, 87]. The trends for C_n^- versus C_nH^- are different in the HBP I samples due to compositional differences and the fact that these films are neat.

SIs from the bottom segment grafts of the DBT sample were also presented on the mass spectrum of the DBT I films. The ion peaks at *m/z* 26 (CN^- or $C_2H_2^-$), 42 (CNO^-) and 119 (*ph*NCO^-) are *N*-phenylmaleimide-related ions, which are from side-grafts in a deeper area. The ion intensities of CN^- and CNO^- in the mass spectrum of the HBP I

films are not as significant as those of the DBT I films. It infers no *N*-phenylmaleimide groups in HBPs. Meanwhile, the mass spectrum of the HBP films does not exhibit at *m/z* 205 [$(C_8H_{11}O_2)C_5H_6^-$], 278 [$(C_8H_{11}O_2)_2^-$], and 290 [$(C_8H_{11}O_2)_2C^-$], which implies that the corresponding samples do not contain rigid polynorbornenyl backbones. The different SI emissions from the DBT films suggest that their surface compositions and structure are distinct from the HBPs.

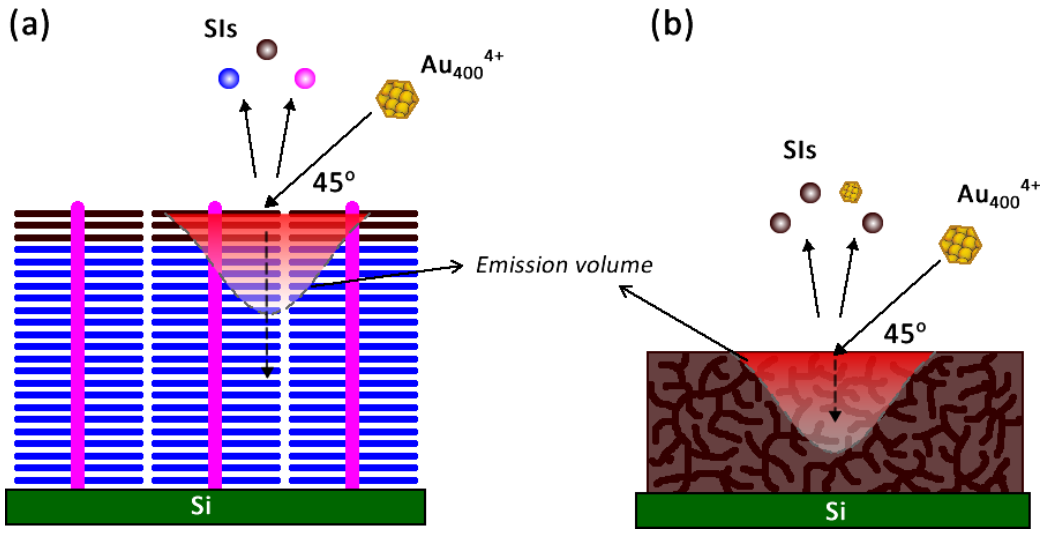

Figure 3.4 Au_{400}^{4+} impacting on (a) ordered arrangement DBT and (b) on HBP in a random arrangement.

The unique surface structure of DBT nanodomains also influences the projectile-related ion emissions. A common occurrence in Au_{400}^{4+} bombardment is the emission of Au^- and Au-adducts [120, 121]. Au^- and $AuC_2H_2^-$ are indeed apparent in the HBP mass spectrum. In contrast, there are no Au-related signals evident in the DBTs spectrum

(Figure 3.3). We attribute the difference to the low-density architecture of DBTs about the HBP film that is a compact organic solid. The projectiles penetrate deeper into the low-density structures than in a compact surface as sketched in Figure 3.4. The Au ions and Au-adducts are created into more depth in DBT films. Furthermore, the aligned long-chain brushes may hinder the escape of Au-related ions by steric effects or promote the neutralization of low-velocity species. Low-mass ions and electrons have higher escape velocities and will be less affected.

The amount and species of functional fluorocarbon groups determine the surface arrangement of DBT films [118, 122]. Table 3.1 shows fluorine-related SI yields of DBT I and HBP I samples. The SI emission is quantified by the SI yield, defined as the number of the ion of interest normalized to the total number of impacts [111, 123]. SI yields of all fluorine-containing ions of DBTs were lower than those of HBs, which is attributed to the segregation of surface components as well as the low density of DBT films [118, 122]. The fluorocarbons are in the top 3 to 7 nm surface area of the DBT films, as confirmed by depth profiling SIMS measurement. For HBP films, fluorine species are evenly distributed without a surface segregation, which results in larger fluorine-containing SI yields.

Table 3.1 Fluorine-related SI yields for DBT I and HBP I samples.

Detected SIs	*m/z*	SI Yields		Reference Intensity Ratio
		DBT I	HBP I	(Φ)
F^-	19	19%	38%	50%
CF_3^-	69	11%	33%	33%
$C_2F_6CHO^-$	166	0.34%	1.6%	21%
$C_2F_6OC_5H_9O^-$	239	0.43%	1.6%	27%

Fluorinated SIs of DBT samples are compared quantitatively as ratios to their correspondences in HB samples. This ratio (Φ) can be calculated as follows:

$$\Phi = \frac{Y_A}{Y_R} \times 100\% \quad 3.1$$

where Y_A and Y_R are the SI yields of the detected ions from analyte and reference, respectively. The F^- ratio for DBT films was 50%, which is comparable to a previous X-ray photoelectron spectroscopy result with similar components [124]. However, the ratios for larger fluorine molecular ions (CF_3^-, $C_2F_6CHO^-$, and $C_2F_6OC_5H_9O^-$) were substantially lower than that of the F^-. The decrease indicates that the surface morphology of DBTs impedes SI emissions of fluorinated polyatomic fragments.

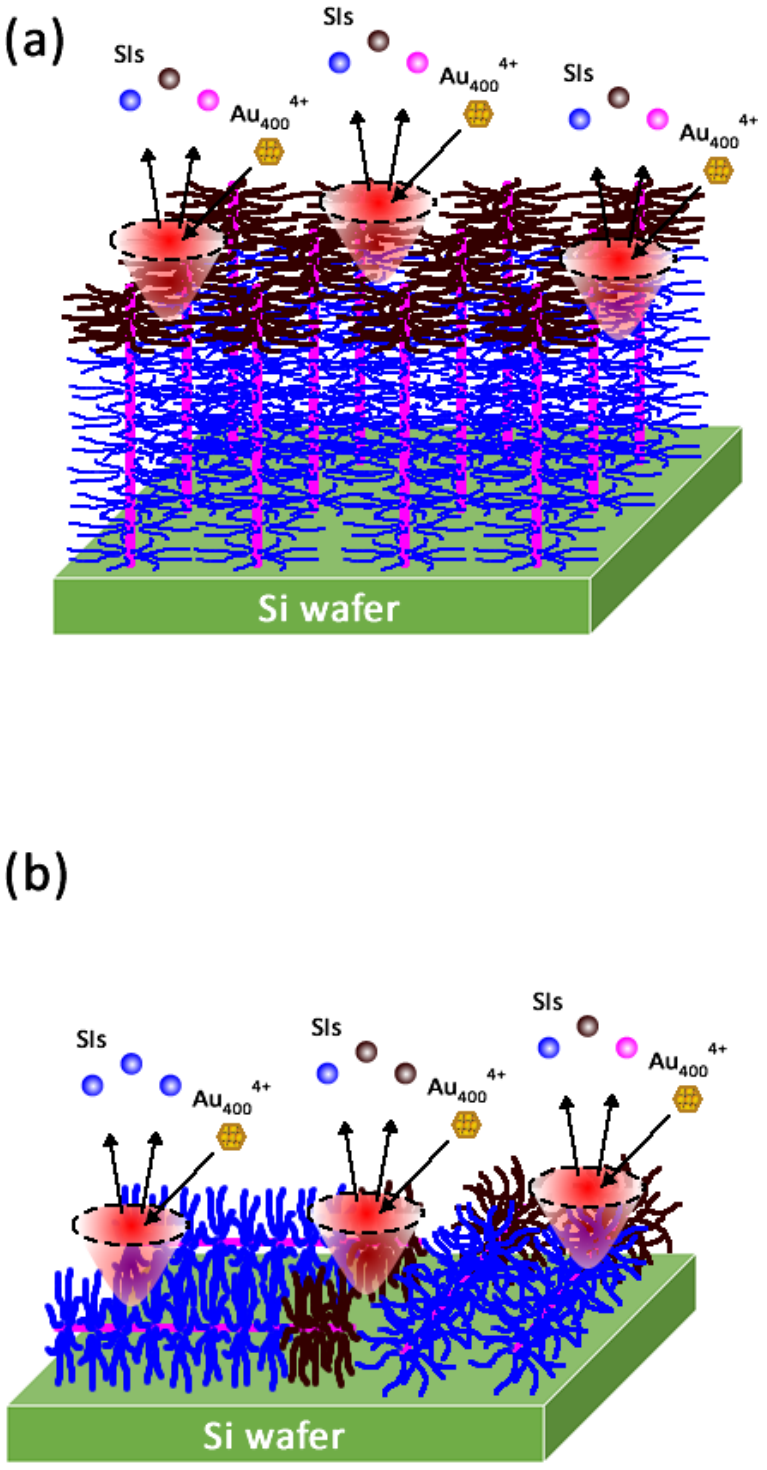

Figure 3.5 Schematic illustration of Au_{400}^{4+} impacting on (a) vertically aligned and (b) "lying down" DBTs on the Si surface.

Comparison surface coverage and homogeneity of DBTs and HBPs

The characterization of the DBT films focuses on their surface assemblies. Figure 3.5 illustrates possible surface assemblies of the DBT cylinders. When DBTs "stands up" as vertically oriented rods, a homogeneous surface develops with the segregation of fluorocarbons. The surface coverage of the fluorocarbon group in this situation would be close to 100%. Co-emitted SIs of the different functional groups in the same DBT brush should show uncorrelated emissions. If the DBTs have slanted orientations, or "lay down" on the surface, the fluorocarbon surface coverage will not be able to reach a high value, and different functional groups of DBTs will not be evenly distributed on the surface.

Taking DBT I films as an example, fluorocarbon-related ions of F^-, CF_3^-, $C_2F_6CHO^-$, and $C_2F_6OC_5H_9O^-$ are chosen to calculate the fractional surface coverage K (%) for the DBT thin films (Equations 2.6 to 2.10). The fluorocarbon surface coverage of DBT I films is ~88%, which is in agreement with previous studies [124]. This result indicates virtually that DBT I owns a complete coverage of fluorinated components, as designed. As a comparison, HBP I films with the same fluorocarbon functional groups shows the full coverage (~93%) as well because they only fluorocarbon side chains. As discussed above, the uniquely aligned structure of DBTs causes the different SI emissions from other organic solids. The co-emitted SIs from various functional groups of DBTs can also validate their distinct surface structures. Only the vertical alignments of DBTs result in the unity. In DBT I films, the Q values for ions from fluorocarbon groups and *N*-phenylmaleimide groups [e.g., $Q(F^-, CNO^-)$, $Q(F^-, phNCO^-)$, $Q(CF_3^-, CNO^-)$, $Q(CF_3^-$,

phNCO$^-$), Q($C_2F_6CHO^-$, CNO^-), and Q($C_2F_6CHO^-$, phNCO$^-$)] were consistently ~1.1. Similarly, Q(F^-, $C_8H_{11}O_2^-$) and Q[F^-, $(C_8H_{11}O_2)_2^-$] from fluorocarbons and polynorbornenyl backbones were also close to unity (~1.1). These results mean functional groups from different parts of DBTs are homogenously assembled on the surface. It infers that DBT nanodomains are most likely as a desired vertically arrangement structure. When measuring the randomly distributed surface of polymer brushes (e.g. HBP I films), single impacts of projectiles will result in different types of SI emissions from the event to event. As a consequence, the Q value of SIs from various functional groups may be no longer close to unity. The value for Q(F^-, $C_8H_{11}O_2^-$) in HBP I is ~1.9, reflecting that HBP surface brushes may curl and fold with each other and unable to form a homogeneous arrangement.

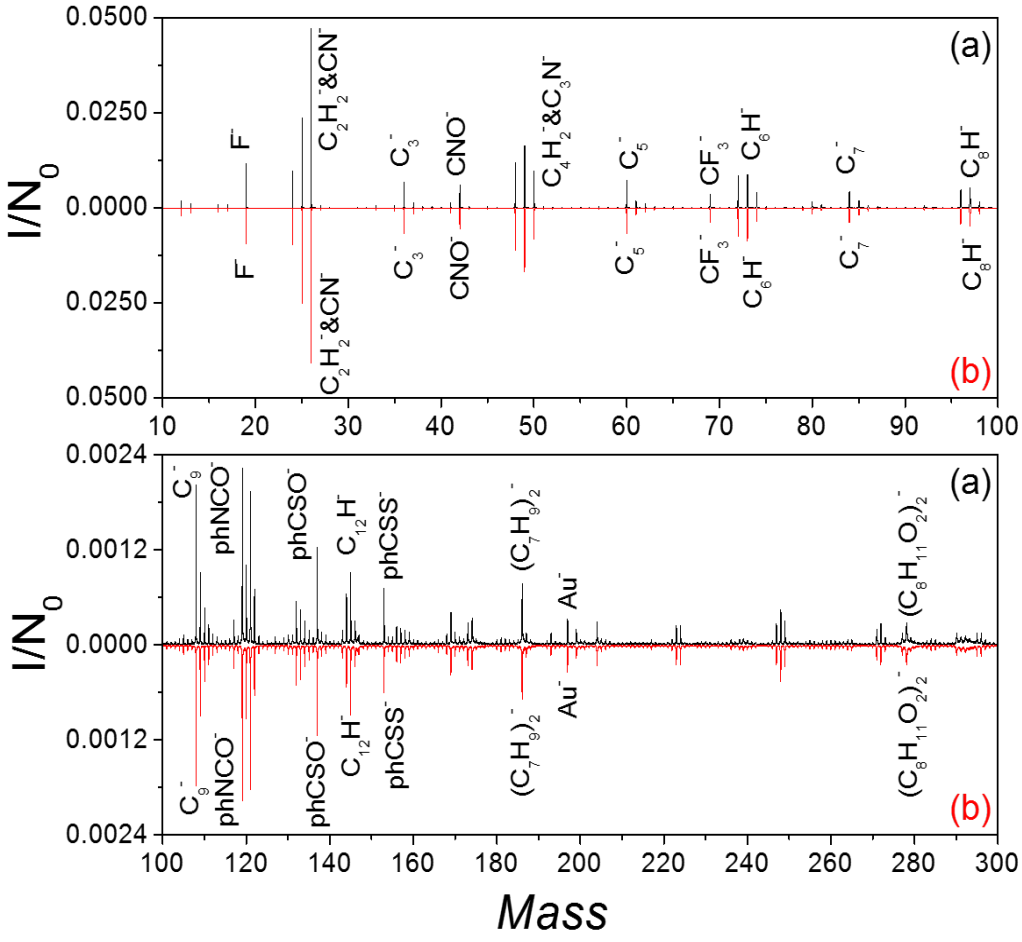

Figure 3.6 Comparison of negative ion mass spectra of DBT II (a) before and (b) after toluene solvent treatment.

Surface analysis of the DBT film processing

Using an appropriate deposition method, the DBTs can form an ordered pattern without any further treatments. However, several physical or chemical processing might afterward re-arrange the surface distributions of DBT nanodomains. The surface changes of DBTs, even it is subtle, could reflect the changes in SI emissions or surface coverages

from the SIMS analysis. One example is comparing the surface differences of DBTs before and after a toluene solvent treatment. Toluene hardly dissolves DBTs, and it evaporates within few minutes. The self-assembly of DBT nanodomains does not likely happen under this condition, and the ordered arrangement of DBTs may be damaged by the movement of organic solvents on the surface. Figure 3.6 shows two SIMS spectra of BDT II films before and after a toluene solution and air purging treatment. It shows no chemical changes after toluene solvent treatment. However, Both SI yields of F^- and CF_3^- reduce from 30.1% to 25.1% and from 19.1% to 17.4%, respectively. The surface coverage of fluorocarbons meanwhile decreases from ~95% to ~82%. It suggests that the well-organized surface arrangement, at least in some DBT nanodomains, has been changed slightly after toluene solvent treatment. We can still claim the DBT keeps a rigid brush structure and the overall film structure stays because the Q values between SIs from fluorocarbons and *N*-phenylmaleimide groups [e.g., Q(F^-, CNO^-), Q(F^-, $phNCO^-$), Q(CF_3^-, CNO^-), and Q(CF_3^-, $phNCO^-$)] do not change after toluene treatment.

Table 3.2 SI yields of fluorocarbon and N-phenylmaleimide related ions for non-annealed, acetone-assisted-annealed, and thermally annealed samples of DBT III.

Detected SIs	*m/z*	Non-annealed	Solvent-assist Annealed	Thermal Annealed
F^-	19	3.8%	10%	2.7%
$C_8F_4H_3O^-$	191	5.2%	10%	7.0%
CNO^-	42	6.4%	5.5%	13%
$PhNCO^-$	119	3.4%	3.0%	8.8%

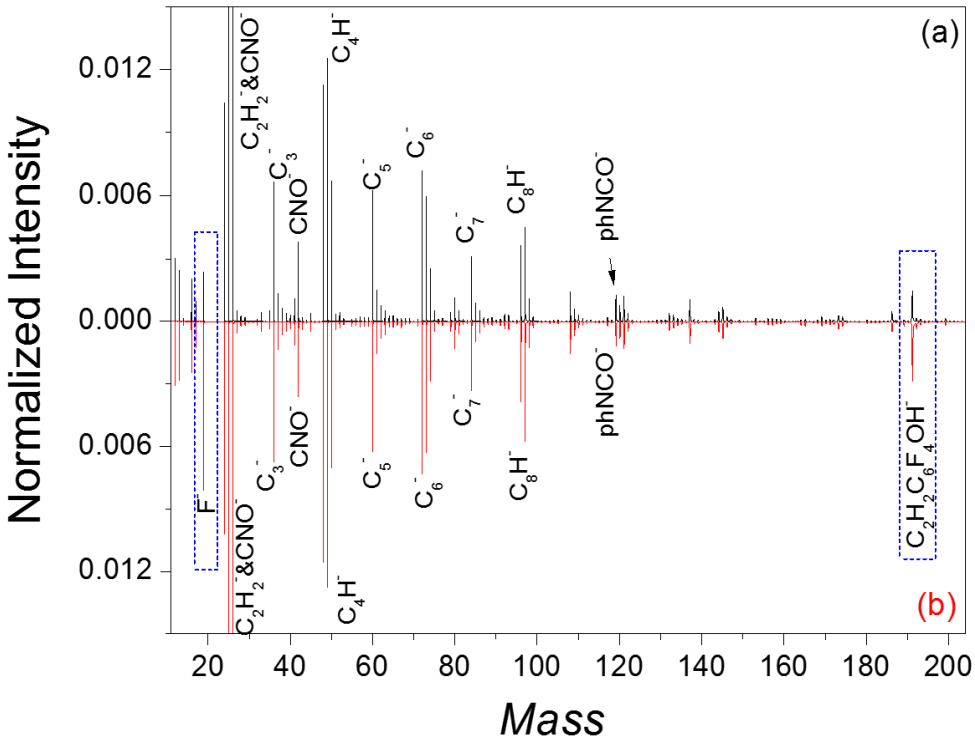

Figure 3.7 Comparison of negative ion mass spectra of DBT II (a) before and (b) after acetone-assisted solvent annealing.

In another case, conservative annealing treatments would prompt fluorocarbons toward the surface and reinforce the vertically aligned pattern [125]. The order of surface DBT arrangement could be therefore improved. DBT III films are used here as examples to compare different annealing treatments. The comparison of the SI spectra of the non-annealed and acetone-assisted-annealed DBT III films is shown in Figure 3-5. In DBT

III, the fluorocarbon ions F^- and $C_8F_4H_3O^-$ are used to assess annealing results. The mass spectra are identical regarding the species of the observed ion peaks, indicating that acetone-assisted annealing did not change the chemical component and structure of the DBT III film. Table 3.2 shows the SI yields of F^-, $C_8F_4H_3O^-$, CNO^-, and $phNCO^-$ from non-annealed, acetone-assisted annealed, and thermally annealed samples. They are typical SIs from either fluorocarbon or *N*-phenylmaleimide. The SI yields of F^- and $C_8F_4H_3O^-$ increase after the acetone-assisted annealing compared with those of the non-annealed film samples. By contrast, little change is observed between the SI yields of CNO^- and $phNCO^-$ after solvent annealing, indicating that acetone-assisted annealing facilitates the surface segregation of fluorocarbon within films. However, changes in the SI yields after a thermal annealing seem to be the opposite way. SI yields of CNO^- and $phNCO^-$ changed notably, but the SI yields of F^- and $C_8F_4H_3O^-$ remain unchanged or even decrease after the thermal treatment. These results indicate that the *N*-phenylmaleimide groups, instead of fluorocarbon groups, may migrate toward the surface after thermal annealing. Thus, the thermal annealing treatment, different from the solvent-assisted annealing, may damage the "fluorine-up" structure of polymers.

The surface coverage of fluorocarbons in DBT III calculated from Equation 2.9 using F^- and $C_8F_4H_3O^-$, also increased from ~79% in the non-annealed sample to ~94% in the acetone-assisted-annealed sample, which indicates an improved surface coverage. In contrast, the fluorocarbon coverage did not increase after thermal annealing, showing ~74%.

Conclusions

The event-by-event bombardment detection mode probes nano-volumes, thus enabling to identify co-located molecules. Nature and relative intensities of the ejecta are related to the composition and spatial arrangement of the analytes. Some boundaries to the spatial resolution of this SIMS method are set by the volume of the SI emission, which is ~10nm^3. This study shows that segregation within this volume may be detected if they occur depth-wise. Experiments with more compact molecules architectures are needed to determine their size limits of nanodomains that can be detected.

CHAPTER IV

CHARACTERIZATION OF RAW AND MODIFIED PLANT SURFACES*

Introduction

The study of preventing bacterial adhesion is a critical need for food hygiene, treatment, and processing for many years [126-129]. Antifouling coatings are one of the potential approaches used in the protection of biomaterials and engineering surfaces against bacteria [130, 131]. However, due to the physical and chemical difficulties, a practical way to use antifouling coatings on the produce surfaces is questionable. The understanding of raw and modified plant surfaces at the molecular level is necessary and will benefit the follow-up research of using thin film polymers as antifouling materials.

In this chapter, we used Au cluster SIMS with the event-by-event bombardment-detection mode for the analysis of plant surfaces since cluster SIMS has advantages to the enhanced emission of molecular ion signals and reduced molecular fragmentation. As discussed before, the event-by-event bombardment-detection mode enables the characterization of co-localized molecular species within nanodomains. This novel SIMS was also applied to study the degree of coated polymer films and could relate it to the level of the bacterial attachment on the tomato fruit.

---

* Parts of this chapter were reprinted with permission from *International Journal of Food Microbiology*, Volume 185, pages 73-81, Ming Zhang, Fan Yang, SasiKiran Pasupuleti, Jun Kyun Oh, Nandita Kohli, I Lee, Keila Perez, Stanislav V Verkhoturov, Emile A Schweikert, Arul Jayaraman, Luis Cisneros-Zevallos, Mustafa Akbulut "Preventing Adhesion of Escherichia coli O157: H7 and Salmonella Typhimurium LT2 on Tomato Surfaces via Ultrathin Polyethylene glycol Film." Copyright [2014] Elsevier, Ltd.

In this chapter, we used Au cluster SIMS with the event-by-event bombardment-detection mode for the analysis of plant surfaces since cluster SIMS has advantages to the enhanced emission of molecular ion signals and reduced molecular fragmentation. As discussed before, the event-by-event bombardment-detection mode enables the characterization of co-localized molecular species within nanodomains. This novel SIMS was also applied to study the degree of coated polymer films and could relate it to the level of the bacterial attachment on the tomato fruit.

Experimental section

Preparation of raw plant surfaces

Oleander leaves (Nerium oleander, family: Apocynaceae), and cultivated wheat leaves (Triticum aestivum, family: Poaceae) were collected from living plants. Fresh tomato fruit was purchased from a local grocery store. After extensively rinsing with deionized water, the produce was then dried using Kim wipes tissues (Kimberly-Clark Professional, Roswell, GA).The pulp part of tomato was removed to obtain a thin transparent skin, and then they were cut into 1×1 cm^2 pieces. The produce pieces immobilized on the top of cleaned silicon (111) wafers using a double-sided adhesive carbon tape. All samples were then dried overnight under a fume hood before the further treatment.

Oxygen plasma etching and polymer coating on plant surfaces

Dried tomato fruit skins were treated with non-thermal oxygen plasma. March CS-1701 Reactive Ion Etching system (March Plasma Systems, Inc., Concord, CA) from few seconds to 10 minutes. The system runs at an RF frequency of 13.56 MHz with the power output of 150 W, with the O_2 flow of 10 sccm. After 100s plasma treatment, tomato fruit skin samples were immersed into 10% PEG (Mw = 2000, Alfa Aesar), or 10% PVP (Mw =8000, Alfa Aesar) aqueous solutions for 15 min, respectively. Then, they were rinsed with DI water and dried with the N_2 gas purge.

Scanning electron microscopy (SEM)

JEOL JSM-7500F high-resolution field emission SEM (JEOL USA Inc., Peabody, MA) was used to determine the surface morphology of neat tomato skin surfaces and to characterize the physical changes on the produce surface due to the oxygen plasma treatment.

Au cluster-SIMS with the event-by-event bombardment-detection mode

All plant samples were examined with 520 keV Au_{400}^{4+} SIMS instruments operated in the event by event bombardment-detection mode. The instrumentation detail is discussed in Chapter II. Total mass spectra were collected by a summation of several million events. The data acquired in this event-by-event detection mode were processed with custom developed software (SAMPI) [100]. Co-emission mass spectra including an SI of interest were extracted from the records of the individual impacts [81, 119]. This

procedure identifies co-localized molecules within 10-20 nm nanodomains on the surface.

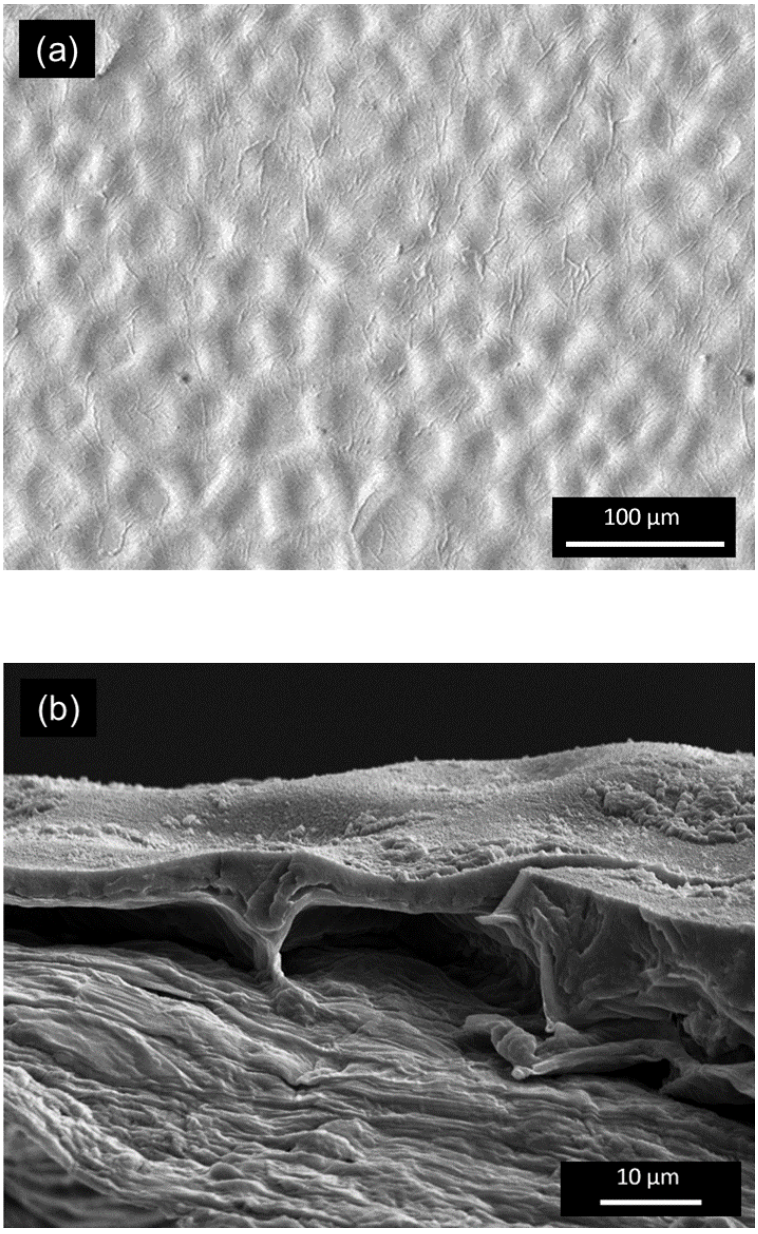

Figure 4.1 SEM images of (a) the top view and (b) the cross-section view of the tomato fruit skin.

Results and discussion

SEM results of the bare tomato fruit and the oleander leaf

Epicuticular waxes are principal components on the top of the tomato fruit cuticle layers, which contain different chemical components from long-chain hydrocarbons to fatty acids [132-135]. Figure 4.1 shows the SEM micrographs of the top view and the cross-section view of the tomato fruit surface.

Tomato fruit surfaces displayed ridge-and-valley-like structures. A smooth wax layer adhered to the outside fabric of the tomato surface area, e.g., trichomes, upper cuticles in Figure 4.1a. The thickness of the wax layer varies from case to case, and it depends on the environment and the plant itself [134-136]. In this case, the estimated thickness of the wax layer was ~3-8 μm in Figure 4.1b. These results show a layer of natural waxes covering the overall surface of the tomato skin.

Figure 4.2 shows the SEM result of the oleander leaf. Similar to the tomato skin, the surface of oleander leaf is covered by the thick layer of natural waxes at the micron level.

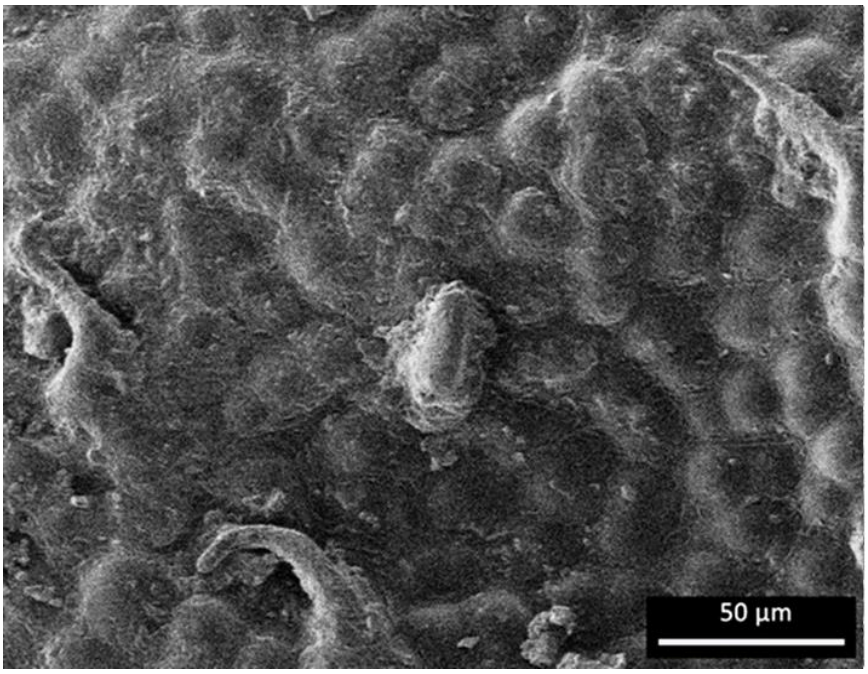

Figure 4.2 SEM image of the top view of the oleander leaf.

Secondary ion emissions of the raw tomato fruit

A plant cuticle is a protective layer of the epidermis of leaves, fruit, and other plant organs without periderm. It contains a broad range of chemicals from lipid and carbon-based polymers impregnated with wax. Those waxes are a complex mixture of long-chain hydrocarbons, aldehydes, alcohols, acids, and esters as well as of sterols and triterpenes [134, 135, 137-141]. Here we use a tomato skin as an example to demonstrate how to apply SIMS to characterize surface components of plants. The negative ions SIMS spectrum of the raw tomato skin without any chemical treatments is shown in Figure 4.3. Fragmental ions such as C_n^-, C_nH^-, e.g., which are ions at mass 13 (CH^-), 25 (C_2H^-), 36 (C_3^-), 49 (C_4H^-), 60 (C_5^-), 73 (C_6H^-), 84 (C_7^-), 97 (C_8H^-), 108 (C_9^-), 121 ($C_{10}H^-$

), 133 ($C_{11}H^-$), 145 ($C_{12}H^-$), and 157 ($C_{13}H^-$) in the low mass region (*m/z*<100 amu) indicated numbers of hydrocarbons in the wax layer and other common ions are also shown. The SI at mass 42 (CNO^-) corresponds to nitrogen-containing compounds. The SIs at mass 63 (PO_2^-) and 79 (PO_3^-) are from phosphate-containing components such as lipids. In the higher mass range, the SI at mass 197 (Au^-), 223 ($AuC_2H_2^-$), and 239 ($AuC_2H_2O^-$) correspond to negative ions of Au and Au adducts [120, 121]. Also, the SIs at mass 113 ($C_8H_{17}^-$), 169 ($C_{12}H_{25}^-$), 183 ($C_{13}H_{27}^-$), and 211 ($C_{15}H_{31}^-$) correspond to molecular ions of hydrocarbons. Hydrocarbons usually prefer to form positive fragmentation ions rather than negative ones, so intensities of most SIs of hydrocarbons are much lower than those of carbon cluster ions in the negative ion mass spectrum. The SIs at mass 137 ($C_{10}H_{17}^-$), and 149 ($C_{11}H_{17}^-$) correspond to terpenoids, carbohydrates or their derivatives [132, 134, 135, 138]. The SI at mass 271($C_{15}H_{11}O_5^-$) corresponds to the molecular ion of naringenin-chalcone [135, 138]. Long-chain fatty acids, as one of the main components of epicuticular waxes, often form groups of carboxylate ions in the mass spectrum. From tomato skins, the SIs at mass 283 [$CH_3(CH_2)_{16}COO^-$], 297 [$CH_3(CH_2)_{17}COO^-$], 311 [$CH_3(CH_2)_{18}COO^-$], 325 [$CH_3(CH_2)_{19}COO^-$], and 339 [$CH_3(CH_2)_{20}COO^-$] correspond to fatty acids or their derivatives. No contaminants or other groups of chemicals are found in mass spectra. In sum, most abundant SIs from the overall mass spectrum are carbon clusters and carboxylates, which indicates that principal components of the epicuticular wax are hydrocarbons, fatty acids, and their derivatives. SIMS detection volume and SI result indicated that epicuticular waxes were

main components on the outermost layer of peeled tomatoes. Similar results were also discussed in other SIMS studies of the plant surfaces[142, 143].

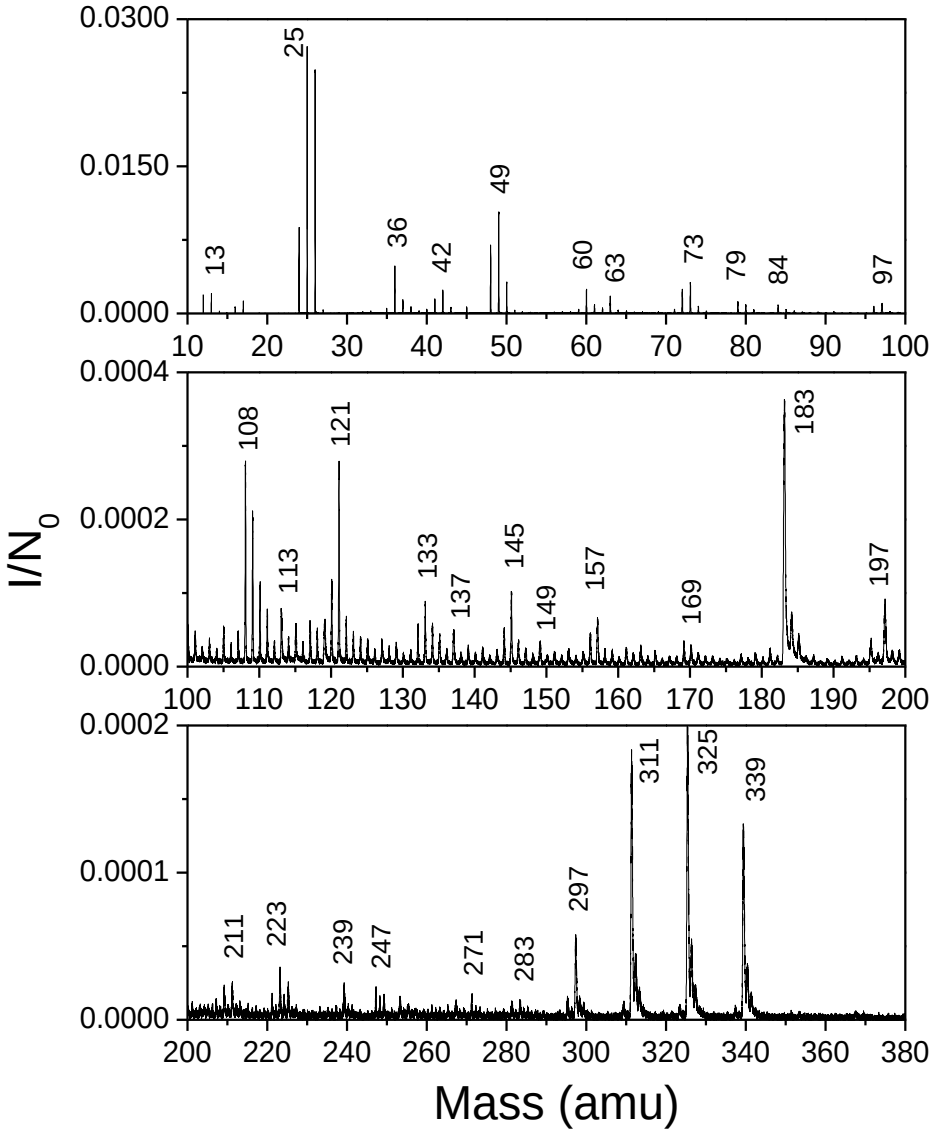

Figure 4.3 520 keV Au_{400}^{4+} negative ion mass spectra of the raw tomato fruit skin.

Secondary ion emission from non-treated plant surfaces

Long-chain fatty acids, as one of the common components of epicuticular waxes, form groups of carboxylic ions in the negative ion mass spectrum. Figure 4.4 compares molecular ions of fatty acids in oleander leaves, tomato fruit skins, and wheat leaves from mass 290 to 530 amu. They show different groups of carboxylic ions for each type of samples. In the mass spectrum of oleander leaves, the peaks at mass 297 [$CH_3(CH_2)_{17}COO^-$], 311 [$CH_3(CH_2)_{18}COO^-$], 325 [$CH_3(CH_2)_{19}COO^-$], 339 [$CH_3(CH_2)_{20}COO^-$], 395 [$CH_3(CH_2)_{24}COO^-$], 409 [$CH_3(CH_2)_{25}COO^-$], 423 [$CH_3(CH_2)_{26}COO^-$], 437 [$CH_3(CH_2)_{27}COO^-$], 449 ($C_{29}H_{57}COO^-$ or $C_{32}H_{65}^-$), 451 [$CH_3(CH_2)_{28}COO^-$], 465 [$CH_3(CH_2)_{29}COO^-$], 479 [$CH_3(CH_2)_{30}COO^-$], and 493 [$CH_3(CH_2)_{31}COO^-$] correspond to two groups of fatty acids or their derivatives. The ion peaks at mass 297 [$CH_3(CH_2)_{17}COO^-$], 311 [$CH_3(CH_2)_{18}COO^-$], 325 [$CH_3(CH_2)_{19}COO^-$], and 339 [$CH_3(CH_2)_{20}COO^-$] show in the mass spectrum of tomato fruit skins, and the peaks at 297 [$CH_3(CH_2)_{17}COO^-$], 395 [$CH_3(CH_2)_{24}COO^-$], 423 [$CH_3(CH_2)_{26}COO^-$], 463 ($C_{30}H_{59}COO^-$ or $C_{33}H_{67}^-$) , and 479 [$CH_3(CH_2)_{30}COO^-$] show in the mass spectrum of wheat leaves, respectively. The mass spectra result showing above reveal that different plant develops different groups of fatty acids on their surface areas. The chemical formation of epicuticular waxes depends on the nature of plants and their outside environments.

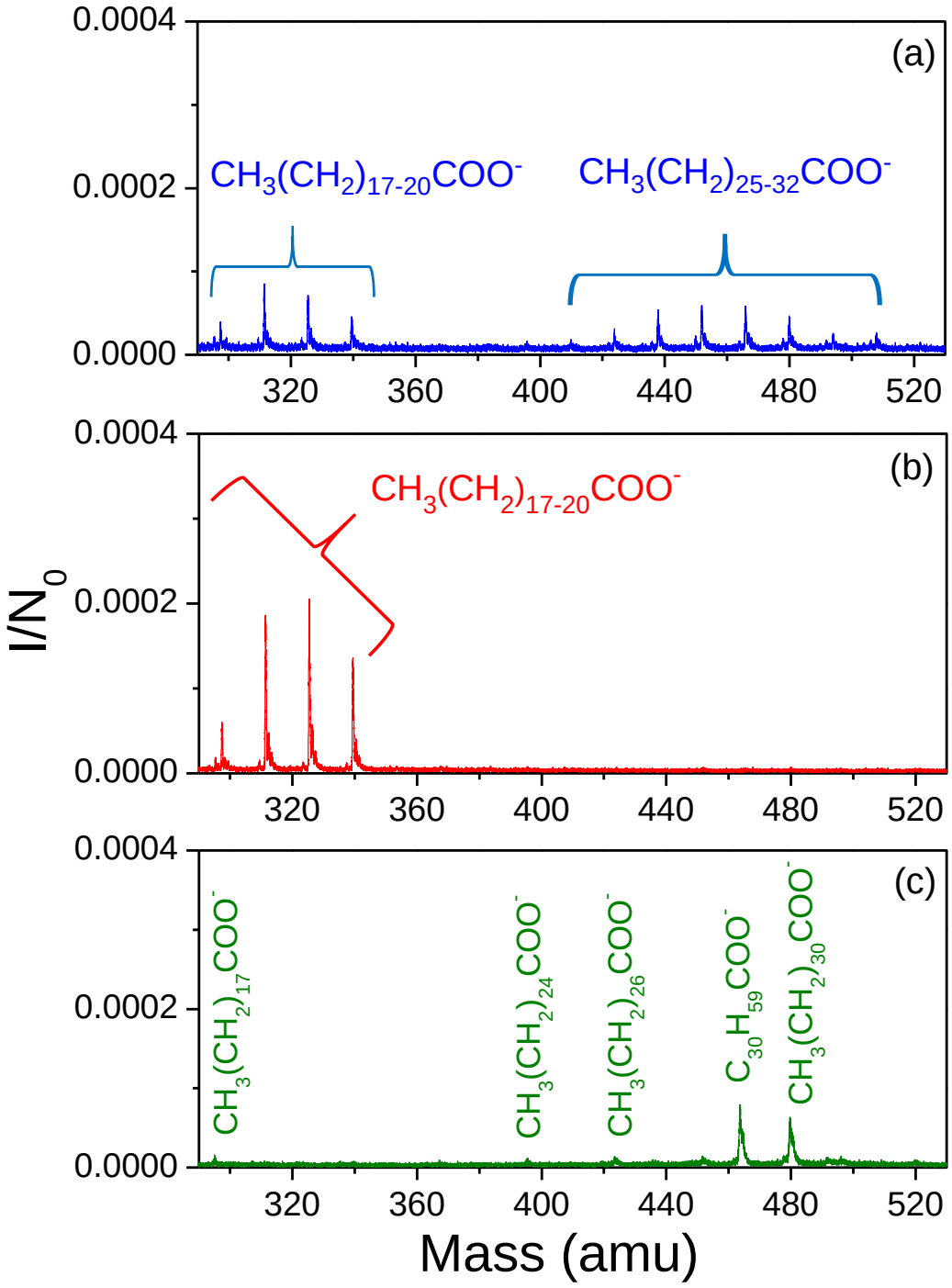

Figure 4.4 520 keV Au_{400}^{4+} negative ion mass spectra of (a) oleander leaves, (b) tomato fruit skins, (c) wheat leaves.

Table 4.1 Correlation coefficients (Q) of selective molecular ions of hydrocarbons or fatty acids in the oleander leaf.

Q	With C_5^-	With $C_2H_2O^-$ or CNO^-	With $C_8H_{17}^-$	With $CH_3(CH_2)_{18}COO^-$	With $CH_3(CH_2)_{28}COO^-$
$C_{12}H_{25}^-$	1.0	1.1	1.3	0.9	0.8
$C_{14}H_{27}^-$	1.1	1.5	1.4	4.9	0.5
$CH_3(CH_2)_{19}COO^-$	1.2	0.4	1.3	5.9	0.9
$CH_3(CH_2)_{29}COO^-$	1.1	1.0	0.9	0.7	2.2

The coincidence counting method was used to estimate the surface homogeneity of these chemical species in the wax layer [109]. The detailed discussion of this methodology is in Chapter II. Table 4.1 lists correlation coefficients (Q) values of molecular ions of hydrocarbons or fatty acids with different types of SIs from the mass spectrum of oleander leaves. Q values of molecular ion [$C_{12}H_{25}^-$, $C_{14}H_{27}^-$, $CH_3(CH_2)_{19}COO^-$, or $CH_3(CH_2)_{29}COO^-$] with C_5^-, which is one of carbon-based fragmentation ions, are close to the unity. It means molecular ions of hydrocarbons or fatty acids and fragmentation ions are independently emitted from a single emission area because low mass carbon-based fragmentation ions often recombined from molecules containing carbons. Both hydrocarbons and fatty acids could contribute carbons to fragmentation ions, so their Q values are not significantly different. In contrast, Q values of a molecular ion with $C_2H_2O^-$ or CNO^- do not always equal to one. For instance, Q[$C_2H_2O^-$, $CH_3(CH_2)_{19}COO^-$] is 0.4, while Q($C_2H_2O^-$, $C_{14}H_{27}^-$) is 1.5. Nearly unity Q

values were observed between $C_2H_2O^-$ and $C_{12}H_{25}^-$, and $C_2H_2O^-$ and $CH_3(CH_2)_{29}COO^-$. Q values between long-chain hydrocarbon ions and fatty acid ions are also different. They show that $C_8H_{17}^-$, $C_{12}H_{25}^-$, $C_{14}H_{27}^-$, and $CH_3(CH_2)_{19}COO^-$ are correlated. $C_{14}H_{27}^-$, $CH_3(CH_2)_{18}COO^-$, and $CH_3(CH_2)_{19}COO^-$ are co-localized while $CH_3(CH_2)_{28}COO^-$ and $CH_3(CH_2)_{29}COO^-$ are related. The coincidental analysis of SIs from the oleander leaf shows its surface components are not homogeneous. Instead, SIs of long-chain hydrocarbons and fatty acids are identified from different nanoscopic domains or chemicals.

Oxygen plasma etching on tomato surfaces

Figure 4.5 compares the SEM results of tomato fruit surfaces after 100s and 600s of nonthermal oxygen plasma etching. Upon an exposure of 100s to oxygen plasma etching (Figure 4.5a), the surface roughness of tomato fruit skins increased, and intercellular spaces were present on the surface. Some of the wax layers were removed. After 600s etching, not only the wax but also the entire cuticle layer was removed. In Figure 4.5b, one can clearly see that the internal materials of the tomato cell are exposed on the surface. The plant cuticle layer in the edge and inter-cell areas are kept since they have a much thicker layer of waxes.

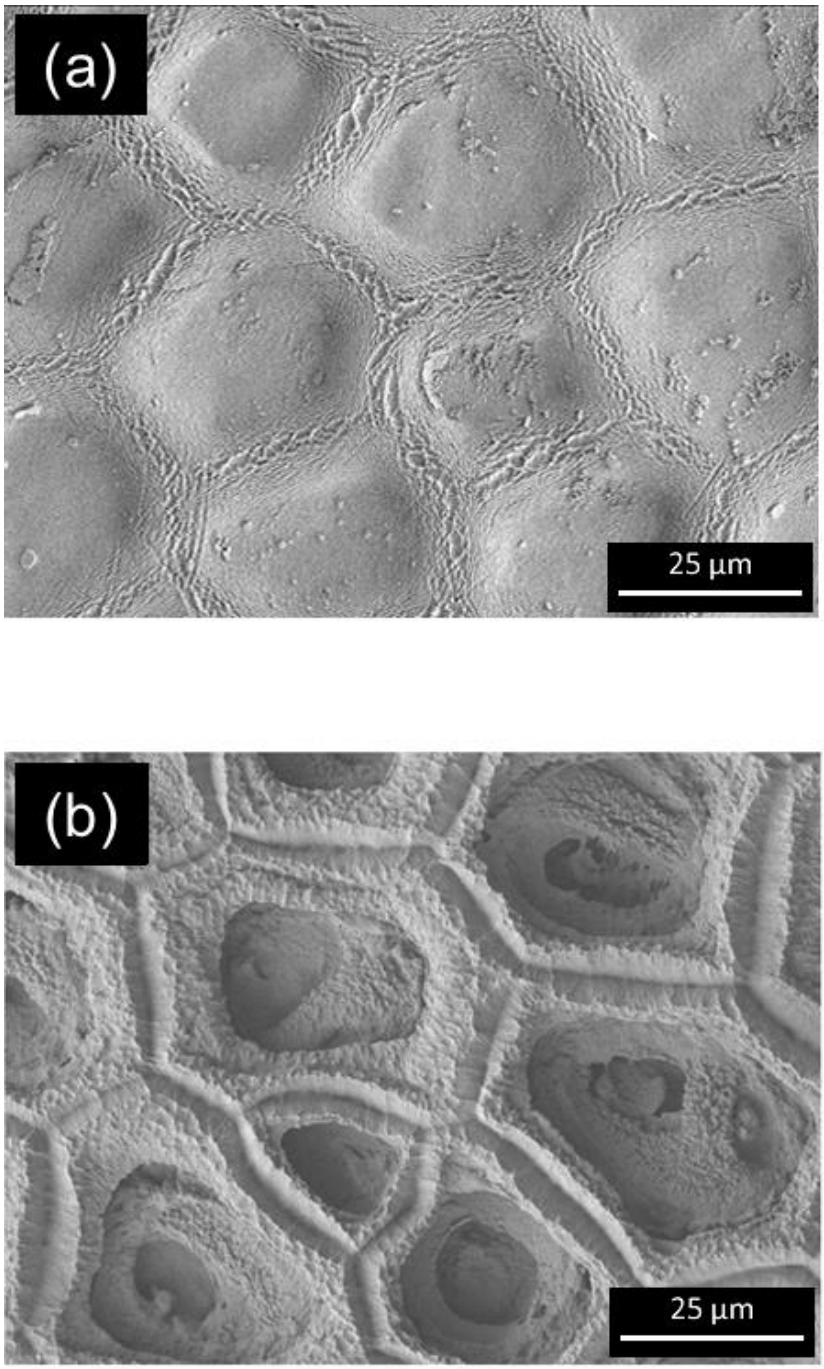

Figure 4.5 SEM images of the tomato fruit surface after (a) 100s and (b) 600s of oxygen plasma etching.

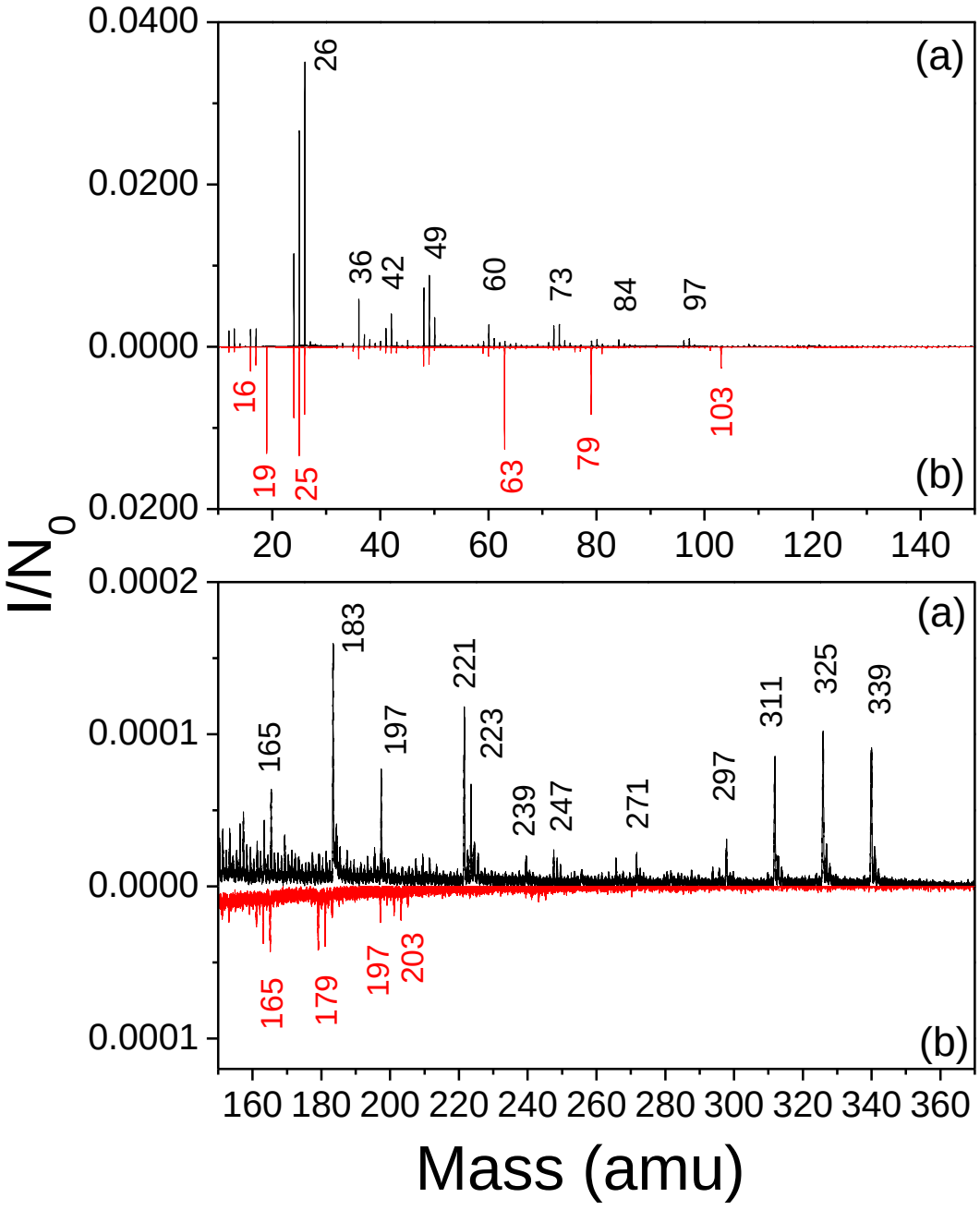

Figure 4.6 Comparison of negative ion mass spectra of tomato surface after (a) 100s and (b) 600s of oxygen plasma etching.

The negative ions SIMS spectra of the tomato surface after oxygen plasma etching are shown in Figure 4.6. The SIs from 100s and 600s etching are completely different since the oxygen plasma etching altered the surface chemical environment. The mass spectrum after 100s etching (Fig. 6a) are similar to the original tomato surface. SIs at mass 13 (CH^-), 26 ($C_2H_2^-$ or CN^-), 36 (C_3^-), 49 (C_4H^-), 60 (C_5^-), 73 (C_6H^-), 84 (C_7^-), and 97 (C_8H^-) are carbon related clusters. $C_{12}H_{21}^-$ and $C_{13}H_{27}^-$ are related to the hydrocarbons. Au^-, $AuC_2H_2^-$ and $AuC_2H_2O^-$ correspond to Au ions and Au adducts. The SIs at mass 297 [$CH_3(CH_2)_{17}COO^-$], 311 [$CH_3(CH_2)_{18}COO^-$], 325 [$CH_3(CH_2)_{19}COO^-$], and 339 [$CH_3(CH_2)_{20}COO^-$] are from fatty acids or their derivatives. However, some hydrocarbons and fatty acids are much smaller than those from the raw tomato fruit skin. The summary of SI yields is shown in Table 4.2. In Figure 4.6b, most SIs from long-chain hydrocarbons and fatty acids, are gone because most of the cuticle layers are removed, and materials inside the cell are exposed on the surface. SI at mass 63 (PO_2^-), 79 (PO_3^-), 103 ($C_5H_{11}O_2^-$), and 179 ($C_{12}H_{19}O^-$) are pronounced, and they might be from chemicals inside the cell. Also, a large amount of F^- probably from the contaminant gas CF_4 during the oxygen plasma process [144].

Table 4.2 SI yields of featured molecular ions of tomato skin

Etching time	$C_{14}H_{27}^-$	$CH_3(CH_2)_{18}COO^-$	$CH_3(CH_2)_{19}COO^-$	$CH_3(CH_2)_{20}COO^-$
0 s	1.7%	1.0%	1.1%	0.7%
100 s	0.5%	0.3%	0.4%	0.4%
600 s	ND	ND	ND	ND

ND=not detectable

PEG or PVP polymer coatings on tomato surface

Figure 4.7 compared negative ion mass spectra of PEG-coated and PVP-coated tomato surface. The mass spectrum of the PEG-coated surface (Figure 4.7a) is clearly correlated to its fragmental molecular ions such as $C_2H_3O^-$, $C_2H_4OH^-$, $CH_2OC_2H_4^-$, $(CH_2CH_2O)_2H^-$, $(CH_2CH_2O)_2OH^-$, and $(CH_2CH_2O)_4CH_3^-$ [145]. $CH_3(CH_2)_{17}COO^-$, $CH_3(CH_2)_{18}COO^-$, $CH_3(CH_2)_{19}COO^-$, and $CH_3(CH_2)_{20}COO^-$ from wax compositions of the tomato skin were hard to observe, which suggests PEG polymer fully covered the tomato. In Figure 4.7b, the PVP related ions are present at Mass 26 (CN^-), 42 (CNO^-), 50 (C_3N^-), 152 [$(C_6H_9NO)C_2OH^-$], 249 [$(C_6H_9NO)_2C_2H_3^-$], and 272 [$(C_6H_9NO)_2C_3N^-$]. We can also observe the tomato skin related ion from the mass spectrum at 183 ($C_{13}H_{27}^-$), 297 [$CH_3(CH_2)_{17}COO^-$], 311 [$CH_3(CH_2)_{18}COO^-$], 325 [$CH_3(CH_2)_{19}COO^-$], and 339 [$CH_3(CH_2)_{20}COO^-$]. This evidence indicates that PVP partially coated on the tomato surface that it still has an open area of components on the top of tomato layers.

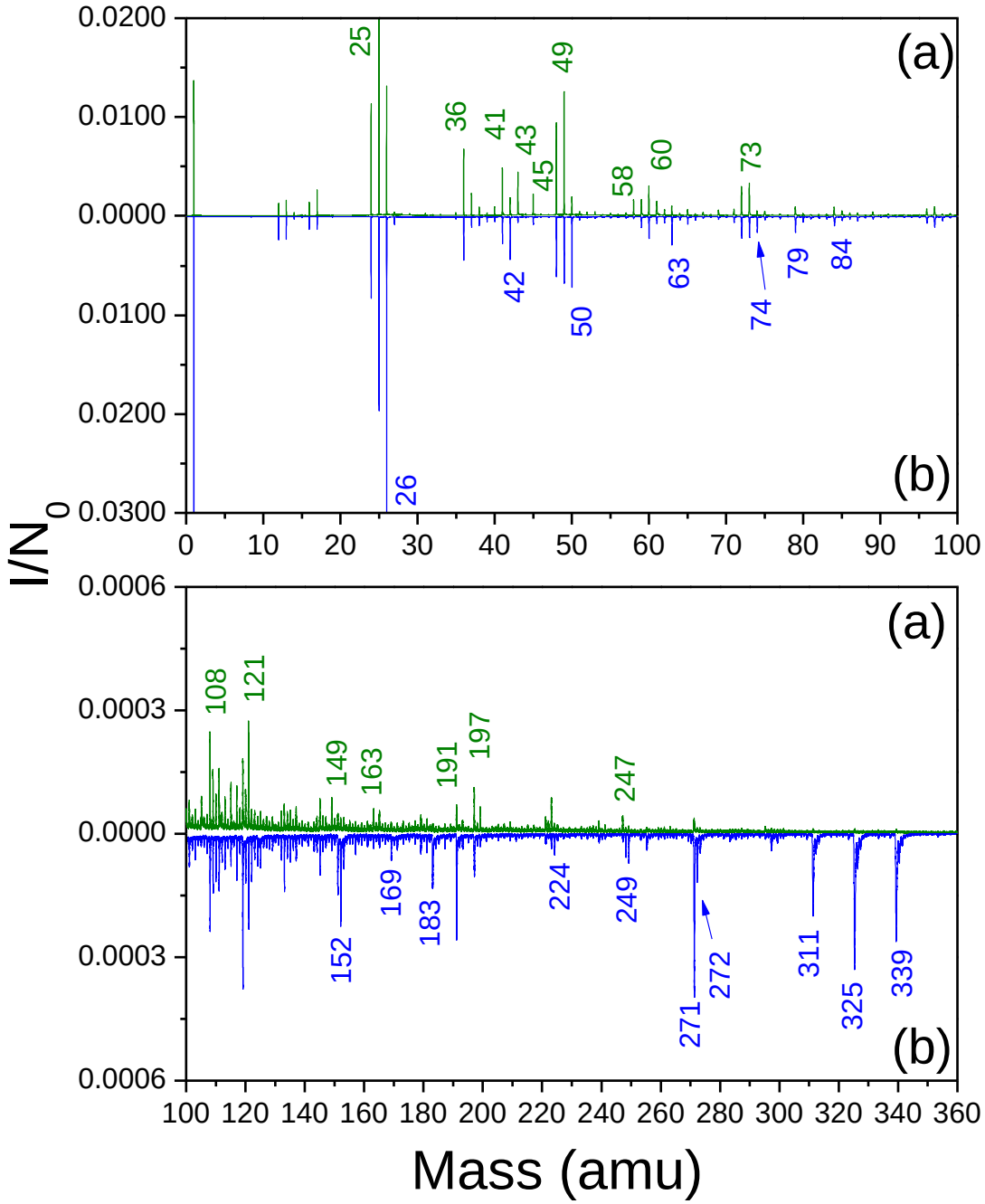

Figure 4.7 Comparison of negative ion mass spectra of (a) the PEG-coated and (b) the PVP coated tomato surface.

The quantitative analysis results explain well for these phenomena. The methodology for a quantitative estimate of the coverage of a given species is discussed in Chapter II [88]. In this case, the ion pair of $CH_2OC_2H_4^-$ and $(CH_2CH_2O)_4CH_3^-$ are considered as fragment ions from PEG and used for calculating the degree of coating of PEG. The ion pairs of CNO^-, $(C_6H_9NO)C_2OH^-$ and $(C_6H_9NO)_2C_3N^-$ are considered as fragmental ions from PVP and used for calculating the degree of coating of PVP. As a result, coated-PEG sample suggested that ~93% of the total surface was covered with PEG polymer. As a comparison, the surface coverage of the PVP film coating is ~79%. Both the SI emission and degree of coating results show that PEG is superior to PVP to form a better polymer film to cover the entire surface area. The follow-up bacterial attachment results in comparison to that on a bare tomato surface were discussed elsewhere [146, 147].

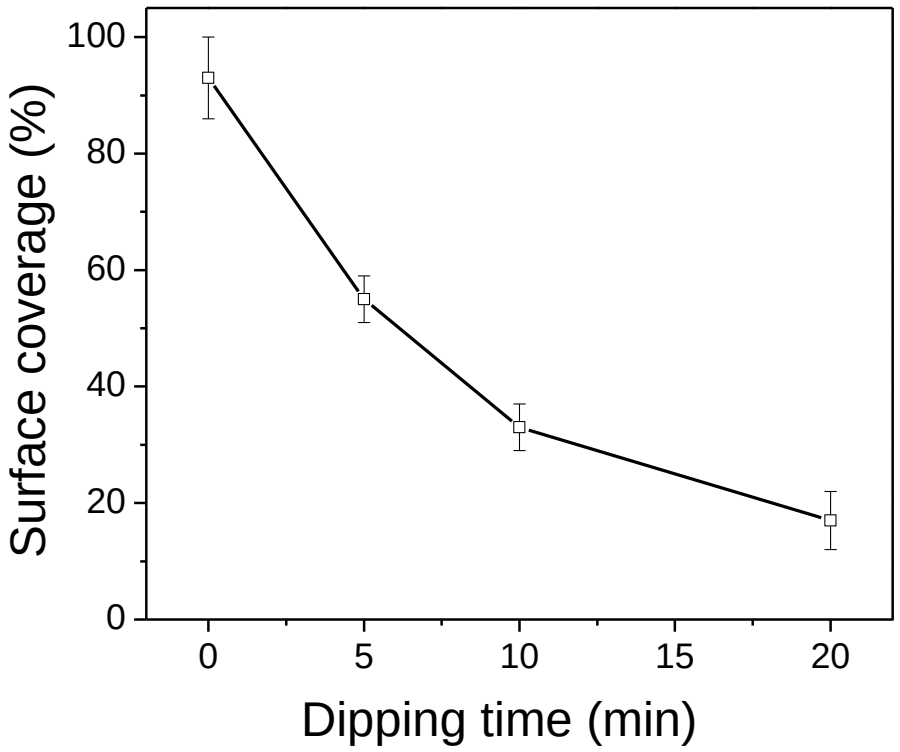

Figure 4.8 The surface PEG film coverage as a function of the water dipping time.

We can use the same method to estimate the remove of the surface PEG coverage from plants. The removal of the water solvable polymer film from the tomato was tested by dipping PEG-coated tomato surfaces in water. The degree of surface PEG coating was calculated from coincidence mass spectra with PEG-related ion peaks [$CH_2OC_2H_4^-$ and $(CH_2CH_2O)_4CH_3^-$] [92, 93, 119]. Figure 4.8 shows surface coverage of PEG as a function of the water rinsing time. The original surface was almost fully covered by PEG film before water treatment. In the first 5 min, nearly 50 % of surface PEG are washed

away. After 20 min dipping, the surface coverage of PEG is less than 17%. The relationship of the removal of PEG from the surface and the dipping time is not linear or single exponential. It is hard to find PEG-related SIs and use them to estimate the degree coating of PEG in a long water dipping time. Also, Figure 4.9 shows the SIMS result of PEG-coated tomato surface after 24 hours water dipping. As we predicted before, there is only tomato surface related ions left and no PEG-related ions present in the mass spectrum.

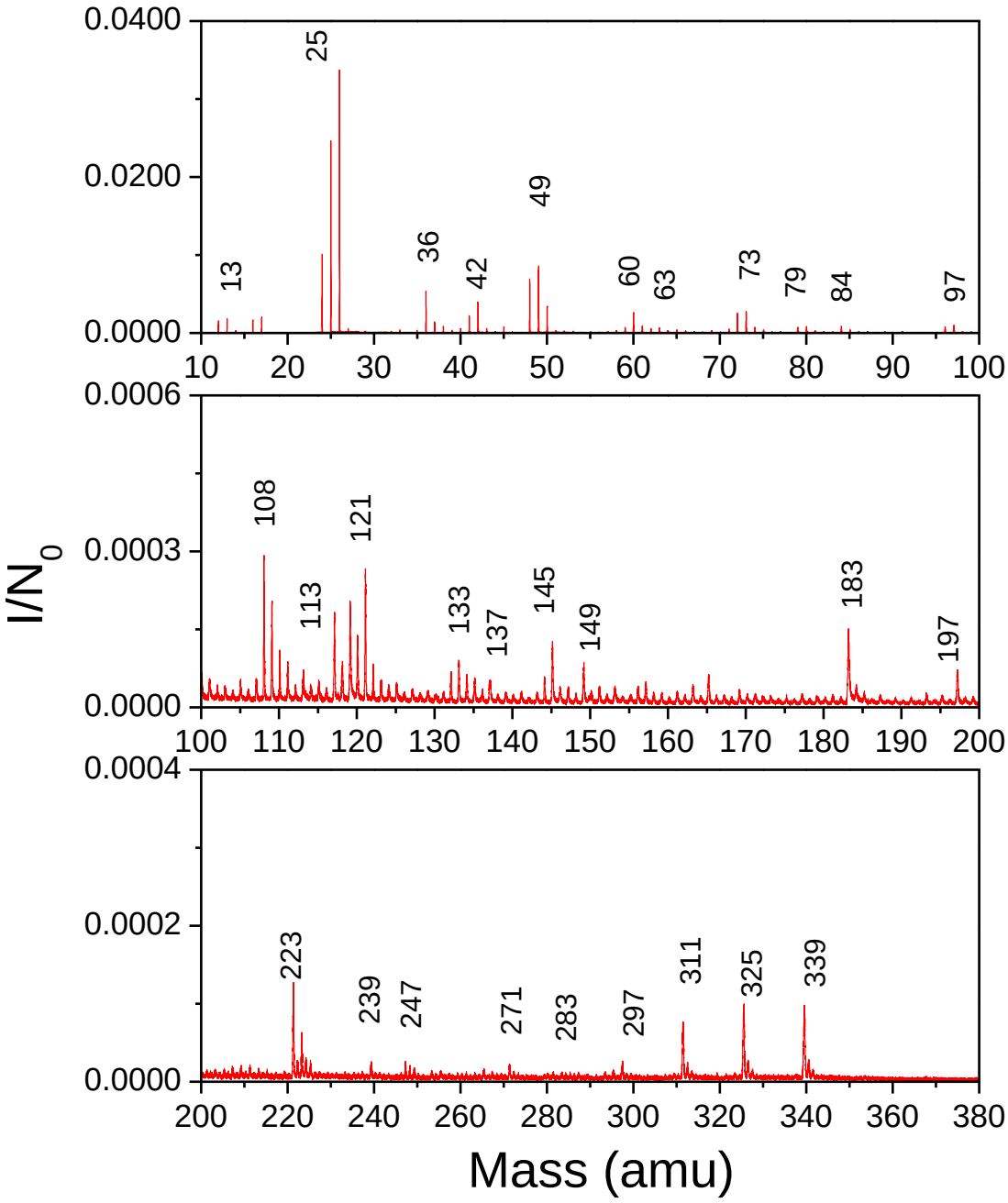

Figure 4.9 520 keV Au_{400}^{4+} negative ion mass spectra of PEG-coated tomato surface after 24 hours water dipping.

Conclusion

This study demonstrates that SIMS is a suitable surface analytical approach to identify different chemical components (e.g. hydrocarbons and fatty acids) on plant surfaces. The degree of PEG coatings on tomato is almost 100%, and this coverage could decrease to 17% only by rinsing in water for 20 min. PEG is a better antifouling potential material than PVP because it can form complete films and is easy to remove. Cluster SIMS with the event-by-event bombardment-detection mode has a promising future for exploring the quality of antifouling coatings at the nanoscale.

CHAPTER V

ADSORPTION IDENTIFICATION AND COVERAGE KINETICS OF SELF-ASSEMBLED MONOLAYER

Introduction

Self-assembled monolayers (SAMs) are widely used in studies of biomimetic systems, chemical resistance, control of wetting and adhesion, molecular recognitions, and nanofabrication [148-153]. The chemical structure of SAMs can be characterized by many surface analytical tools. They often include scanning probe microscopy (atom, electron, neutron, ion, and X-ray) [154-158], diffraction techniques [159-168] and vibrational spectroscopies [169-172]. Among these, the secondary ion mass spectrometry (SIMS) has proven to be valuable for SAMs analysis in chemical identifications, kinetic of absorptions and studies of surface degradation or oxidation [161-163, 173-175]. Although conventional SIMS allows a direct identification, it is still difficult to characterize the surface homogeneity and coverage of ultra-thin SAMs at the nanoscale. However, our novel SIMS technique with massive energetic projectiles, e.g. C_{60} and Au_{400}, is the abundant emission of secondary ions (SIs) [60, 110, 176, 177]. At the level of a single projectile impact, the emitted ejecta originates from molecules co-localized within the depth detection of 5-10 nm [91, 108]. Thus, the identification of co-emission SIs enables the determination of surface SAMs. Also, using the event-by-event bombardment-detection mode, extracting useful impacts from the total impacts can

subset of data that correspond to nanodomains with sufficient statistics for surface homogeneity and coverage characterization [93, 109, 124].

In this study, several alkanethiols with different functional groups are used to self-assembly on Au substrates. The formation of SAMs is identified by C_{60} SIMS with the coincidental methodology with SI emissions, the surface homogeneity, and the change of surface thiol coverage during the adsorption process.

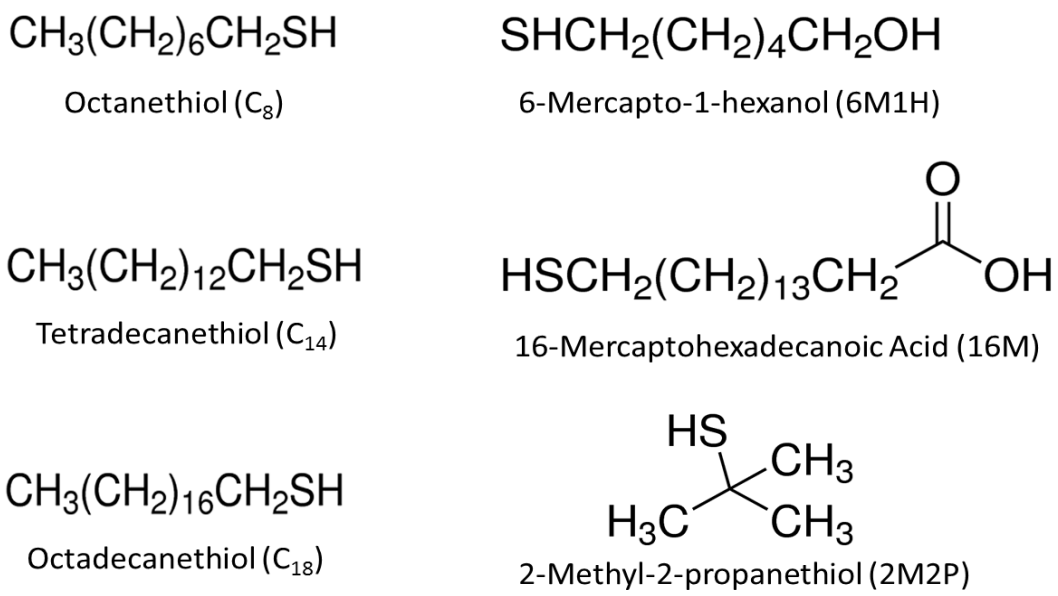

Figure 5.1 The chemical structures of thiols

Experimental section

Materials

All thiols, including 1-octanethiol (C8), 1-tetradecanethiol (C14), 1-octadecanethiol (C18), 6-mercapto-1-hexanol (6M1H), 16-mercaptohexadecanoic acid (16M), and 2-methyl-2-propanethiol (2M2P) were purchased from Sigma-Aldrich (Saint Louis, MO). Their chemical structures are shown in Figure 5.1. Glass microscope slides were purchased from VWR International (Radnor, PA). 100nm thick Au-coated Si wafers were obtained from Silicon Valley Microelectronics (Santa Clara, CA).

Preparation of the Au film on glass slides

Glass slides were cut into ~1 cm^2 pieces and then cleaned by 7X laboratory detergent at 100°C for 30 min. The glass pieces were rinsed with a considerable amount of Millipore water (Barnstead, Dubuque, IA) for several times, and dried by the N_2 purge. The Au (99%) was coated on the cleaned glass surface by a Hummer V sputtering system (Anatech, Union City, CA). The thickness of Au layers was determined by a Gaertner L2W26D ellipsometer (Gaertner Scientific, Skokie, IL) with a 632.8 nm laser beam and 70° incident angle.

Oxygen plasma cleaning Au-coated Si wafers

Au-coated Si wafers were cut into 1×1 cm^2 pieces and then cleaned by ultrasonication in ethanol for 10 min. Wafer pieces were then cleaned by oxygen plasma using the March CS-1701 Reactive Ion Etching system (March Plasma Inc., Concord, CA) for 5 min.

Preparation of thiolated films on different surfaces

The 1mM thiol solutions were prepared with various thiols in ethanol. Fresh prepared Au-coated glass slides or cleaned Au-coated Si pieces were immersed in the thiol solutions from 10 minutes to 36 hours. When a sample was removed from the solution, it was then rinsed with ethanol and purged in a flow of N_2 gas. The surface hydrophobicity of thiol films was also evaluated by static water contact angle measurements. In this method, one drop of Millipore water (resistivity ≥18.2 MΩ·cm at 25 °C, Millipore, MA) was placed onto a fresh prepared thiol-coated film and allowed to equilibrate for the 30s. A digital camera collected images from the cross-section view, and the contact angles were analyzed by ImageJ and contact angle plug-in software. The contact angles are the average of at least three measurements. For SIMS measurement, all thin film samples were quickly transferred into the C_{60} SIMS chamber to minimize their surface oxidations.

C_{60} SIMS with the event-by-event bombardment-detection mode

The C_{60} SIMS measurements were carried out with a customized SIMS instrument, equipped with a C_{60} effusion source capable of producing C_{60}^{2+} projectiles with a total impact energy of 50 keV [178]. The detail of C_{60} SIMS instrument is discussed in Chapter II. Total mass spectra were obtained by the summation of several million events.

Table 5.1 Water contact angles on different thiol-coated surfaces

	Name	"Head group" terminal	Water contact angle
Hydrophobic	Octanethiol (C8)	$-CH_3$	92.64°
	Tetradecanethiol (C14)	$-CH_3$	104.81°
	Octadecanethiol (C18)	$-CH_3$	108.95°
Hydrophilic	6-Mercapto-1-hexanol (6M1H)	-OH	41.50°
	16-Mercaptohexadecanoic Acid (16M)	-COOH	50.00°
	2-Methyl-2-propanethiol (2M2P)	$-CH_3$	73.50°

Results and discussion

Water contact angles of thiols on Au-coated glass substrates

Table 5.1 summarizes static water contact angles of different thiols on Au-coated glass surfaces. The Au-coated glasses were immersed into thiol solution overnight (more than 24 hours) to ensure the maximum adsorption of thiols on the surface. Due to the different "head groups" and structures of thiols, their surface could be considered as hydrophobic or hydrophilic surfaces. If the water contact angle is larger than 90°, the thiol-coated surface will be regarded as the hydrophobic surface. Alternatively, if not, it will be hydrophilic. From these water contact angle results, alkanethiol-coated surfaces including C8, C14 and C18 are hydrophobic. Surfaces of 6M1H, 16M, and 2M2P are hydrophilic. It suggests different thiols can adsorb on the Au-coated glass. However, the water contact angle experiments cannot provide any chemical information, which requires the use of advanced surface analytical techniques.

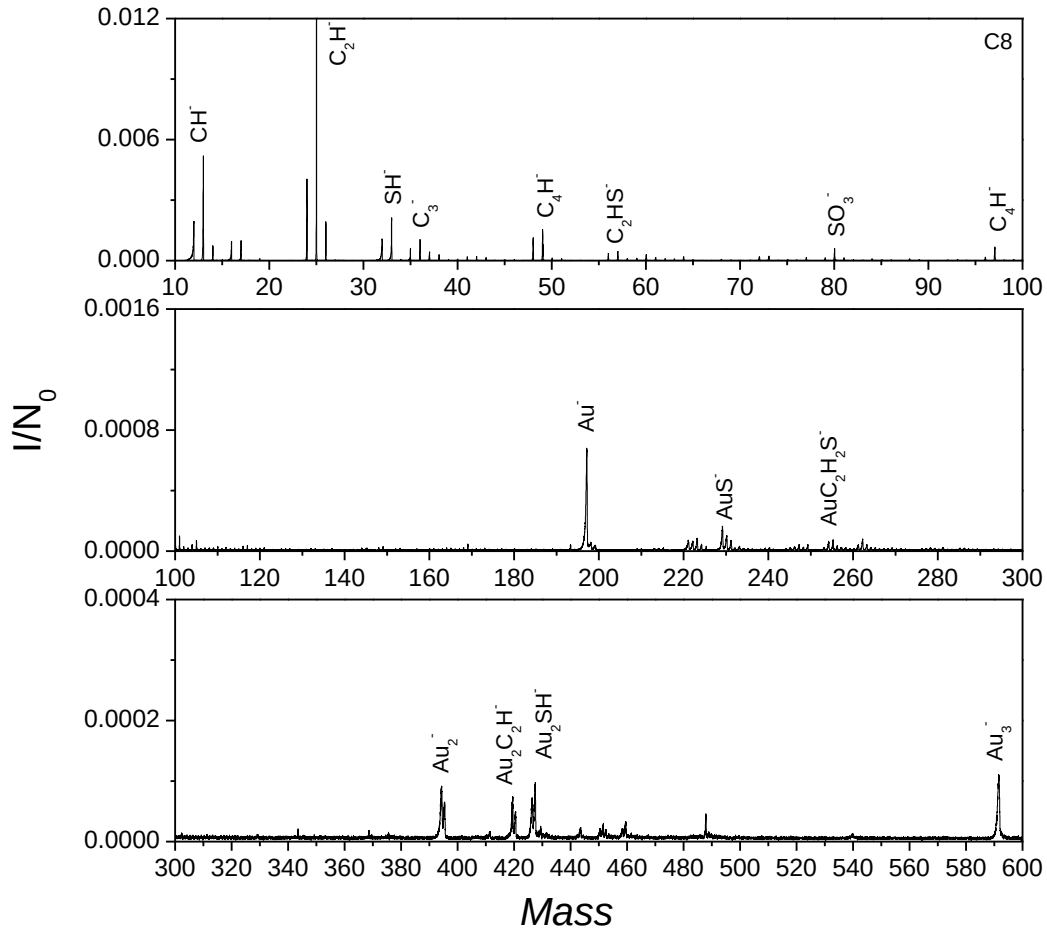

Figure 5.2 The negative ion mass spectrum of C8 adsorbed on the Au-coated glass surface.

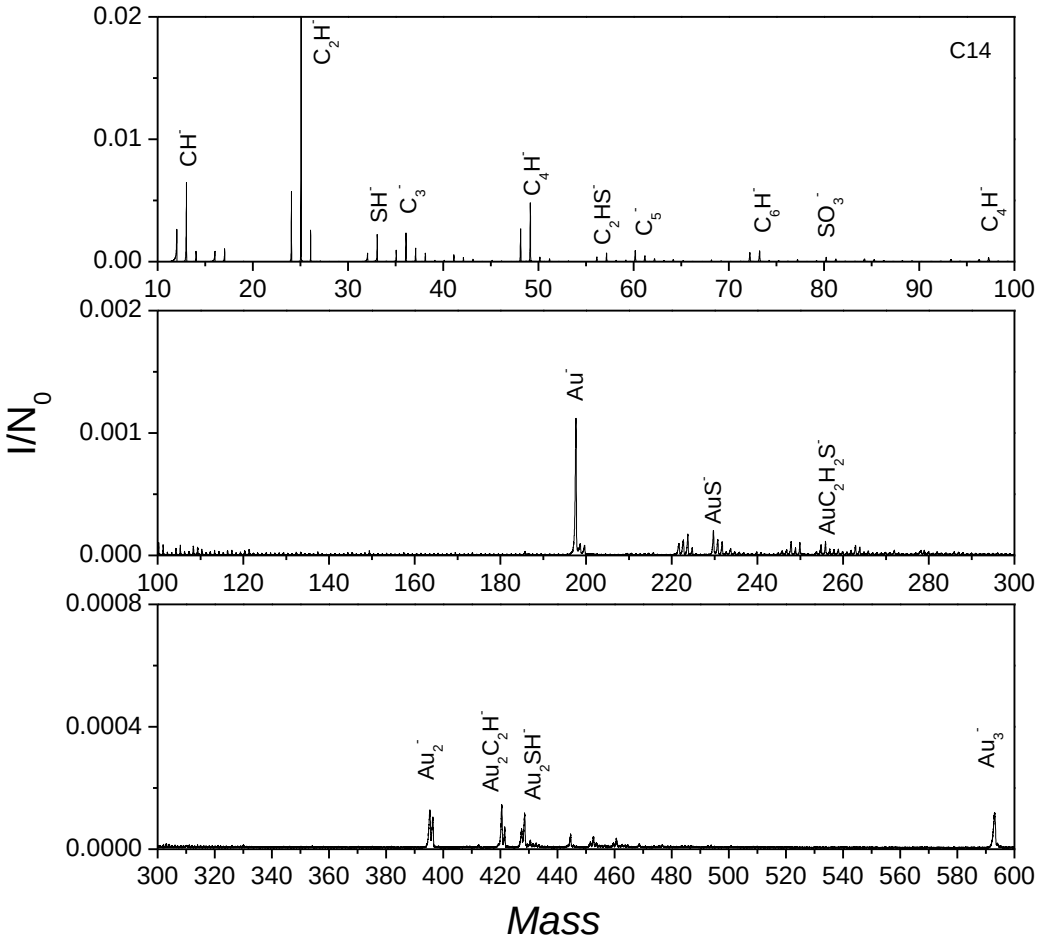

Figure 5.3 The negative ion mass spectrum of C14 adsorbed on the Au-coated glass surface.

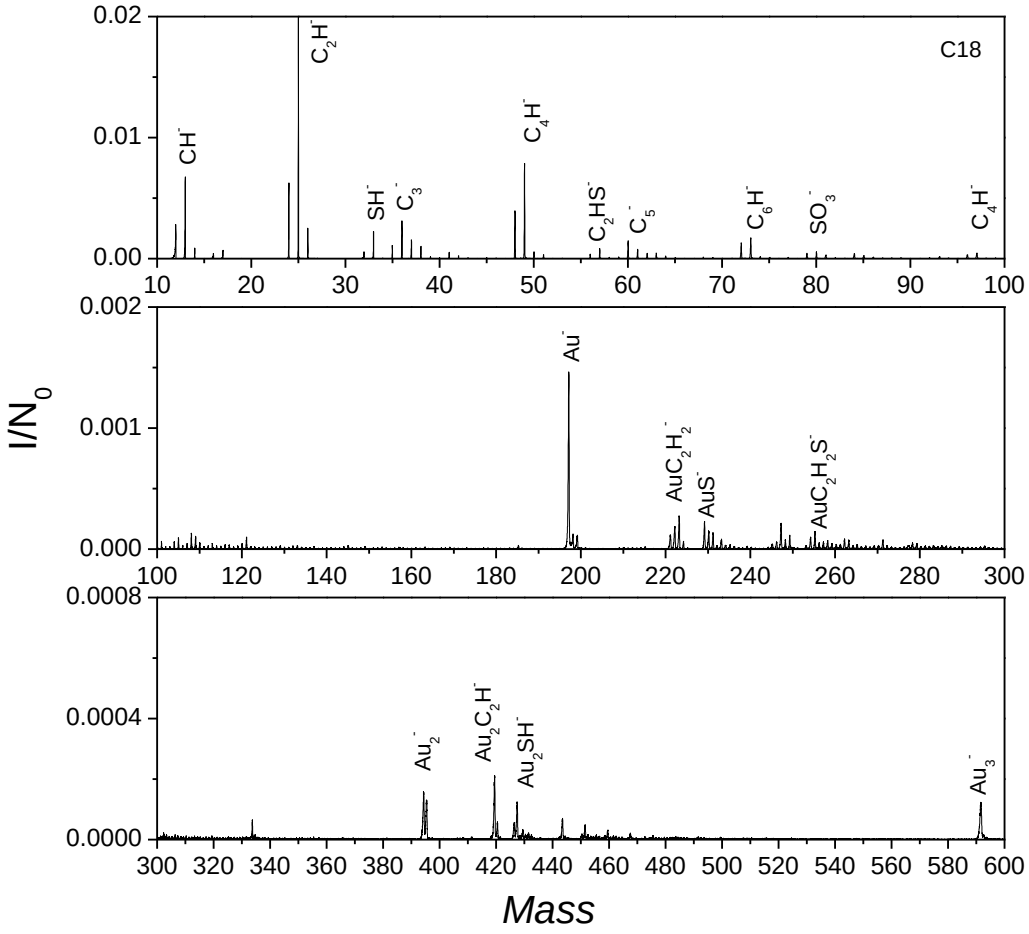

Figure 5.4 The negative ion mass spectrum of C18 adsorbed on the Au-coated glass surface.

SI emissions of thiol adsorbed on the Au-coated glass substrates

Figure 5.2, 5.3, and 5.4 show the negative ion mass spectra of the Au-coated glass slides after 36-hour immersion into 1-octanethiol, 1-tetradecanethiol, and 1-octadecanethiol solutions, respectively. Long time immersion enables alkanethiol

molecules to adsorb on the Au substrate as a monolayer. These mass spectra are similar since C8, C14, and C18 have a similar long chain hydrocarbon head groups. The ion peaks at *m/z* 32 (S^-), 33 (SH^-), and 57 (C_2HS^-) originate exclusively from alkanethiols. Since the thickness of the alkanethiol monolayer (~1-2nm) is thinner than the detection/emission depth of C_{60} SIMS, the secondary ions from the underneath layer, e.g. Au, could be observed in mass spectra as well. Ion peaks at *m/z* 197 (Au^-), 223 ($AuC_2H_2^-$), 229 (AuS^-), 247 ($AuC_4H_2^-$), 255 ($AuC_2H_2S^-$), 394 (Au_2^-), 419 ($Au_2C_2H^-$), and 427 (Au_2HS^-) are Au ions and Au adducts. The presence of gold-sulfur ions is the evidence of the formation of the Au-S bonding at the substrate-thiol interface. Other SIs of Au adducts, e.g. $AuC_4H_2^-$ and $Au_2C_2H^-$, are also generated from the interface of alkanethiols and Au [162]. Little glass related ions are observed from these mass spectra. They only show alkanethiols and Au related SIs in their mass spectra.

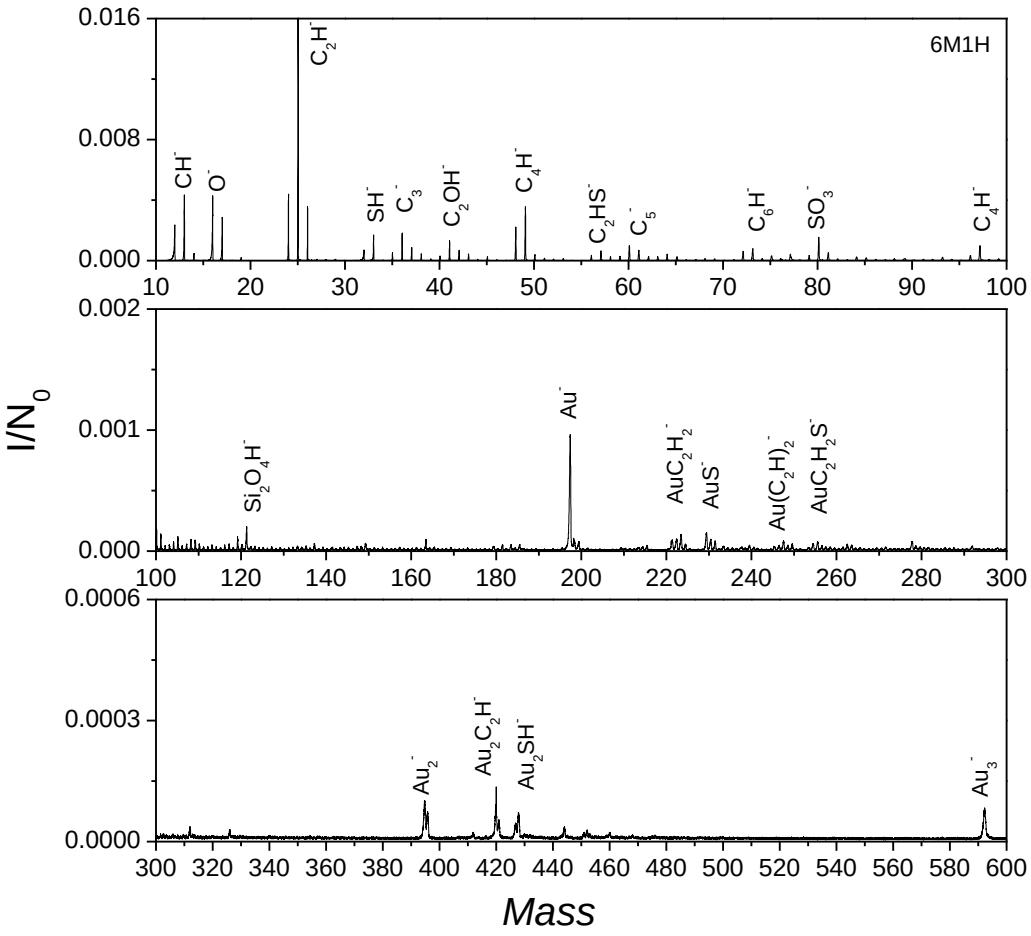

Figure 5.5 The negative ion mass spectrum of 6M1H adsorbed on the Au-coated glass surface.

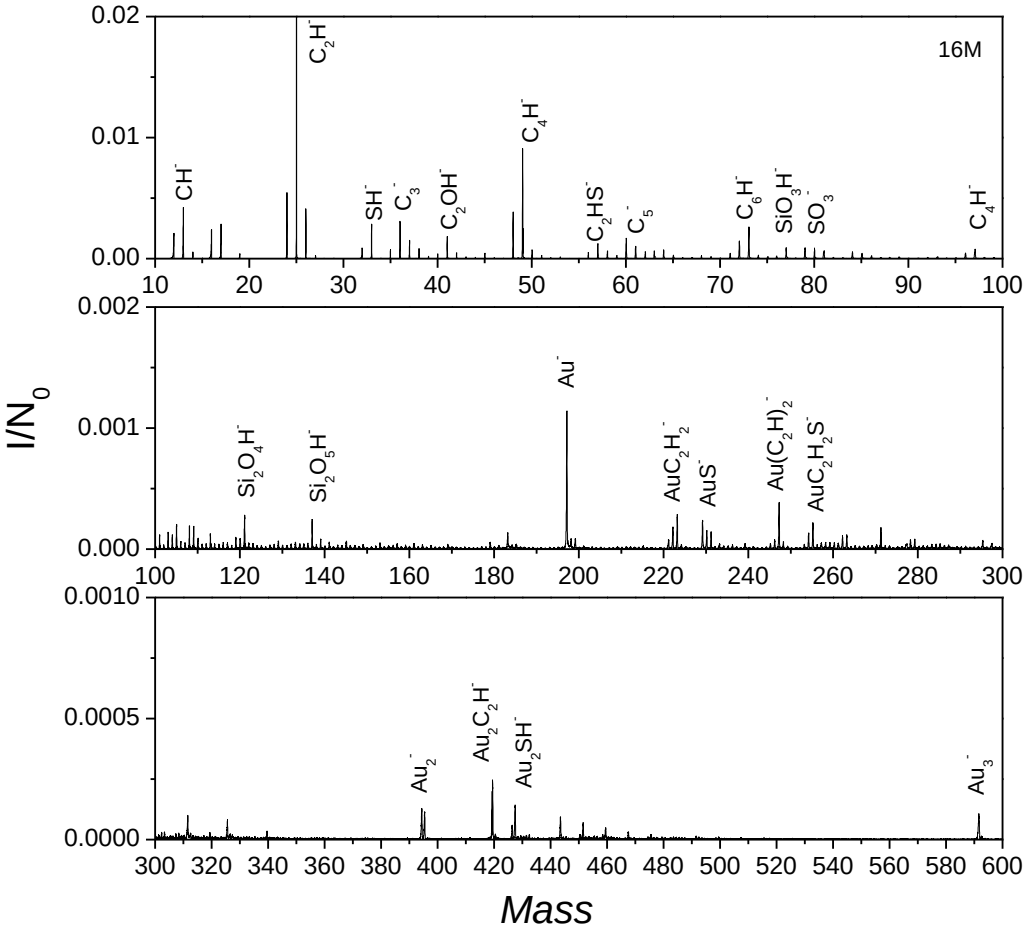

Figure 5.6 The negative ion mass spectrum of 16M adsorbed on the Au-coated glass surface.

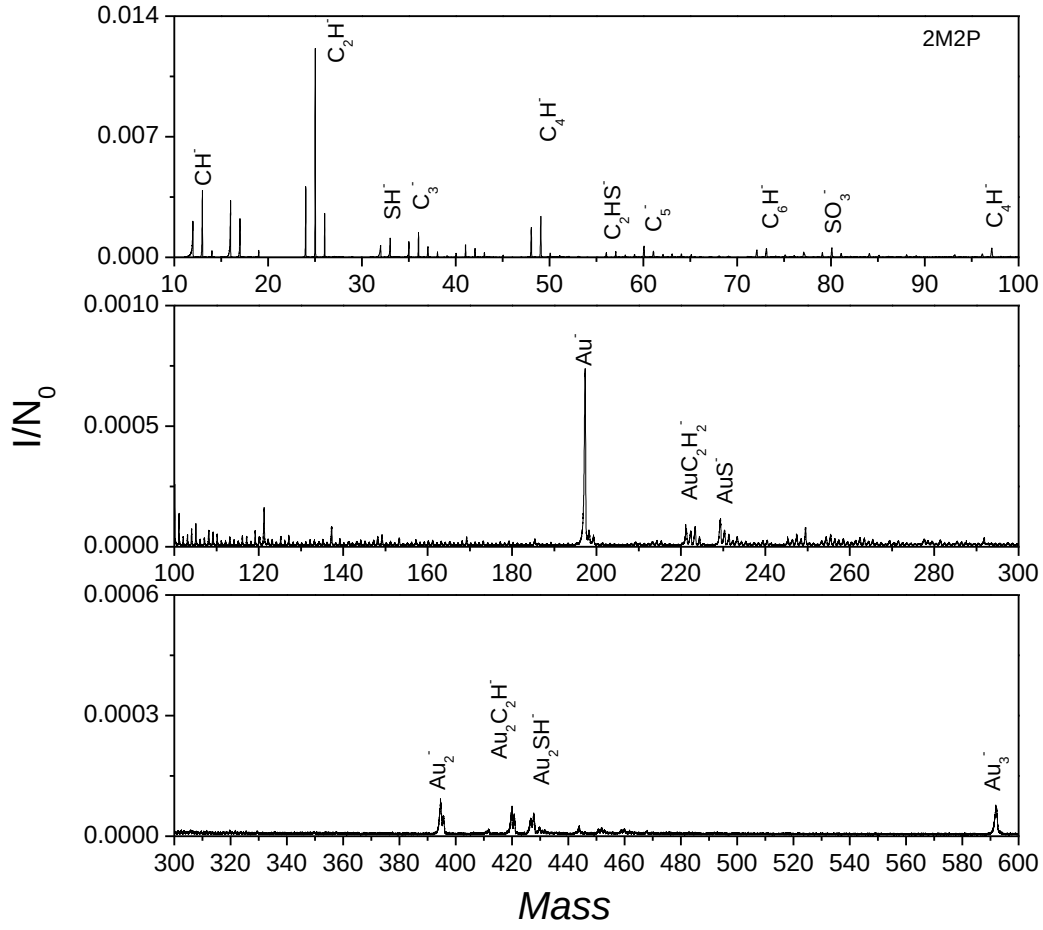

Figure 5.7 The negative ion mass spectrum of 2M2P adsorbed on the Au-coated glass surface.

Figure 5.5, 5.6, and 5.7 show the negative ion mass spectra of the Au-coated glass slides after 36-hour immersion into 6-mercapto-1-hexanol, 16-mercaptohexadecanoic acid, and 2-methyl-2-propanethiol solutions, respectively. Similar to previous

alkanethiols, only thiols, and Au related ions are shown in these samples. Little glass related ions are observed from these mass spectra.

Surface coverages of thiols were calculated by the coincidence method. The detailed description of this methodology is discussed in Chapter II. The thiol-related ions SH^-, C_2HS^- and AuS^- are chosen to calculate the surface coverage of different thiol films by equations 2.6-2.10. Table 5.2 shows the surface coverage results of various thiols on Au/glass substrates. They are all close to the complete coverage, which means the high-quality self-assembly layer could be formed by using an appropriate immersion.

Table 5.2 Surface coverage of different thiols on Au-coated glass substrates.

Sample	Chemical name	Surface thiols coverage
C8	Octanethiol	~95%
C14	Tetradecanethiol	~97%
C18	Octadecanethiol	~98%
6M1H	6-Mercapto-1-hexanol	~98%
16M	16-Mercapthohexadecanoic acid	~96%
2M2P	2-Methyl-2-propanethiol	~96%

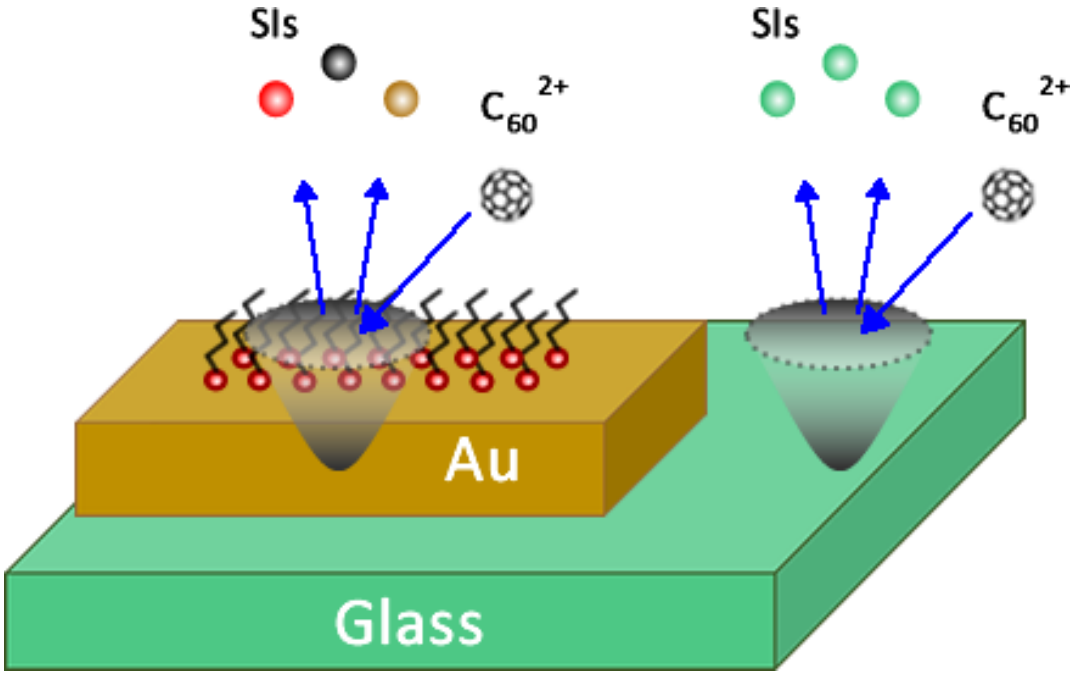

Figure 5.8 Schematic illustration of C_{60}^{2+} impacted on the octadecanethiol adsorbed Au-coated glass surface.

Characterization of octadecanethiols adsorption on Au

The schematic illustration of applying event-by-event bombardment-detection mode to probe the thiolated surface is shown in Figure 5.8. The C_{60} projectiles impact randomly on the surface with different chemical compositions. The first event on the left demonstrates that a single C_{60}^{2+} impacts on the octadecanethiol/Au region, and the detection of co-emitted SIs from both alkanethiol and Au. The second event on the right illustrates that the C_{60}^{2+} impacts on a bare glass surface. All individual events are

extracted and recorded that allows one to collect a coincidental mass spectrum of co-emitted ions with a selected ion [111].

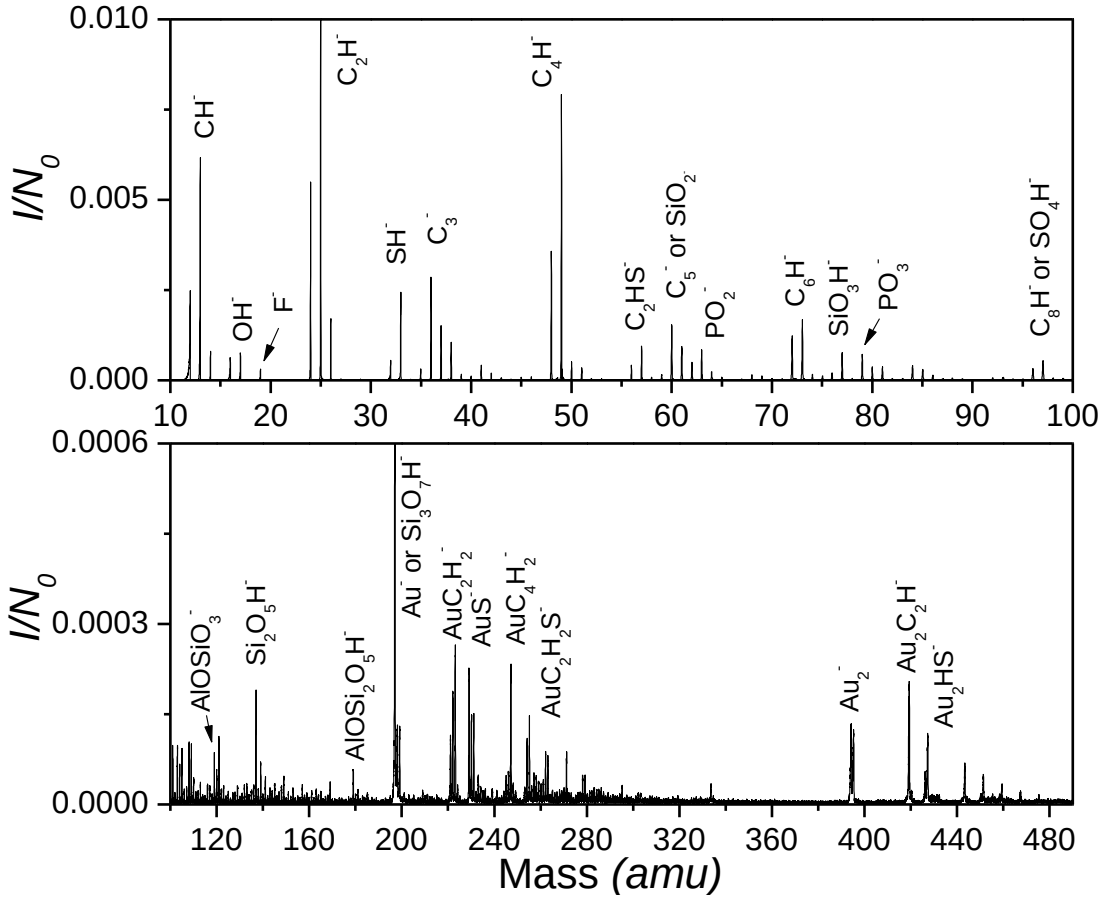

Figure 5.9 The negative secondary ion mass spectra of octadecanethiol adsorbed on the 20nm thick Au-coated glass.

Figure 5.9 shows the negative ion mass spectrum of octadecanethiol on 20 nm thick Au-coated glass slides. Other than ions from alkanethiol and Au, a series of glass-related ions at *m/z* 77 (SiO_3H^-), 119 [$AlO(SiO_3)^-$], 137 ($Si_2O_5H^-$), and 179 [$AlO(Si_2O_5H)^-$] are observed, which indicates free glasses expose to the surface. It is probably because the average thickness of the deposited Au on the glass is only 10-20 nm, forming a grain textured surface instead of a complete and thick layer of Au films.

Coincidence ion mass spectrum can reveal the surface ensemble by examining co-emitted ions. Figure 5.10 compares mass spectra of coincidental ions with SH^- and SiO_3H, respectively. The co-emission mass spectrum of the thiol-related ion, C_2HS^-, shows that the octadecanethiol and Au related ions are enhanced (Figure 5.10a). It shows that alkanethiol and Au species are co-emitted from the same domain/location. On the contrary, co-emitted ions with SiO_3H^- displays the depression of octadecanethiol and Au related SIs in Figure 5.10b, confirming that octadecanethiols do not adsorb on the glass. Meanwhile, glass-related ions SiO_2^-, $AlO(SiO_3)^-$, $Si_2O_5H^-$, and $AlO(Si_2O_5)^-$ are enhanced in the coincidental mass spectrum with SiO_3H^- (Figure 5.10b), which suggests that these ions originate from the glass. These results provide the direct evidence that alkanethiols adsorb on the Au substrate instead of glasses.

The correlation coefficient (Q) can be used to discuss the co-localization of chemical assemblies on the surface as well. The detail of this method is discussed in Chapter II. For the octadecanethiol sample shown in Figure 5.9, the Q of thiol-related ions with silica ions [e.g., Q(HS^-, SiO_3H^-) and Q(C_2HS^-, SiO_3H^-)] are less than one (~0.6), showing an anti-correlated relationship between octadecanethiol molecules and glass. Similarly,

Au and glass are anti-correlated as well because their Q values [e.g., $Q(Au^-,Si_2O_5H^-)$ and $Q(Au^-,SiO_3H^-)$] are ~0.8. Comparatively, Q values of thiol-related and Au ions [e.g., $Q(HS^-, Au^-)$, and $Q(C_2HS^-, Au^-)$] are consistent ~1.1, suggesting these ions are correlated with each other. As a result, both coincidental mass spectra and correlation coefficient confirms that octadecanethiol molecules adsorb on the Au substrate.

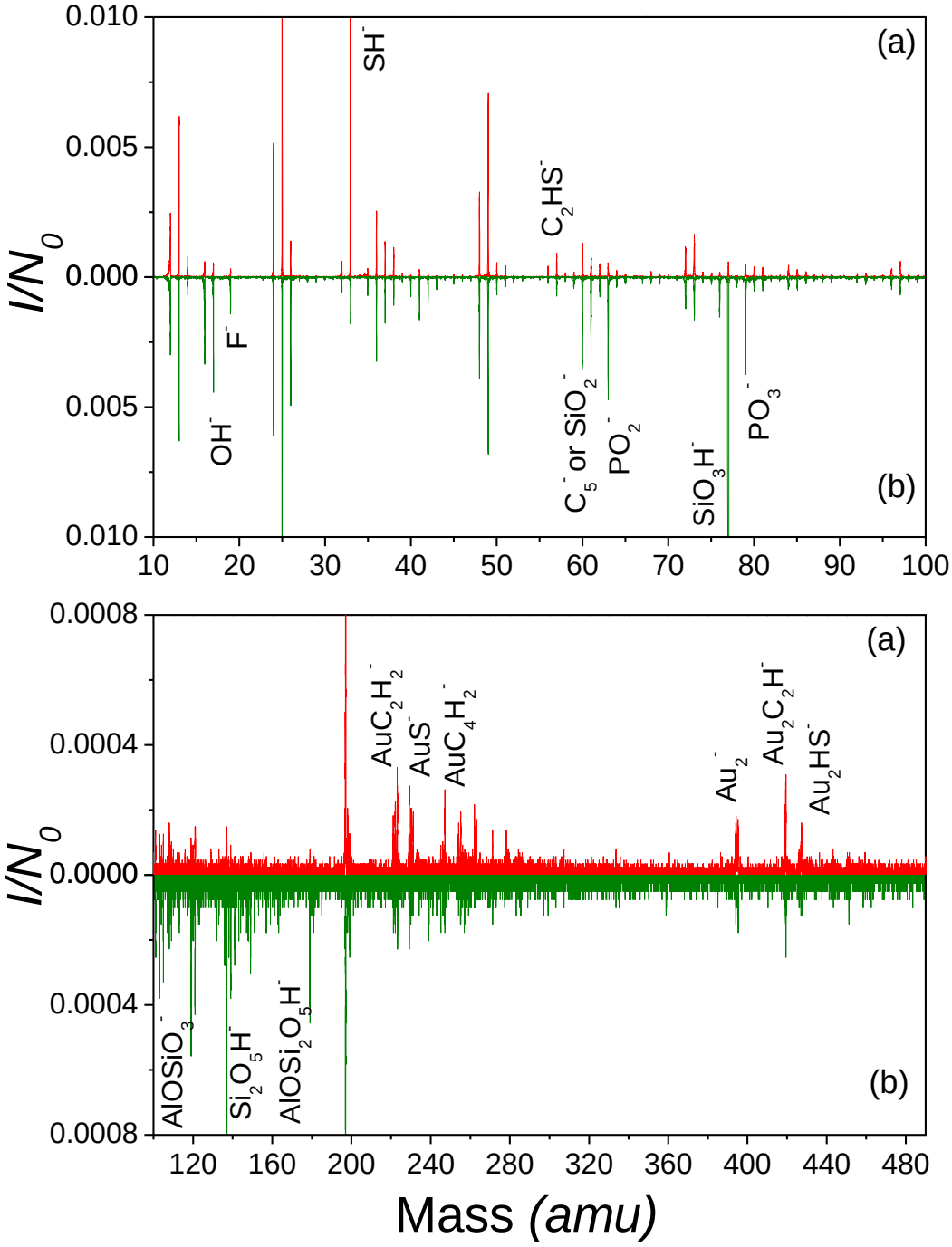

Figure 5.10 Comparison of coincidental ion mass spectra of octadecanethiol adsorbed on an Au-coated glass of co-emitted ions with (a) SH^- and (b) SiO_3H^-.

Surface octadecanethiol coverage kinetics

Previous studies have shown that SAM formation occurs in two steps, a fast initial step of (physical) adsorption and a second slower step of monolayer organization [179-181]. Adsorption occurs at the interface of different chemicals and phases. The approach of molecules to the surface occurs because of a combination of diffusion and convective transport. According to the Langmuir kinetic model, the rate of deposition onto the surface is proportional to the free space of the surface [148].

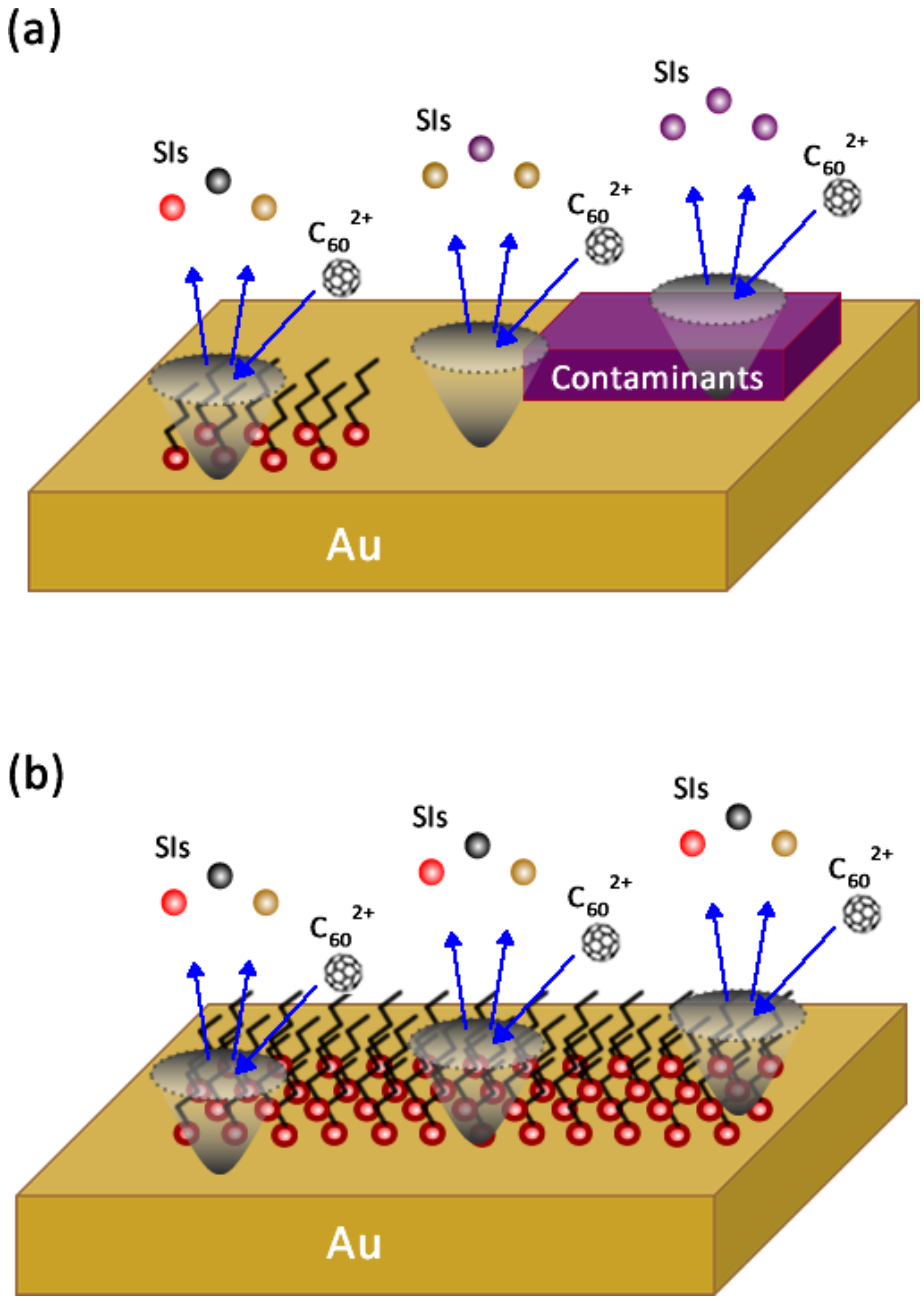

Figure 5.11 Schematic illustration of C_{60}^{2+} impacted on the (a) partially surfaces covered and (b) fully covered octadecanethiol assembled on Au.

Freshly deposited Au-coated glasses and commercially available Au-coated Si wafers are used to study the adsorption kinetics of octadecanethiols on Au. The thickness of the deposited Au layer is more than 50 nm to make sure no glass components are exposed on the surface. Oxygen plasma was used to clean the natural growth thiols and sulfur-related contaminants when they revealed in an ambient condition for a long time. However, it generated recontaminations (usually is oxidizes) after the oxygen plasma cleaning [182, 183]. Figure 5.11 shows the impact of C_{60} clusters on the alkanethiols assemblies on Au surface. When alkanethiol molecules partially cover the surface of Au, only the emitted SIs from each event do not always contain thiol related ions (Figure 5.11a). However, ions from thiols will be found from everywhere if thiols form a whole layer on the top of Au. As a result, surface thiol coverage is capable of characterizing the adsorption kinetics of the self-assembly process.

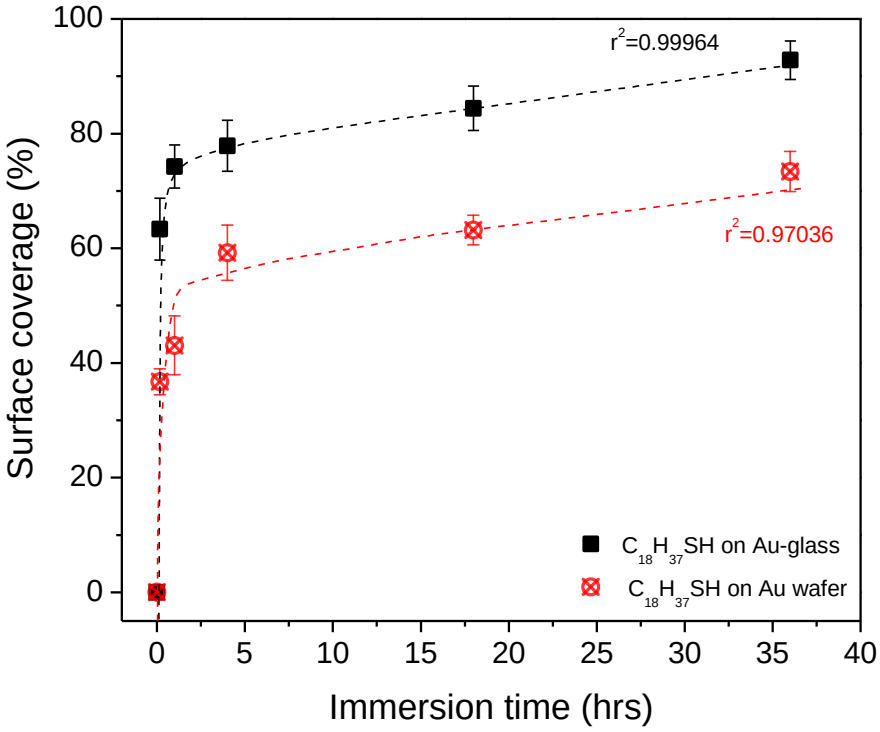

Figure 5.12 Surface coverages of octadecanethiols as a function of time.

Both Au-coated glass slides and Au-coated Si wafers are immersed into 1mM octadecanethiol solutions from a few minutes to numerous hours. Their surface coverage in octadecanethiol is directly shown in Figure 5.12. Their surface coverages exhibit a similar increasing trend, associated with two distinguish steps. The first step has surface coverages rising very quickly from a few minutes to about couple hours, which involves an initial fast physisorption process of octadecanethiols. This step is compared to the

simple Langmuir or Avrami kinetic model, which assumes that the rate of deposition is proportional to the free space on the surface, that is,

$$k_1(1-\theta) = \frac{d\theta}{dt} \quad 5.1$$

Where θ is the proportional amount of surface area deposited and k_1 is the rate constant of the first step. The *t* is the immersion time [148, 184].

Then, the second step shows surface coverages rising slowly before reaching saturation (>90% surface coverage) after more than three hours of immersion. This step may involve the monolayer organization of octadecanethiol molecules. A second step was found to follow zero-order kinetics. [148, 184]. Once the octadecanethiol molecules are at the surface, the self-organization occurs in three phases, which includes a low-density phase, an intermediate density phase, and a high-density phase. A subdued increase of the thiol coverage after few hours suggests that low coverage or intermediate phase (with a random dispersion or lying flat on the Au substrate) progressively transforms to a high-density phase with close-packed orders and thiol molecules standing vertically.

The exact mechanisms of SAM formation depend on adsorbates, solvent and substrate properties, e.g., the cleanliness of the substrate. Imperfections or impurities can cause defects in the form of SAMs. It might also reveal a phase transition occurred during an alkanethiol immersion. The octadecanethiol molecules do not form a uniform layer on the surface of Au-coated Si because of obstructions from the dirt or contamination at first. The assumption in previous studies [185] states that the formation of SAMs is an exchange process, and the thiol molecules displace unexpected adsorbates

before immersion. Dislodgement with thiol molecules requires desorption of the adsorbates already present at the first stage. Therefore, the kinetics of SAMs formation is influenced by the rate of desorption of contaminants [162, 173]. It might explain the surface coverage of thiols from the oxygen plasma treated Au is always lower than that from the freshly prepared Au.

To fit kinetic data for SAM growth, we derivate equations (7) and (8) to express θ:

$$\theta = a[1 - \exp(-k_1 t)] \quad 5.2$$

$$\theta = b + k_2 t \quad 5.3$$

Where k_2 is the rate constant of the second step. The a and b are correction parameters that relate to the cleanliness of the Au surface. The combination of equations (7) and (8) fits curves of thiol coverages as a function of time well. The r^2 for curves of fresh deposited Au and oxygen plasma cleaned Au are 0.99964 and 0.97036, respectively. The time constant τ is one over k. In the quick step, the estimate τ are 5.3 min and 7.4 min for the fresh deposited Au and oxygen plasma cleaned Au samples, which are close to previous studies [186].

Conclusions

This study illustrates SIMS to validate the adsorption of octadecanethiol on Au surfaces and quantify the surface coverage of alkanethiol SAMs. Surface homogeneity and coverage analysis derived from the coincidental SIMS have been proved to be valuable in studies of the kinetics of alkanethiol adsorptions and the formation of SAMs.

The cluster SIMS with the event-by-event bombardment-detection mode has a promising future for the kinetic and adsorption study of thin films.

CHAPTER VI

CONCLUSIONS

The purpose of this work was to develop and validate SIMS using nanoprojectiles, specifically C_{60} and Au_{400}, for the characterization of nanodomains, the measurement of surface homogeneity and the study of surface adsorption. C_{60} and Au_{400} at hyper-velocity cause emission of multiple SIs. It is thus feasible to run experiments in the event-by-event bombardment-detection mode where SIs from each individual projectile impact are recorded separately. The co-emitted SIs originate from co-localized components, hence enabling nanodomain analysis.

The innovative concept of coincidence mass spectrometry was demonstrated with the study of thin macromolecules films. The nature and relative intensities of the ionized ejecta are related to the composition and spatial arrangement of the thin film. Segregation of polymeric functional groups within nano-volume can be detected. Experiments with more compact molecular structures are needed to determine the size limits of nanodomains that can be distinguished.

The SIMS study of different types of plant surfaces has shown the ability to identify different chemical groups (e.g. hydrocarbons and fatty acids). Surface chemical homogeneity as well as the degree of polymer coatings from the coincidence secondary ions provide additional information of natural or modified plant surfaces. The study of surface adsorption and self-assembly of alkanethiol monolayers, with the ability to

determine surface homogeneity and coverage, demonstrates the details to study thermodynamic and kinetic aspects of various films at the nanoscale.

The full range of applications and the limits of our SIMS mode remain to be explored. The mechanism(s) of secondary ion emission, critical for studying the chemical composition of nano-metric surfaces or interfaces, remains to be better understood as it applies to complex polymeric and biological samples. There is room for further development of this SIMS methodology, foremost high-resolution mapping, highly sensitive co-localization detection, and accurate identification of molecular ions.

REFERENCES

[1] T.E. Madey, C.H. Nien, K. Pelhos, J.J. Kolodziej, I.M. Abdelrehim, H.S. Tao, Faceting induced by ultrathin metal films: structure, electronic properties and reactivity, Surface Science, 438 (1999) 191-206.

[2] F.S.S. Chien, J.W. Chang, S.W. Lin, Y.C. Chou, T.T. Chen, S. Gwo, T.S. Chao, W.F. Hsieh, Nanometer-scale conversion of Si_3N_4 to SiO_x, Applied Physics Letters, 76 (2000) 360.

[3] T. Yamada, T. Inoue, K. Yamada, N. Takano, T. Osaka, H. Harada, K. Nishiyama, I. Taniguchi, Detection of C-Si covalent bond in CH_3 adsorbate formed by chemical reaction of CH_3MgBr and H:Si(111), Journal of the American Chemical Society, 125 (2003) 8039-8042.

[4] K. Nishiyama, Y. Tanaka, H. Harada, T. Yamada, D. Niwa, T. Inoue, T. Homma, T. Osaka, I. Taniguchi, Adsorption of organic molecules by photochemical reaction on Cl:Si(111) and H:Si(111) evaluated by HREELS, Surface Science, 600 (2006) 1965-1972.

[5] R. Gómez, M.J. Weaver, Electrochemical Infrared Studies of Monocrystalline Iridium Surfaces. Part 2: Carbon Monoxide and Nitric Oxide Adsorption on Ir(110), Langmuir, 14 (1998) 2525-2534.

[6] S. Zou, M.J. Weaver, Spatial structure of ordered electrochemical adlayers from in situ scanning tunneling microscopy and infrared spectroscopy: single-site carbon monoxide binding on iridium(111) and comparisons with related systems, Surface Science, 446 (2000) L95-L100.

[7] L. Borgese, A. Zacco, E. Bontempi, P. Colombi, R. Bertuzzi, E. Ferretti, S. Tenini, L.E. Depero, Total reflection of x-ray fluorescence (TXRF): a mature technique for environmental chemical nanoscale metrology, Measurement Science and Technology, 20 (2009) 084027.

[8] R. Miller, Z. Guo, E.A. Vogler, C.A. Siedlecki, Plasma coagulation response to surfaces with nanoscale chemical heterogeneity, Biomaterials, 27 (2006) 208-215.

[9] D.R. Baer, M.H. Engelhard, XPS analysis of nanostructured materials and biological surfaces, Journal of Electron Spectroscopy and Related Phenomena, 178-179 (2010) 415-432.

[10] C.L. Cheung, S.W. Chung, A. Chatterji, T.W. Lin, J.E. Johnson, S. Hok, J. Perkins, J.J. De Yoreo, Physical controls on directed virus assembly at nanoscale chemical templates, Journal of the American Chemical Society, 128 (2006) 10801-10807.

[11] C. Srinivasan, T.J. Mullen, J.N. Hohman, M.E. Anderson, A.A. Dameron, A.M. Andrews, E.C. Dickey, M.W. Horn, P.S. Weiss, Scanning electron microscopy of nanoscale chemical patterns, Acs Nano, 1 (2007) 191-201.

[12] J.K. Gimzewski, C. Joachim, Nanoscale science of single molecules using local probes, Science, 283 (1999) 1683-1688.

[13] K.F. Kelly, I.W. Chiang, E.T. Mickelson, R.H. Hauge, J.L. Margrave, X. Wang, G.E. Scuseria, C. Radloff, N.J. Halas, Insight into the mechanism of sidewall functionalization of single-walled nanotubes: an STM study, Chemical Physics Letters, 313 (1999) 445-450.

[14] I.L. Medintz, A.R. Clapp, H. Mattoussi, E.R. Goldman, B. Fisher, J.M. Mauro, Self-assembled nanoscale biosensors based on quantum dot FRET donors, Nature Materials, 2 (2003) 630-638.

[15] H.J. Kong, T.R. Polte, E. Alsberg, D.J. Mooney, FRET measurements of cell-traction forces and nano-scale clustering of adhesion ligands varied by substrate stiffness, Proceedings of the National Academy of Sciences of the United States of America, 102 (2005) 4300-4305.

[16] F. Ratto, S. Heun, O. Moutanabbir, F. Rosei, In situ nanoscale mapping of the chemical composition of surfaces and 3D nanostructures by photoelectron spectromicroscopy, Nanotechnology, 19 (2008) 265703.

[17] K. Horiba, Y. Nakamura, N. Nagamura, S. Toyoda, H. Kumigashira, M. Oshima, K. Amemiya, Y. Senba, H. Ohashi, Scanning photoelectron microscope for nanoscale three-dimensional spatial-resolved electron spectroscopy for chemical analysis, Review of Scientific Instruments, 82 (2011) 113701.

[18] T. Okuda, T. Eguchi, K. Akiyama, A. Harasawa, T. Kinoshita, Y. Hasegawa, M. Kawamori, Y. Haruyama, S. Matsui, Nanoscale chemical imaging by scanning tunneling microscopy assisted by synchrotron radiation, Physical Review Letters, 102 (2009) 105503.

[19] E. de Smit, I. Swart, J.F. Creemer, G.H. Hoveling, M.K. Gilles, T. Tyliszczak, P.J. Kooyman, H.W. Zandbergen, C. Morin, B.M. Weckhuysen, F.M.F. de Groot, Nanoscale chemical imaging of a working catalyst by scanning transmission X-ray microscopy, Nature, 456 (2008) 222-U239.

[20] B.S. Yeo, T. Schmid, W. Zhang, R. Zenobi, Towards rapid nanoscale chemical analysis using tip-enhanced Raman spectroscopy with Ag-coated dielectric tips, Analytical and Bioanalytical Chemistry, 387 (2007) 2655-2662.

[21] F. De Angelis, G. Das, P. Candeloro, M. Patrini, M. Galli, A. Bek, M. Lazzarino, I. Maksymov, C. Liberale, L.C. Andreani, E. Di Fabrizio, Nanoscale chemical mapping using three-dimensional adiabatic compression of surface plasmon polaritons, Nature Nanotechnology, 5 (2010) 67-72.

[22] J. Stadler, T. Schmid, R. Zenobi, Nanoscale Chemical Imaging Using Top-Illumination Tip-Enhanced Raman Spectroscopy, Nano Letters, 10 (2010) 4514-4520.

[23] N. Hayazawa, M. Motohashi, Y. Saito, H. Ishitobi, A. Ono, T. Ichimura, P. Verma, S. Kawata, Visualization of localized strain of a crystalline thin layer at the

nanoscale by tip-enhanced Raman spectroscopy and microscopy, Journal of Raman Spectroscopy, 38 (2007) 684-696.

[24] L. Cassiday, SIMS and MALDI: better together, Analytical Chemistry, 80 (2008) 8860-8860.

[25] A. Brown, J.C. Vickerman, Static SIMS, FABMS and SIMS imaging in applied surface analysis, The Analyst, 109 (1984) 851.

[26] T.L. Salter, F.M. Green, I.S. Gilmore, M.P. Seah, P. Stokes, A comparison of SIMS and DESI and their complementarities, Surface and Interface Analysis, 43 (2011) 294-297.

[27] J.M. Miller, Fast-Atom Bombardment Mass Spectrometry and Related Techniques, Advances in Inorganic Chemistry, 28 (1984) 1-27.

[28] B.J. Garrison, A. Delcorte, L.V. Zhigilei, T.E. Itina, K.D. Krantzman, Y.G. Yingling, C.M. McQuaw, E.J. Smiley, N. Winograd, Big molecule ejection—SIMS vs. MALDI, Applied Surface Science, 203-204 (2003) 69-71.

[29] I. Talian, A. Orinak, J. Preisler, A. Heile, L. Onofrejova, D. Kaniansky, H.F. Arlinghaus, Comparative TOF-SIMS and MALDI TOF-MS analysis on different chromatographic planar substrates, Journal of Separation Science, 30 (2007) 2570-2582.

[30] P. Williams, Secondary ion mass spectrometry, Annual Review of Materials Science, 15 (1985) 517-548.

[31] P. Zalm, Secondary ion mass spectrometry, Vacuum, 45 (1994) 753-772.

[32] A. Benninghoven, F. Rudenauer, H.W. Werner, Secondary ion mass spectrometry: basic concepts, instrumental aspects, applications and trends, (1987).

[33] R.G. Wilson, F.A. Stevie, C.W. Magee, Secondary ion mass spectrometry: a practical handbook for depth profiling and bulk impurity analysis, Wiley-Interscience1989.

[34] H. Oechsner, W. Rühe, E. Stumpe, Comparative SNMS and SIMS studies of oxidized Ce and Gd, Surface Science, 85 (1979) 289-301.

[35] C.D. Moak, H.E. Banta, J.N. Thurston, J.W. Johnson, R.F. King, Duo Plasmatron Ion Source for Use in Accelerators, Review of Scientific Instruments, 30 (1959) 694.

[36] J.J. Vajo, R.E. Doty, E.H. Cirlin, Influence of O_2^+ energy, flux, and fluence on the formation and growth of sputtering-induced ripple topography on silicon, Journal of Vacuum Science & Technology A, 14 (1996) 2709-2720.

[37] W. Reuter, A SIMS-XPS study on silicon and germanium under O_2^+bombardment, Nuclear Instruments and Methods in Physics Research Section B: Beam Interactions with Materials and Atoms, 15 (1986) 173-175.

[38] S. Tan, K. Yeo, A. Wee, In situ XPS and SIMS analysis of O_2^+ beam-induced silicon oxidation, Surface and Interface Analysis, 36 (2004) 640-644.

[39] L.Y. Ming, W. Reuter, Matrix effect in SIMS analysis using an O_2^+ primary beam, Journal of Vacuum Science and Technology, 17 (1980) 36-39.

[40] G. Mezey, E. Kótai, T. Nagy, L. Lohner, A. Manuba, J. Gyulai, V. Deline, C. Evans, R. Blattner, A comparison of techniques for depth profiling oxygen in silicon, Nuclear Instruments and Methods, 167 (1979) 279-287.

[41] J.F. Mahoney, Electrohydrodynamic Ion Source, Journal of Applied Physics, 40 (1969) 5101.

[42] G. Caskey, R.A. Douglas, H. Richards, H.V. Smith, A simple negative-ion sputter source, Nuclear Instruments and Methods, 157 (1978) 1-7.

[43] A.M. Falick, G.H. Wang, F.C. Walls, Ion source for liquid matrix secondary ionization mass spectrometry, Analytical Chemistry, 58 (1986) 1308-1311.

[44] L.W. Swanson, Liquid metal ion sources: Mechanism and applications, Nuclear Instruments and Methods in Physics Research, 218 (1983) 347-353.

[45] N. Davies, D.E. Weibel, P. Blenkinsopp, N. Lockyer, R. Hill, J.C. Vickerman, Development and experimental application of a gold liquid metal ion source, Applied Surface Science, 203-204 (2003) 223-227.

[46] L.W. Swanson, G.A. Schwind, A.E. Bell, Measurement of the energy distribution of a gallium liquid metal ion source, Journal of Applied Physics, 51 (1980) 3453.

[47] L.W. Swanson, Use of the liquid metal ion source for focused beam applications, Applied Surface Science, 76-77 (1994) 80-88.

[48] M. Tajmar, Influence of Taylor cone size on droplet generation in an indium liquid metal ion source, Applied Physics A, 81 (2005) 1447-1450.

[49] L. Bischoff, W. Pilz, T. Ganetsos, R.G. Forbes, C. Akhmadaliev, GaBi alloy liquid metal ion source for microelectronics research, Ultramicroscopy, 107 (2007) 865-868.

[50] L.W. Swanson, Emission characteristics of gallium and bismuth liquid metal field ion sources, Journal of Vacuum Science and Technology, 16 (1979) 1864.

[51] F. Stevie, D. Griffis, Quantification in dynamic SIMS: Current status and future needs, Applied Surface Science, 255 (2008) 1364-1367.

[52] P.C. Zalm, Dynamic SIMS: Quantification at All Depths?, Microchimica Acta, 132 (2000) 243-257.

[53] C.A. Sims, T. Zha, Bayesian Methods for Dynamic Multivariate Models, International Economic Review, 39 (1998) 949.

[54] G. Gillen, A. Fahey, M. Wagner, C. Mahoney, 3D molecular imaging SIMS, Applied Surface Science, 252 (2006) 6537-6541.

[55] L. Van Vaeck, A. Adriaens, R. Gijbels, Static secondary ion mass spectrometry (S-SIMS) Part 1: methodology and structural interpretation, Mass Spectrometry Reviews, 18 (1999) 1-47.

[56] R.N. Sodhi, Time-of-flight secondary ion mass spectrometry (TOF-SIMS):--versatility in chemical and imaging surface analysis, Analyst, 129 (2004) 483-487.

[57] R.N. Sodhi, Time-of-flight secondary ion mass spectrometry (TOF-SIMS):—versatility in chemical and imaging surface analysis, Analyst, 129 (2004) 483-487.

[58] I.S. Gilmore, M.P. Seah, Static SIMS: A Study of Damage Using Polymers, Surface and Interface Analysis, 24 (1996) 746-762.

[59] N. Winograd, Z. Postawa, J. Cheng, C. Szakal, J. Kozole, B.J. Garrison, Improvements in SIMS continue: Is the end in sight?, Applied Surface Science, 252 (2006) 6836-6843.

[60] N. Winograd, The magic of cluster SIMS, Analytical Chemistry, 77 (2005) 142 A-149 A.

[61] F. Kollmer, Cluster primary ion bombardment of organic materials, Applied Surface Science, 231-232 (2004) 153-158.

[62] S. Ninomiya, Y. Nakata, K. Ichiki, T. Seki, T. Aoki, J. Matsuo, Measurements of secondary ions emitted from organic compounds bombarded with large gas cluster

ions, Nuclear Instruments and Methods in Physics Research Section B: Beam Interactions with Materials and Atoms, 256 (2007) 493-496.

[63] T. Gruendling, S. Weidner, J. Falkenhagen, C. Barner-Kowollik, Mass spectrometry in polymer chemistry: a state-of-the-art up-date, Polymer Chemistry, 1 (2010) 599-617.

[64] F. Kötter, A. Benninghoven, Secondary ion emission from polymer surfaces under Ar^+, Xe^+ and SF_5^+ ion bombardment, Applied Surface Science, 133 (1998) 47-57.

[65] K. Boussofiane-Baudin, G. Bolbach, A. Brunelle, S. Della-Negra, P. Håkansson, Y. Le Beyec, Secondary ion emission under cluster impact at low energies (5–60 keV); influence of the number of atoms in the projectile, Nuclear Instruments and Methods in Physics Research Section B: Beam Interactions with Materials and Atoms, 88 (1994) 160-163.

[66] D. Weibel, S. Wong, N. Lockyer, P. Blenkinsopp, R. Hill, J.C. Vickerman, A C60 primary ion beam system for time of flight secondary ion mass spectrometry: its development and secondary ion yield characteristics, Analytical Chemistry, 75 (2003) 1754-1764.

[67] A. Wucher, Molecular secondary ion formation under cluster bombardment: A fundamental review, Applied Surface Science, 252 (2006) 6482-6489.

[68] G. Gillen, A. Fahey, Secondary ion mass spectrometry using cluster primary ion beams, Applied Surface Science, 203-204 (2003) 209-213.

[69] F. Grønlund, W.J. Moore, Sputtering of Silver by Light Ions with Energies from 2 to 12 kev, The Journal of Chemical Physics, 32 (1960) 1540.

[70] P. Rol, J. Fluit, J. Kistemaker, Sputtering of Copper by bombardment with ions of 5–25 KeV, Physica, 26 (1960) 1000-1008.

[71] A.D. Appelhans, J.E. Delmore, Comparison of polyatomic and atomic primary beams for secondary ion mass spectrometry of organics, Analytical Chemistry, 61 (1989) 1087-1093.

[72] R.D. Harris, M.J. Van Stipdonk, E.A. Schweikert, Kiloelectron volt cluster impacts: prospects for cluster-SIMS, International Journal of Mass Spectrometry and Ion Processes, 174 (1998) 167-177.

[73] N.K. Dzhemilev, A.M. Goldenberg, I.V. Veriovkin, S.V. Verkhoturov, Fragmentation of cluster ions in SIMS: cluster distributions over lifetime, excitation energy and kinetic energy release, Nuclear Instruments and Methods in Physics Research Section B: Beam Interactions with Materials and Atoms, 114 (1996) 245-251.

[74] E.A. Schweikert, M.G. Blain, M.A. Park, E.F. Da Silveira, Surface characterization with keV clusters and MeV ions, Nuclear Instruments and Methods in Physics Research Section B: Beam Interactions with Materials and Atoms, 50 (1990) 307-313.

[75] S.V. Verkhoturov, E.A. Schweikert, A novel approach for coincidence ion mass spectrometry, Analytical and Bioanalytical Chemistry, 373 (2002) 609-611.

[76] S. Verkhoturov, E. Schweikert, N. Rizkalla, Surface mass spectrometry at the submicrometer scale, Langmuir, 18 (2002) 8836-8840.

[77] S. Della-Negra, J. Arianer, J. Depauw, S.V. Verkhoturov, E.A. Schweikert, The Pegase project, a new solid surface probe: focused massive cluster ion beams, Surface and Interface Analysis, 43 (2011) 66-69.

[78] J.D. Debord, F.A. Fernandez-Lima, S.V. Verkhoturov, E.A. Schweikert, S. Della-Negra, Characteristics of positive and negative secondary ions emitted from Au_3^+ and Au_{400}^{4+} impacts, Surface and Interface Analysis, 45 (2013) 134-137.

[79] M. Van Stipdonk, E. Schweikert, M. Park, Coincidence measurements in mass spectrometry, Journal of Mass Spectrometry, 32 (1997) 1151-1161.

[80] M.A. Park, K.A. Gibson, K. Quinones, M.A. Schweikert, Coincidence Counting in Time-of-Flight Mass Spectrometry: A Test for Chemical Microhomogeneity, Science, 248 (1990) 988-990.

[81] R. Rickman, S. Verkhoturov, E. Parilis, E. Schweikert, Simultaneous ejection of two molecular ions from keV gold atomic and polyatomic projectile impacts, Physical Review Letters, 92 (2004) 047601.

[82] C. Guillermier, S.D. Negra, R.D. Rickman, V. Pinnick, E.A. Schweikert, Influence of massive projectile size and energy on secondary ion yields from organic surfaces, Applied Surface Science, 252 (2006) 6529-6532.

[83] C. Guillermier, V. Pinnick, S.V. Verkhoturov, E.A. Schweikert, Organic SIMS with single massive gold projectile: Ion yield enhancement by silver metallization, Applied Surface Science, 252 (2006) 6644-6647.

[84] M.J. Eller, S.V. Verkhoturov, S. Della-Negra, E.A. Schweikert, Electron Emission From Hypervelocity C-60 impacts, Journal of Physical Chemistry C, 114 (2010) 17191-17196.

[85] S.V. Verkhoturov, M.J. Eller, R.D. Rickman, S. Della-Negra, E.A. Schweikert, Single Impacts of C_{60} on Solids: Emission of Electrons, Ions and Prospects for Surface Mapping, Journal of Physical Chemistry C, 114 (2010) 5637-5644.

[86] V. Pinnick, S. Rajagopalachary, S.V. Verkhoturov, L. Kaledin, E.A. Schweikert, Characterization of Individual Nano-Objects by Secondary Ion Mass Spectrometry, Analytical Chemistry, 80 (2008) 9052-9057.

[87] V.T. Pinnick, S.V. Verkhoturov, L. Kaledin, Y. Bisrat, E.A. Schweikert, Molecular identification of individual nano-objects, Analytical Chemistry, 81 (2009) 7527-7531.

[88] S. Raiagopalachary, S.V. Verkhoturov, E.A. Schweikert, Characterization of Individual Ag Nanoparticles and Their Chemical Environment, Analytical Chemistry, 81 (2009) 1089-1094.

[89] C. Anders, G. Ziegenhain, S. Zimmermann, H.M. Urbassek, Cluster-induced crater formation, Nuclear Instruments & Methods in Physics Research Section B-Beam Interactions with Materials and Atoms, 267 (2009) 3122-3125.

[90] A. Delcorte, S. Yunus, N. Wehbe, N. Nieuwjaer, C. Poleunis, A. Felten, L. Houssiau, J.J. Pireaux, P. Bertrand, Metal-assisted secondary ion mass spectrometry using atomic (Ga^+, In^+) and fullerene projectiles, Analytical Chemistry, 79 (2007) 3673-3689.

[91] Z. Li, S.V. Verkhoturov, J.E. Locklear, E.A. Schweikert, Secondary ion mass spectrometry with C_{60}^+ and Au_{400}^{4+} projectiles: Depth and nature of secondary ion emission from multilayer assemblies, International Journal of Mass Spectrometry, 269 (2008) 112-117.

[92] L.J. Chen, S.S. Shah, J. Silangcruz, M.J. Eller, S.V. Verkhoturov, A. Revzin, E.A. Schweikert, Characterization and quantification of nanoparticle-antibody conjugates on cells using C-60 ToF SIMS in the event-by-event bombardment/detection mode, International Journal of Mass Spectrometry, 303 (2011) 97-102.

[93] L.J. Chen, S.S. Shah, S.V. Verkhoturov, A. Revzin, E.A. Schweikert, Characterization and quantification of biological micropatterns using cluster SIMS, Surface and Interface Analysis, 43 (2011) 555-558.

[94] S. Della-Negra, J. Depauw, C. Guillermier, E.A. Schweikert, Massive clusters: Secondary emission from qkeV to qMeV. New emission processes? New SIMS probe?, Surface and Interface Analysis, 43 (2011) 62-65.

[95] S. Bouneau, S. Della-Negra, J. Depauw, D. Jacquet, Y. Le Beyec, J.P. Mouffron, A. Novikov, M. Pautrat, Heavy gold cluster beams production and identification, Nuclear Instruments and Methods in Physics Research Section B: Beam Interactions with Materials and Atoms, 225 (2004) 579-589.

[96] G. Curtis, J. Silcox, A Wien filter for use as an energy analyzer with an electron microscope, Review of Scientific Instruments, 42 (1971) 630-637.

[97] J.L. Wiza, Microchannel Plate Detectors, Nuclear Instruments and Methods, 162 (1979) 587-601.

[98] C. Catchpole, C. Johnson, The multianode photomultiplier, Publications of the Astronomical Society of the Pacific, (1972) 134-136.

[99] J.E. Locklear, Secondary ion emission under keV carbon cluster bombardment, Chemistry, Texas A&M University, 2006.

[100] R.D. Rickman, Secondary ion emission from “super-efficient” events: prospects for surface mass spectrometry, Chemistry, Texas A&M University, 2004.

[101] P. Steffens, A time-of-flight mass spectrometer for static SIMS applications, Journal of Vacuum Science & Technology A: Vacuum, Surfaces, and Films, 3 (1985) 1322.

[102] R. Grix, R. Kutscher, G. Li, U. Grüner, H. Wollnik, H. Matsuda, A time-of-flight mass analyzer with high resolving power, Rapid Communications in Mass Spectrometry, 2 (1988) 83-85.

[103] J.D. Debord, S. Della-Negra, F.A. Fernandez-Lima, S.V. Verkhoturov, E.A. Schweikert, Bi-Directional Ion Emission from Massive Gold Cluster Impacts on Nanometric Carbon Foils, Journal of Physical Chemistry C, 116 (2012) 8138-8144.

[104] L.J. Chen, Characterization and Quantification of Biological Surfaces Using Cluster ToF-SIMS with the Event-By-Event Bombardment/Detection Mode, Chemistry, Texas A&M University, 2012.

[105] W. Wiley, I.H. McLaren, Time-of-flight mass spectrometer with improved resolution, Review of Scientific Instruments, 26 (1955) 1150-1157.

[106] M.J. Eller, S.V. Verkhoturov, S. Della-Negra, E.A. Schweikert, SIMS instrumentation and methodology for mapping of co-localized molecules, Rev Sci Instrum, 84 (2013) 103706.

[107] M.J. Eller, S.V. Verkhoturov, S. Della-Negra, E.A. Schweikert, SIMS instrumentation and methodology for mapping of co-localized molecules, Review of Scientific Instruments, 84 (2013) In press.

[108] Z. Li, S.V. Verkhoturov, E.A. Schweikert, Nanovolume analysis with secondary ion mass spectrometry using massive projectiles, Analytical Chemistry, 78 (2006) 7410-7416.

[109] L.J. Chen, J.H. Seo, M.J. Eller, S.V. Verkhoturov, S.S. Shah, A. Revzin, E.A. Schweikert, Quantitative label-free characterization of avidin-biotin assemblies on silanized glass, Analytical Chemistry, 83 (2011) 7173-7178.

[110] R.D. Harris, M.J. Van Stipdonk, E.A. Schweikert, Kiloelectron volt cluster impacts: prospects for cluster-SIMS, International Journal of Mass Spectrometry and Ion Processes, 174 (1998) 167-177.

[111] L.J. Chen, S.S. Shah, J. Silangcruz, M.J. Eller, S.V. Verkhoturov, A. Revzin, E.A. Schweikert, Characterization and Quantification of Nanoparticle-Antibody Conjugates on Cells Using C(60) ToF SIMS in the Event-By-Event Bombardment/Detection Mode, International Journal of Mass Spectrometry, 303 (2011) 97-102.

[112] H.-C. Kim, S.-M. Park, W.D. Hinsberg, Block Copolymer Based Nanostructures: Materials, Processes, and Applications to Electronics, Chemical Reviews, 110 (2009) 146-177.

[113] J. Bang, U. Jeong, D.Y. Ryu, T.P. Russell, C.J. Hawker, Block Copolymer Nanolithography: Translation of Molecular Level Control to Nanoscale Patterns, Advanced Materials, 21 (2009) 4769-4792.

[114] C.J. Hawker, T.P. Russell, Block copolymer lithography: Merging “bottom-up” with “top-down” processes, Mrs Bulletin, 30 (2005) 952-966.

[115] D. Briggs, Surface analysis of polymers by XPS and static SIMS, Cambridge University Press1998.

[116] C.M. Mahoney, Cluster secondary ion mass spectrometry of polymers and related materials, Mass Spectrometry Reviews, 29 (2010) 247-293.

[117] S. Cho, F. Yang, G. Sun, M.J. Eller, C. Clark, E.A. Schweikert, J.W. Thackeray, P. Trefonas, K.L. Wooley, Directing Self-Assembly of Nanoscopic Cylindrical Diblock Brush Terpolymers into Films with Desired Spatial Orientations: Expansion of Chemical Composition Scope, Macromolecular Rapid Communications, (2013).

[118] G. Sun, S. Cho, C. Clark, S.V. Verkhoturov, M.J. Eller, A. Li, A. Pavía-Jiménez, E.A. Schweikert, J.W. Thackeray, P. Trefonas, Nanoscopic Cylindrical Dual Concentric and Lengthwise Block Brush Terpolymers as Covalent Preassembled High-Resolution and High-Sensitivity Negative-Tone Photoresist Materials, Journal of the American Chemical Society, 135 (2013) 4203-4206.

[119] C.-K. Liang, S.V. Verkhoturov, L.-J. Chen, E.A. Schweikert, Size-dependent emission of negative ions from gold nanoparticles bombarded with C60 and Au400, International Journal of Mass Spectrometry, 334 (2013) 43-48.

[120] C. Guillermier, S.D. Negra, R.D. Rickman, G.J. Hager, E.A. Schweikert, Prompt in situ emission of gold adducts from single impacts of large gold clusters on organics solids, International Journal of Mass Spectrometry, 263 (2007) 298-303.

[121] G.J. Hager, C. Guillermier, S.V. Verkhoturov, E.A. Schweikert, Au-analyte adducts resulting from single massive gold cluster impacts, Applied Surface Science, 252 (2006) 6558-6561.

[122] P. Trefonas, J.W. Thackeray, G. Sun, S. Cho, C. Clark, S.V. Verkhoturov, M.J. Eller, A. Li, A. Pavia-Sanders, E.A. Schweikert, Bottom-up/top-down, high-resolution, high-throughput lithography using vertically assembled block bottle brush polymers, Journal of Micro/Nanolithography, MEMS, and MOEMS, 12 (2013) 043006.

[123] S. Rajagopalachary, S.V. Verkhoturov, E.A. Schweikert, Examination of nanoparticles via single large cluster impacts, Nano Letters, 8 (2008) 1076-1080.

[124] S. Cho, F. Yang, G. Sun, M.J. Eller, C. Clark, E.A. Schweikert, J.W. Thackeray, P. Trefonas, K.L. Wooley, Directing Self-Assembly of Nanoscopic Cylindrical Diblock Brush Terpolymers into Films with Desired Spatial Orientations: Expansion of Chemical Composition Scope, Macromolecular Rapid Communications, 35 (2014) 437-441.

[125] C. Sinturel, M. Vayer, M. Morris, M.A. Hillmyer, Solvent Vapor Annealing of Block Polymer Thin Films, Macromolecules, 46 (2013) 5399-5415.

[126] P. Appendini, J.H. Hotchkiss, Review of antimicrobial food packaging, Innovative Food Science & Emerging Technologies, 3 (2002) 113-126.

[127] M. Saarela, G. Mogensen, R. Fondén, J. Mättö, T. Mattila-Sandholm, Probiotic bacteria: safety, functional and technological properties, Journal of biotechnology, 84 (2000) 197-215.

[128] X. Shi, X. Zhu, Biofilm formation and food safety in food industries, Trends in Food Science & Technology, 20 (2009) 407-413.

[129] R.V. Tauxe, Food safety and irradiation: protecting the public from foodborne infections, Emerging infectious diseases, 7 (2001) 516.

[130] J.L. Dalsin, P.B. Messersmith, Bioinspired antifouling polymers, Materials today, 8 (2005) 38-46.

[131] A.R. Statz, R.J. Meagher, A.E. Barron, P.B. Messersmith, New peptidomimetic polymers for antifouling surfaces, Journal of the American Chemical Society, 127 (2005) 7972-7973.

[132] G.M. Hunt, E.A. Baker, Phenolic constituents of tomato fruit cuticles, Phytochemistry, 19 (1980) 1415-1419.

[133] M.P. Velcheva, C. Donchev, Isoprenoid hydrocarbons from the fruit of extant plants, Phytochemistry, 45 (1997) 637-639.

[134] S. Santier, A. Chamel, Reassessment of the role of cuticular waxes in the transfer of organic molecules through plant cuticles, Plant Physiology and Biochemistry, 36 (1998) 225-231.

[135] S. Bauer, E. Schulte, H.-P. Thier, Composition of the surface wax from tomatoes, European Food Research and Technology, 219 (2004) 223-228.

[136] M. Saladie, A.J. Matas, T. Isaacson, M.A. Jenks, S.M. Goodwin, K.J. Niklas, R. Xiaolin, J.M. Labavitch, K.A. Shackel, A.R. Fernie, A. Lytovchenko, M.A. O'Neill, C.B. Watkins, J.K. Rose, A reevaluation of the key factors that influence tomato fruit softening and integrity, Plant Physiology, 144 (2007) 1012-1028.

[137] E. Baker, M. Bukovac, G.M. Hunt, Composition of tomato fruit cuticle as related to fruit growth and development, Linnean Society symposium series, 1982.

[138] S. Bauer, E. Schulte, H.-P. Thier, Composition of the surface wax from tomatoes, European Food Research and Technology, 219 (2004) 487-491.

[139] E.A. Baker, G.M. Hunt, P.J.G. Stevens, Studies of plant cuticle and spray droplet interactions: A fresh approach, Pesticide Science, 14 (1983) 645-658.

[140] H. Kallio, R. Nieminen, S. Tuomasjukka, M. Hakala, Cutin composition of five finnish berries, Journal of Agricultural and Food Chemistry, 54 (2006) 457-462.

[141] E. Dominguez, J.A. Heredia-Guerrero, A. Heredia, The biophysical design of plant cuticles: an overview, New Phytologist, 189 (2011) 938-949.

[142] F.M. Piras, M.F. Dettori, A. Magnani, ToF-SIMS PCA analysis of Myrtus communis L, Applied Surface Science, 255 (2009) 7805-7811.

[143] R. Jetter, R. Sodhi, Chemical composition and microstructure of waxy plant surfaces: triterpenoids and fatty acid derivatives on leaves of Kalanchoe daigremontiana, Surface and Interface Analysis, 43 (2011) 326-330.

[144] A. Tourovskaia, T. Barber, B.T. Wickes, D. Hirdes, B. Grin, D.G. Castner, K.E. Healy, A. Folch, Micropatterns of chemisorbed cell adhesion-repellent films using oxygen plasma etching and elastomeric masks, Langmuir, 19 (2003) 4754-4764.

[145] Y. Choi, H. Lee, S.T. Fountain, D.M. Lubman, Direct chemical analysis of uv laser ablation products of organic polymers by using selective ion monitoring mode in gas chromatography/mass spectrometry, Journal of the American Society for Mass Spectrometry, 5 (1994) 106-112.

[146] M. Zhang, J.K. Oh, L. Cisneros-Zevallos, M. Akbulut, Bactericidal effects of nonthermal low-pressure oxygen plasma on S. *typhimurium* LT2 attached to fresh produce surfaces, Journal of Food Engineering, 119 (2013) 425-432.

[147] M. Zhang, F. Yang, S. Pasupuleti, J.K. Oh, N. Kohli, I.S. Lee, K. Perez, S.V. Verkhoturov, E.A. Schweikert, A. Jayaraman, L. Cisneros-Zevallos, M. Akbulut, Preventing adhesion of Escherichia coli O157:H7 and Salmonella Typhimurium LT2 on tomato surfaces via ultrathin polyethylene glycol film, International Journal of Food Microbiology, 185 (2014) 73-81.

[148] D.K. Schwartz, Mechanisms and kinetics of self-assembled monolayer formation, Annu Rev Phys Chem, 52 (2001) 107-137.

[149] K. Ariga, Y. Yamauchi, G. Rydzek, Q. Ji, Y. Yonamine, J. Hill, Layer-by-layer Nanoarchitectonics: Invention, Innovation, and Evolution, Chemistry Letters, 43 (2014) 36-68.

[150] C. Tschierske, Development of structural complexity by liquid-crystal self-assembly, Angewandte Chemie International Edition in English, 52 (2013) 8828-8878.

[151] A.K. Nowinski, F. Sun, A.D. White, A.J. Keefe, S. Jiang, Sequence, structure, and function of peptide self-assembled monolayers, Journal of the American Chemical Society, 134 (2012) 6000-6005.

[152] D.K. Aswal, S. Lenfant, D. Guerin, J.V. Yakhmi, D. Vuillaume, Self assembled monolayers on silicon for molecular electronics, Analytica Chimica Acta, 568 (2006) 84-108.

[153] P. Chinwangso, A.C. Jamison, T.R. Lee, Multidentate adsorbates for self-assembled monolayer films, Accounts of Chemical Research, 44 (2011) 511-519.

[154] R.K. Smith, P.A. Lewis, P.S. Weiss, Patterning self-assembled monolayers, Progress in Surface Science, 75 (2004) 1-68.

[155] Y. Qi, Investigation of organic films by atomic force microscopy: Structural, nanotribological and electrical properties, Surface Science Reports, 66 (2011) 379-393.

[156] F. Klappenberger, Two-dimensional functional molecular nanoarchitectures – Complementary investigations with scanning tunneling microscopy and X-ray spectroscopy, Progress in Surface Science, 89 (2014) 1-55.

[157] P. GuyotSionnest, A.-A. Dhirani, R. Zehner, R. Hsung, P. Guyot Sionnest, L. Sita, Self-Assembly of Conjugated Molecular Rods: A High-Resolution STM Study, Journal of the American Chemical Society, 118 (1996) 3319-3320.

[158] P. Maksymovych, D.C. Sorescu, J.T. Yates, Jr., Gold-adatom-mediated bonding in self-assembled short-chain alkanethiolate species on the Au(111) surface, Physical Review Letters, 97 (2006) 146103.

[159] M. Edelwirth, J. Freund, S.J. Sowerby, W.M. Heckl, Molecular mechanics study of hydrogen bonded self-assembled adenine monolayers on graphite, Surface Science, 417 (1998) 201-209.

[160] M. Tchalala, H. Enriquez, A. Mayne, A. Kara, S. Roth, M. Rachid Tchalala, M. Silly, A. Bendounan, F. Sirotti, T. Greber, B. Aufray, G.r. Dujardin, M. Ait Ali, H. Oughaddou, Formation of one-dimensional self-assembled silicon nanoribbons on Au(110)-(2 × 1), Applied Physics Letters, 102 (2013) 083107.

[161] K.V. Wolf, D.A. Cole, S.L. Bernasek, High-resolution TOF-SIMS study of varying chain length self-assembled monolayer surfaces, Analytical Chemistry, 74 (2002) 5009-5016.

[162] M. Schröder, S. Sohn, H.F. Arlinghaus, Investigation of secondary cluster ion emission from self-assembled monolayers of alkanethiols on gold with ToF-SIMS, Applied Surface Science, 231-232 (2004) 164-168.

[163] H. Min, G. Jung, D.W. Moon, I.S. Choi, T.G. Lee, Quantitative analysis of mixed self-assembled monolayers using ToF-SIMS, Applied Surface Science, 255 (2008) 1037-1039.

[164] L.H. Dubois, B.R. Zegarski, R.G. Nuzzo, Molecular ordering of organosulfur compounds on Au(111) and Au(100): Adsorption from solution and in ultrahigh vacuum, The Journal of Chemical Physics, 98 (1993) 678.

[165] J. Pflaum, G. Bracco, F. Schreiber, R. Colorado, O.E. Shmakova, T.R. Lee, G. Scoles, A. Kahn, Structure and electronic properties of CH_3- and CF_3-terminated alkanethiol monolayers on Au(111): a scanning tunneling microscopy, surface X-ray and helium scattering study, Surface Science, 498 (2002) 89-104.

[166] J. Noh, E. Ito, K. Nakajima, J. Kim, H. Lee, M. Hara, High-Resolution STM and XPS Studies of Thiophene Self-Assembled Monolayers on Au(111), The Journal of Physical Chemistry B, 106 (2002) 7139-7141.

[167] C.-Y. Lee, P. Gong, G. Harbers, D. Grainger, D. Castner, L. Gamble, Surface Coverage and Structure of Mixed DNA/Alkylthiol Monolayers on Gold: Characterization by XPS, NEXAFS, and Fluorescence Intensity Measurements, Analytical Chemistry, 78 (2006) 3316-3325.

[168] M. Dhayal, D. Ratner, XPS and SPR Analysis of Glycoarray Surface Density, Langmuir, 25 (2009) 2181-2187.

[169] C.M. Pradier, M. Salmain, L. Zheng, G. Jaouen, Specific binding of avidin to biotin immobilised on modified gold surfaces - Fourier transform infrared reflection absorption spectroscopy analysis, Surface Science, 502 (2002) 193-202.

[170] M. Bieri, T. Burgi, Adsorption kinetics of l-glutathione on gold and structural changes during self-assembly: an in situ ATR-IR and QCM study, Physical Chemistry Chemical Physics, 8 (2006) 513-520.

[171] R.G. Freeman, K.C. Grabar, K.J. Allison, R.M. Bright, J.A. Davis, A.P. Guthrie, M.B. Hommer, M.A. Jackson, P.C. Smith, D.G. Walter, M.J. Natan, Self-Assembled Metal Colloid Monolayers: An Approach to SERS Substrates, Science, 267 (1995) 1629-1632.

[172] M.S. Boeckl, A.L. Bramblett, K.D. Hauch, T. Sasaki, B.D. Ratner, J.W. Rogers, Self-Assembly of Tetraphenylporphyrin Monolayers on Gold Substrates, Langmuir, 16 (2000) 5644-5653.

[173] L. Houssiau, P. Bertrand, TOF–SIMS study of alkanethiol adsorption and ordering on gold, Applied Surface Science, 175 (2001) 399-406.

[174] A. Auditore, N. Tuccitto, S. Quici, G. Marzanni, F. Puntoriero, S. Campagna, A. Licciardello, ToF-SIMS investigation of functional mixed aromatic thiol monolayers on gold, Applied Surface Science, 231-232 (2004) 314-317.

[175] S. Sohn, M. Schröder, D. Lipinsky, H. Arlinghaus, ToF-SIMS investigations of the degeneration processes of self-assembled monolayers of alkanethiols on gold, Surface and Interface Analysis, 36 (2004) 1222-1226.

[176] D. Weibel, S. Wong, N. Lockyer, P. Blenkinsopp, R. Hill, J.C. Vickerman, A C_{60} primary ion beam system for time of flight secondary ion mass spectrometry: its development and secondary ion yield characteristics, Analytical Chemistry, 75 (2003) 1754-1764.

[177] R.D. Rickman, S.V. Verkhoturov, E.A. Schweikert, Cluster secondary ion mass spectrometry: an insight into "super-efficient" collision cascades, Applied Surface Science, 231-232 (2004) 54-58.

[178] M.J. Eller, S.V. Verkhoturov, S. Della-Negra, E.A. Schweikert, Electron Emission From Hypervelocity C_{60} impacts, Journal of Physical Chemistry C, 114 (2010) 17191-17196.

[179] D.K. Schwartz, Mechanisms and kinetics of self-assembled monolayer formation, Annual Review of Physical Chemistry, 52 (2001) 107-137.

[180] S. Pan, A.M. Belu, B.D. Ratner, Self assembly of 16-mercapto-1-hexadecanol on gold: surface characterization and kinetics, Materials Science and Engineering: C, 7 (1999) 51-58.

[181] F. Schreiber, Structure and growth of self-assembling monolayers, Progress in Surface Science, 65 (2000) 151-257.

[182] P. Fuchs, Low-pressure plasma cleaning of Au and PtIr noble metal surfaces, Applied Surface Science, 256 (2009) 1382-1390.

[183] B. Koslowski, H.G. Boyen, C. Wilderotter, G. Kästle, P. Ziemann, R. Wahrenberg, P. Oelhafen, Oxidation of preferentially (111)-oriented Au films in an oxygen plasma investigated by scanning tunneling microscopy and photoelectron spectroscopy, Surface Science, 475 (2001) 1-10.

[184] A. Ulman, Formation and Structure of Self-Assembled Monolayers, Chemical Reviews, 96 (1996) 1533-1554.

[185] J.C. Love, L.A. Estroff, J.K. Kriebel, R.G. Nuzzo, G.M. Whitesides, Self-assembled monolayers of thiolates on metals as a form of nanotechnology, Chemical Reviews, 105 (2005) 1103-1170.

[186] L. Houssiau, P. Bertrand, TOF–SIMS study of alkanethiol adsorption and ordering on gold, Applied Surface Science, 175-176 (2001) 399-406.